Journal of Energy Chemistry 87 (2023) 256–285

Contents lists available at ScienceDirect

Journal of Energy Chemistry

journal homepage: www.elsevier.com/locate/jechem

http://www.journals.elsevier.com/journal-of-energy-chemistry/

Molybdenum disulfide as hydrogen evolution catalyst: From atomistic to materials structure and electrocatalytic performance

Mohsin Muhyuddin [a], Giorgio Tseberlidis [a], Maurizio Acciarri [a], Oran Lori [d], Massimiliano D'Arienzo [a], Massimiliano Cavallini [b], Plamen Atanassov [c], Lior Elbaz [d], Alessandro Lavacchi [e], Carlo Santoro [a,*]

[a] Department of Materials Science, University of Milano-Bicocca, Via Roberto Cozzi 55, Building U5, 20125 Milan, Italy
[b] Istituto per lo Studio dei Materiali Nanostrutturati, (ISMN), Consiglio Nazionale delle Ricerche (CNR), Via P. Gobetti 101, Bologna, Italy
[c] Department of Chemical and Biomolecular Engineering, University of California, Irvine, CA 92697, United States
[d] Department of Chemistry and the Institute of Nanotechnology and Advanced Materials, Bar-Ilan University, Ramat-Gan 5290002, Israel
[e] Institute of Chemistry of the Organometallic Compounds - National Research Council (ICCOM-CNR), Via Madonna del Piano, 10, 50019 Sesto Fiorentino (FI), Italy

ARTICLE INFO

Article history:
Received 11 July 2023
Revised 7 August 2023
Accepted 12 August 2023
Available online 23 August 2023

Keywords:
Hydrogen evolution reaction
Molybdenum disulphide
Electrocatalysts
Synthesis techniques
Sustainable energy production
Water electrolysis

ABSTRACT

Hydrogen production via water electrolysis defines the novel energy vector for achieving a sustainable society. However, the true progress of the given technology is hindered by the sluggish and complex hydrogen evolution reaction (HER) occurring at the cathodic side of the system where overpriced and scarce Pt-based electrocatalysts are usually employed. Therefore, efficient platinum group metals (PGMs)-free electrocatalysts to carry out HER with accelerated kinetics are urgently demanded. In this scenario, molybdenum disulfide (MoS_2) owing to efficacious structural attributes and optimum hydrogen-binding free energy (ΔG_{H^*}) is emerging as a reliable alternative to PGMs. However, the performance of MoS_2-based electrocatalysts is still far away from the benchmark performance. The HER activity of MoS_2 can be improved by engineering the structural parameters i.e., doping, defects inducement, modulating the electronic structure, stabilizing the 1 T phase, creating nanocomposites, and altering the morphologies using appropriate fabrication pathways. Here, we have comprehensively reviewed the majority of the scientific endeavors published in recent years to uplift the HER activity of MoS_2-based electrocatalysts using different methods. Advancements in the major fabrication strategies including hydrothermal synthesis methods, chemical vapor deposition, exfoliation techniques, plasma treatments, chemical methodologies, etc. to tune the structural parameters and hence their ultimate influence on the electrocatalytic activity in acidic and/or alkaline media have been thoroughly discussed. This study can provide encyclopedic insights about the fabrication routes that have been pursued to improve the HER performance of MoS_2-based electrocatalysts.

Mohsin Muhyuddin is a final year doctoral candidate in the Materials Science and Nanotechnology Department of the University of Milano-Bicocca where he is pursuing his research under the supervision of Dr. Carlo Santoro at the Electrocatalysis and Bioelectrocatalysis laboratory. He completed his Bachelor and Master of Science in Materials Science and Engineering from the Institute of Space Technology (IST), Islamabad, Pakistan in the year 2016 and 2019, respectively. Presently, Mohsin's area of research includes the development of advanced and cost-effective noble metals-free electrocatalysis for sustainable energy applications.

Giorgio Tseberlidis received his PhD in Industrial Chemistry in 2018 under the supervision of Prof. Alessandro Caselli at the University of Milano (Italy), working on the catalytic applications of pyclen metal complexes. He then moved to the Department of Materials Science of the University of Milano-Bicocca (Italy) in 2019, where he is currently Post-doc researcher in the group of Prof. Simona Binetti. His research is focused on the growth of earth-abundant chalcogenides and their use in photovoltaic and photocatalytic applications.

* Corresponding author.
E-mail address: carlo.santoro@unimib.it (C. Santoro).

https://doi.org/10.1016/j.jechem.2023.08.011

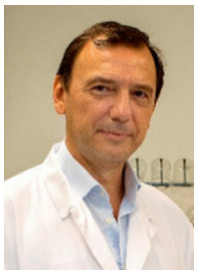

Maurizio Filippo Acciarri, is associate professor of Physics at UNIMIB. His research is mainly addressed to the study of photovoltaic cells and more generally to the physical aspects of energy efficiency and energy storage. In this area, he studied CO_2 capture from industrial fumes and use. He is the coordinator of the GEM (Green Energy Management) Summer School and is president of the international network "SILKWAY - Energy, Connectivity, Environment, People" made up of universities, local and international stakeholders and other external partners from Europe and Central Asia. He participates to the Network for the Sustainable Development of Universities energy working group as a contact for UNIMIB for the energy sector and he is the coordinator of the Energy Committee of the Milano-Bicocca University. Since 2019 he has been a member of the Institutional Research Committee of the National Energy Cluster as a representative of physicists (Physics for energy).

Massimiliano D'Arienzo is Associate Professor of General and Inorganic Chemistry at the University of Milano-Bicocca since 2018 at the Department of Materials Science in the University of Milano-Bicocca. His expertise spans from the synthesis by soft chemistry methods of ceramics and inorganic materials with controlled morphological and surface features, to their exploiting in hybrid materials employed in a wide range of applications (e.g. photocatalysis, catalysis, LIBs, gas sensing and automotive). The results of his research activity provided scientific and technological impacts, leading to several financed national and European projects, 80 peer-reviewed papers, two book chapters and five patents.

Plamen Atanassov is a Chancellor's Professor of Chemical & Biomolecular Engineering, University of California Irvine, where his research focuses on the development of non-platinum electrocatalysts for fuel cells, nano-structured platinum-based catalysts and advanced supports, catalysts for CO_2 electroreduction and products valorization, ammonia electrosynthesis and new materials and technologies for energy conversion and storage. He is participating the effort to build California's hydrogen hub by serving on the executive team for Alliance for Renewable Clean Hydrogen Energy Systems (ARCHES) and interfacing with hydrogen technology demonstration and research efforts regionally and Nation-wide. Plamen Atanassov was inducted into the National Academy of Inventors, and he is a Fellow of both: The Electrochemical Society and the International Society of Electrochemistry, for which he is the current President-elect.

Alessandro Lavacchi is a senior researcher at the Institute of Organometallic Chemistry of the National Research Council of Italy, where he also is the head of the Electron Microscopy Facility and the elected head of the Technology Transfer Center. His research focuses on the development and characterization of nanomaterials for electrochemical conversion and storage, with a focus on alkaline membrane electrolysis and biomass conversion in electrochemical devices. He co-authored more than 130 papers, mostly on energy materials, and the monograph "Nanotechnology in Electrocatalysis for Energy

Oran Lori currently holds a postdoc position in the chemistry department at the University of California, Irvine. His research revolved around the microstructure and stability of sol-gel-based ceramic nuclear fuels and fuel analogues under radiation conditions. Prior to that, he spent a couple of years in the space industry working on oxygen evolution using molten oxide electrolysis chiefly from lunar soil. Oran received his PhD in chemistry from Bar-Ilan University in 2021 focusing on development of ceramic materials and electrocatalysis of hydrogen-based energy technology.

Massimiliano Cavallini is the Research Director at CNR-ISMN, where he leads the multidisciplinary "Nanotechnology of Multifunctional Materials" group. He earned a Laurea cum Laude in 1995 and a PhD in Chemistry in 1999 from the University of Florence. His research encompasses unconventional bottom-up nanofabrication, dewetting, polymorphism, information storage and nano-electrochemistry for nanofabrication. He boasts authorship of more than 150 papers, and multiple book chapters, and holds 15 international patents. Cavallini has also participated as Principal Investigator on various EU projects and was honored with the ESF-European Young Investigator Award in 2006.

Lior Elbaz is a Professor at the Chemistry Department, Bar-Ilan University. He is the head of the Israeli Fuel Cells Consortium (IFCC) and the Director of the Hydrogen Technologies lab at the Israel National Institute for Sustainable Energy (NISE). In his current work, Lior has been focusing on the development of molecular and PGM-free aerogel-based catalysts for hydrogen technologies.

Carlo Santoro got his Ph.D. at the University of Connecticut in 2009, working on microbial fuel cells. He moved to the University of New Mexico in 2013 working on platinum-free electrocatalysts for oxygen reduction reaction and supercapacitive bio-electrochemical systems. Following a spell as Lecturer at the University of Manchester (2020), he joined the University of Milano-Bicocca in 2021 as Assistant Professor, where he established the Electrocatalysis and Bioelectrocatalysis Lab (EBLab). His work focuses on development of electrocatalysts based on platinum-group metal-free materials for electrochemical systems, pursuing biomimetic and bioinspired approaches. He has published over 125 manuscripts (Hindex=45) and holds 2 patents.

1. Introduction

Global warming and atmospheric pollution due to the release of toxic gases are shaping a severe crisis for the present era where the burning of fossil fuels is one of the main causes of these unprecedented challenges [1–4]. On the other hand, energy demands in the last decade have drastically increased and it is expected that total energy consumption will cross 30 Terawatt (TW) by the year 2050 which is almost threefold of what was required in 2010 [5,6]. Hence a prime reliance on annihilating fossil fuels is insufficient to safely power the planet. Such a dilemmatic situation enthralls the attention of the scientific community to urgently provide viable and permanent solutions for the aforementioned problems. Therefore, the concept of the *Hydrogen Economy* presenting hydrogen as a green energy vector was coined in the 1970s [7,8]. Using hydrogen as a fuel not only ensures zero carbon emission but it has a maximum energy content that is about three times that of gasoline [9].

Mass-scale hydrogen production can rely on three typical pathways; (i) methane reforming, (ii) coal gasification and (iii) water

electrolysis [10]. The first two routes, deriving from fossil resources, generate CO_2 as an inevitable by-product and therefore these methods of generating hydrogen contradict the theme of 'Hydrogen Economy' and 'Sustainable Energy' where a core goal is to minimize the planetary carbon footprint. Water electrolysis by employing renewable energy sources provides an opportunity to produce sustainable, environmentally safe, highly pure and compressed hydrogen without any contribution to carbon emission. Moreover, hydrogen storage also gives privilege to conventional renewable energy mechanisms such as wind or solar systems where intermittence and disruptions due to their sole dependency on particular time horizons (i.e., specific periods of a day or season or weather conditions) affect the operational stability of the power grid [11–14]. However, coupling the water electrolysis system with a renewable energy source can clear up this challenge since energy can be stored in the form of hydrogen as a green fuel that afterward can be utilized when and where required [15].

Major classes of low-temperature water electrolyzers involve alkaline water electrolyzers (AWEs), proton-exchange membrane water electrolyzers (PEMWEs) and anion-exchange membrane water electrolyzers (AEMWEs), offering various merits over each other with some technological contrasts [16,17]. PEMWEs are the most efficient system and have the high volumetric hydrogen production rate among the existing water electrolysis technologies [18] whereas AWEs are the most established water electrolysis technology and are commercially available [16]. On the other hand, AEMWEs are the least matured class of water electrolyzers with lower technology readiness levels (TRL). However, they are extremely promising as they combine the advantages of both PEMWEs and AWEs [19].

Typically, the water electrolysis system consists of two half-reactions where hydrogen evolution reaction (HER) takes place at the cathodic side and oxygen evolution reaction (OER) is launched at the anodic side [20]. However, despite the huge interest in hydrogen production via water electrolysis, mass-scale commercialization of PEMWEs has not yet been rationalized. One of the major obstacles in the given pursuit is the utilization of platinum group metals (PGMs) electrocatalysts to catalyze both reactions that are heavily used in PEMWE systems but often used also in other low-temperature water electrolyzers.

Regrettably, the skyrocketing prices and rarity of PGMs used for HER (platinum) and OER (iridium) in the acidic environment are the key bottlenecks that ultimately make hydrogen production through PEMWEs economically impractical. In parallel, the sluggishness and complexity of HER taking place with larger overpotential are also important issues to be overcome [21,22]. To address such problems, the electrocatalytic activity needs to be improved by developing a suitable electrocatalyst that can proficiently boost the kinetics of HER by lowering the activation energy and hence overpotentials [23]. Merits of any potential electrocatalyst include enhanced electrocatalytic activity, operational durability, non-toxicity, ease to synthesize, abundance and cost-effectiveness. However, scarce and overpriced PGMs, belonging to the class of critical raw materials (CRMs), are utilized to perform HER owing to their ability to reduce the overpotential and expedite the reaction kinetics at appreciable rates [23–27]. Up to now, the most efficient and state-of-the-art electrocatalyst for HER in acid media is composed of platinum nanoparticles supported over a conductive carbon backbone (Pt/C) [28]. To solve this limitation plethora of scientific endeavors has been invested in the development of reliable PGM-free electrocatalysts for the execution of HER [24,25,29–32]. Such attempts include a variety of PGM-free electrocatalysts fabricated with earth-abundant constituents such as transition metals-based borides [33–35], nitrides [36,37], chalcogenides [38–44], carbides [45–47], phosphides [48–50], alloys [51,52], metal-free electrocatalysts [53] and even electrocatalysts derived from organic waste [6,54–56]. However, the available options for electrocatalysts are still lacking excellence. For instance, PGMs with lower loadings mainly platinum, palladium, iridium and ruthenium-based materials are not only expensive but also deprived of the stability demands for their industrialization [57] as they tend to agglomerate and leach out from the support materials in extremely acidic and alkaline conditions [57,58]. Similarly, nickel which is considered one of the most potential transition metals to replace PGMs for HER owing to its suitable electronic structure supporting the Ni-H bonds [59], also gets dissolved in acidic environments and finally leads to the deactivation of the electrocatalyst [57]. Moreover, the HER performance of nitrides and metallic electrocatalysts comparable to the PGM-based has not been achieved yet [60]. Despite being the efficient class of electrocatalysts, transition metal phosphides cry out for safer and faster synthesizing methods because longer reaction times at elevated temperatures and the generation of toxic gases and organic compounds are the biggest hindrances in their mass-scale productions [48]. Oxide and hydroxide no doubt demonstrate higher stability but their inherited lower conductivity and unsatisfactory electrocatalytic activity limit their employment for HER [61]. On the other hand, although transition metal carbides have good electronic conductivity their intrinsic activity remains restricted due to the very strong attachment of the reaction intermediates and difficult desorption of H_{asd}, prohibiting the HER kinetics severely [62,63]. Therefore, still there is significant room for advanced research in the arena of PGM-free HER for a mature evolution of efficient and robust electrocatalysts ensuring the commercial practicality of water electrolysis.

Among various PGM-free candidates for HER, nanostructured molybdenum disulfide (MoS_2) is an emerging choice due to its highly active edge sites with the free energy of hydrogen adsorption not far from that demonstrated by PGMs [10,64–66]. Pioneering work to evaluate the electrochemical feature of the bulk MoS_2 was conducted by Tributsch and Bennett who initially found it inactive towards HER [67]. In fact, bulk MoS_2 possesses a lower surface area where individual layers are loosely bonded together through Van der Waal interactions, leading to reduced exposure of active sites and limited conductivity [65]. Later on, Hinnemann and coworkers confirmed the excellent HER electrocatalytic activity of nanostructured MoS_2 since it shows biomimetic ability similar to that of enzymatic nitrogenase [68]. Edges of MoS_2 are electrochemically more active compared to basal planes and particularly Mo-edge has a hydrogen adsorption energy of nearly 0.08 eV with 50% hydrogen coverage which is similar to Pt [65,68]. This astonishing aspect of nanostructured MoS_2 can revolutionize the paradigm of PGM-free HER electrocatalysis if underlying issues associated with MoS_2 (i.e., poor conductivity, the inertness of basal plane and fewer exposed active moieties) are overcome. Therefore, crucial research hotspots for MoS_2-assisted HER could be the engineering of active sites/edges, inducing electrocatalytic activity within the inert basal plane, structural modification via defect engineering and strategies to enhance the conductivity and controlling the phase transformation [64,69,70]. It is a well-established fact that the active site engineering and enhancement of HER activity of MoS_2 can be carried out by designing the appropriate fabrication route where efficient activity, operational durability, manufacturing cost and scalability should also be among the essential consideration. Therefore, over the last few decades, the structural parameters to improve the electrocatalytic performance have been engineered through several pathways such as hydrothermal route, chemical vapor deposition (CVD), exfoliation, colloidal synthesis, plasma-assisted approaches and so on. The choice and route followed in each fabrication strategy can remarkably improve performance.

This review covers the most recent scientific attempts at developing efficient and robust MoS_2-based nanostructured HER electrocatalysts using a wide spectrum of fabrication pathways. Firstly, the two-dimensional (2D) structural integrity of MoS_2 is presented followed by a brief discussion on HER mechanism and MoS_2 stability over the pH range. The detailed discussion of the most important considerations while engineering the active site structure also provides essential grounds for a fundamental understanding. Then scientific developments for effective MoS_2-based electrocatalysts are thoroughly reviewed and comprehensively presented with a prime focus on the fabrication strategies to engineer the structural parameters and hence optimize the HER performance. Finally, the challenges and prospects of MoS_2-based electrocatalysts for hydrogen production have been discussed in detail.

2. Molybdenum disulfide

Transition metal dichalcogenides (TMDCs) are MX_2-type semiconductors, where M stands for transition metal (such as Mo, W, etc.) and X corresponds to a chalcogen (such as S, Se, or Te). They often have a layered structure and can be considered Van der Waals solids [71] since they maintain a strong covalent bonding within the layers while having weak Van der Waals interactions between the layers. Each layer of TMDCs further consists of three sub-atomic layers in which the transition metal atom is sandwiched between two chalcogen atoms [72]. MoS_2 exists both as a pristine bulk material as well as in two-dimensional (2D) form where it represents the most chemically stable and robust 2D material compared to the other TMDCs. The peculiar layered structure of MoS_2 provides relevant functional properties. The leading property of MoS_2 is its capability to act as a solid and dry lubricant [73]. Later MoS_2 attracted much interest for its applications in heterogeneous catalysis [74]. More recently the use of MoS_2 has been proposed in a variety of energy-related processes. Among them, we mention the application in supercapacitors [75] or as an electrocatalyst for the CO_2 reduction reaction [76]. In this regard, MoS_2 can be considered a kind of "super-material", with highly tunable properties that can enable its application in many fields. Later on, MoS_2 emerged as an effective HER electrocatalyst particularly in acidic environments, providing the opportunity to build electrodes for PEMWEs without relying on PGMs and CRMs. Therefore, MoS_2 might provide an amazing opportunity to make PEMWEs, the most efficient system to produce hydrogen at high intensity, more resilient enabling the possibility to deploy it at the TW scale by 2050.

2.1. Structural parameters

In nature, MoS_2 occurs as molybdenite, a bright natural mineral composed of stacked slices with polygonal boundaries. The constrained arrangement of angles between the sides, limited to multiples of 60°, can be attributed to the underlying principles of energy minimization in boundary energy density. This phenomenon is analogous to the behavior observed in three-dimensional materials, where specific shapes are determined by the minimization of energies along distinct crystallographic planes [77]. The bulk MoS_2 is layered solid and composed of several monolayers. Each layer typically has a thickness of 6–7 Å with strong in-plane covalent bonding and weak out-of-plane Van der Waals interactions [78].

MoS_2 can exist in three different phases i.e., hexagonal trigonal prismatic (2H), rhombohedral (3R), and octahedral (1 T) coordination of metal atoms [79] as illustrated in Fig. 1(a). In all these three structures, each layer of molybdenum is sandwiched between two layers of sulfur. The extra 1 T phase is a strained version in which metallic atoms interact with each other. The 2H phase is the most thermodynamically stable configuration for MoS_2 while the others are metastable [80]. Bulk MoS_2 is a random mix of stacked layers with different phases, giving the material an overall band gap of 0.88 eV. Monolayer phases i.e., 2H and 3R are typically semiconductors with a theoretical band gap of ca. 1.71 eV. However, the experimental value can be raised to 2.16 eV depending upon the structural attributes [79,81]. This difference indicates dissimilar mechanisms of electron transformation between valence and conduction bands for 2D and 3D materials [80]. Fig. 1(b) illustrates the distribution of energy (energy with respect to wave-vector k) in different variants of MoS_2 such as bulk, quadrilateral (4L), bilayer (2L), and monolayer (1L). The energy level of the highest band located at the K point is indicated by the horizontal line whereas, the edges of valence and conduction bands are represented by blue and red lines, respectively. The transition with the lowermost energy (specified by the solid arrows) could be direct (vertical) only in the event of a single layer. On the other hand, the energy transitions in the monolayer (indicated by the dashed arrow in the 1L plot) are higher compared to the direct band transitions (indicated by the solid arrow).

During this transition from bulk to single-layer MoS_2, the electronic structure behaves as follows: the orbitals contributing to the conduction band states at the K point state are localized within the S-Mo-S sandwich, but the states at the Γ point and the conduction band minimum (CBM) point have strong characters of the *d* orbitals of molybdenum and the antibonding *Pz* orbitals of sulfur, leading to the strong dependence on vertical interlayer coupling. Furthermore, in the case of the indirect gap transition, the K point state remains constant, but the energy of the other states is reduced. More in detail, as the number of layers, is reduced to a single layer, the Γ point state in the valence band has less energy than the K point, and thus the K point state becomes the valence band maximum (VBM) [82]. The downsizing of MoS_2 to 2D nanostructured MoS_2 induces excellent potential for HER activity as not only electronic redistribution takes place but also the delamination into single-layered configuration brings Mo and/or sulfur atoms at the terminal edges along with a lot of dangling bonds. Atoms located at the kinks, defects, edges and corners have lower coordination and they settle over the basal planes and produce the active sites for HER with easy electronic interaction. The sulfur passivation of the molybdenum edge causes higher activity because of unsaturated coordination and a sulfur-dense environment. Moreover, the unsatisfied dangling bonds and lower coordination in the 2D MoS_2 make the connection of substrate and molybdenum atom at the edges possible which in turn increases the active sites and conductivity [64].

HER performance is highly controlled by the nature of phases present in the MoS_2 because the electrocatalytic activity originates from the metallic coordination [83]. The 1 T phase exhibits metallic properties such as high electrical conductivity and electrocatalytically active basal plane whereas the other two phases i.e., 2H and 3R are semiconductor in nature with wide bandgap structure. 1 T MoS_2 can be produced by disrupting a single sulfur layer in the 2H phase. Both the basal plane and sulfur-containing edges in the 1 T phase constitute the active sites for HER whereas in crystalline 2H MoS_2 HER can only be carried out by uncoordinated sulfur atoms located at the edges [64,84]. It is important to underline that charge carrier mobility along the edges is 2200 times higher but the inferior conductivity between the stacked layers not only inhabits the charge mobility between the active centers and electrode but the electrochemically inert basal plane of bulk and 2H MoS_2 restricts the HER activity. Moreover, electronic conductivity is particularly controlled by the number of non-bonding *d* electrons distributed between the antibonding and bonding states of

molybdenum-sulfur bonds and the corresponding coordination of molybdenum. Therefore, the phase stability and transition from semiconducting 2H to 1 T solely depend on the *d* orbital filling scenario. In 2H MoS_2, all the non-bonding *d* orbitals are fully filled, making it a semiconductor. On the other hand, the metallic nature of the 1 T phase is due to the partially filled non-bonding *d* orbitals that favor electron transportation and uplift the kinetics electrocatalytic activity [84,85]. The electronic conductivity of the metallic 1 T phase is 10 folds higher than the 2H phase of MoS_2 which implies significant resistance and therefore insufficient charge transportation [69,86]. Another, amazing property of 1 T MoS_2 is its remarkable hydrophilicity which is again attributed to the structural suitability where the staggered sulfur atoms on either side of the triangular sheets can bring the molybdenum atoms nearer to the surface which ensures the hydrophilicity [69,87]. When 1 T MoS_2 is dispersed in water it does not aggregate and shows a contact angle of 25° whereas the 2H MoS_2 instantly tends to aggregate while showing a 118° contact angle in solid form [88]. Therefore, compared to the few-layered 2H phase of MoS_2, the 1 T phase clearly show extraordinarily higher HER activity [69,89]. However, the instability of the 1 T phase and its natural tendency to convert to 2H-MoS_2 over time is the major challenge in its deployment for electrocatalysis. In the light of crystal field theory, 1 T-MoS_2 instability and vulnerability to transform into 2H-MoS_2 is derived from the asymmetric holding of electrons in Mo 4*d* orbitals. In the typical 1 T phase of MoS_2, due to the octahedral coordination of Mo atoms in the ligand fields, the 4*d* orbitals get split into t_{2g} and e_g manifolds [90] where the assignment of the two t_{2g} electrons cause severe structural instability. Therefore, the stability of the 1 T phase can be improved by lowering the asymmetric occupation of electrons.

Lin et al. systematically studied the transition between the phases of MoS_2 and elucidated that the phase transformation does not involve any addition of new atoms and only atomic displacement takes place collectively [91]. Using in situ microscopic analysis, it was observed that 2H/1T transformation occurs due to the gliding of atomic planes of molybdenum and/or sulfur from an intermediate phase known as α-phase (phase stable at higher temperature and does not involve the trigonal arrangement of molybdenum atoms, but they are aligned in zigzag form), acting as a precursor in which the migration of boundaries support the growth of second phase. Moreover, Lin et al. also grew 1 T Phase on the 2H layer through an electron beam. In a similar context, Zhu et al. revealed that 2H → 1 T phase transformation can be locally induced in single-layered MoS_2 through weak bombardment with Argon plasma however, the formed 1 T domains can be of few nanometers in size. The 1 T phase is stabilized due to point defects particularly, sulfur vacancies [92]. Another exciting attempt was made by He and co-workers to stabilize the 1 T MoS_2 nanoflowers. The strategy was based on a simplistic electron injection by chemically bonding TiO_2 to 1 T MoS_2 to develop a composite on a larger scale. The election-injection engineering evoked the reconstitution of 4*d* orbitals of molybdenum that ensured 100% conversion of 2H MoS_2 into 1 T MoS_2 [93].

2.2. Application as an HER electrocatalyst

Over the past few years, MoS_2-based electrocatalysts with diverse nanostructures and morphologies, such as nanoparticles, nanosheets (NSs), and nanorods (NRs), etc. have been recognized as promising alternatives of PGMs for the HER electrocatalysis due to their higher abundance, cost-effectiveness and robust electrocatalytic activity [96–101]. Heteroatoms of sulfur can induce the *d*-band electron redistribution of adjacent metal atoms, which can accelerate the adsorption and desorption of intermediate hydrogen (H). Interesting structural attributes such as preferred

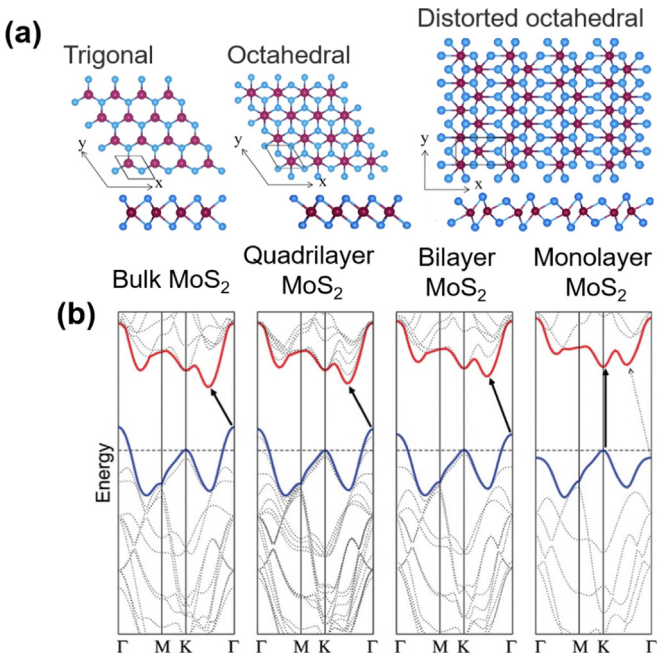

Fig. 1. Three crystalline phases of MoS_2 (a). From left to right: trigonal, octahedral and its strained version [94]. Energy versus wavevector (K) in bulk, four-layers, two-layers, single layer(1L) MoS_2 from left to right (b) [95]. (a) Reproduced with permission from Ref. [94]. Copyright 2015, Institute of Physics (IOP). (b) Reproduced with permission from Ref. [95]. Copyright 2010, American Chemical Society (ACS).

electronic distribution, low bandgap energy and adjustable phase interfaces, make the TMDCs and particularly MoS_2 effective candidates for the reaction of hydrogen evolution.

Owing to hydrogen-binding free energies (ΔG_{H^*}) similar to that of Pt and a preferred 2D structure, MoS_2 has been a research hotspot for the electrocatalytic HER. The 2D layered structure can benefit charge transport from the electrode surface to active sites and the enhanced edge sites provide a low adsorption ΔG_{H^*} for the HER. However, the poor conductivity of MoS_2 is a major bottleneck and causes high over-potential for HER [102]. In parallel, it was shown that bulk MoS_2 is a poor HER electrocatalyst [103]. Importantly, both experimental and computational studies confirm that the HER activity of MoS_2 correlates with the number of catalytically active edge sites that are abundantly present in the 2D monolayer configuration [104–107].

3. Fundamentals of HER

Water can be split by passing an electric current through it, producing hydrogen and oxygen at the cathodic and anodic sides of the system, respectively. This process constitutes the basis for water electrolysis the overall reaction of which is carried out as shown below:

$$2H_2O \rightarrow 2H_2 + O_2$$

Similar to various other electrochemical redox reactions, HER is also a surface phenomenon taking place at the electrode/electrolyte interface [8]. HER follows a complex pathway that typically involves three elementary steps whose mechanism is modified as the pH of the electrolytic media is altered. For acidic media, the first stage is the Volmer step leading to the adsorption of the proton (H^+) on the active moieties (M) of the participating electrocatalyst (Eq. (1)). Subsequently, the reaction must either continue electrochemically or chemically in a competitive way to carry out desorption of the product. Electrochemical desorption begins

when the already adsorbed proton (H_{ads}) combines with another H^+ and electron (e^-) to generate molecular H_2 and this event is known as the Heyrovsky step (Eq. (2)). On the other hand, molecular H_2 can also be evolved via Tafel step (chemical desorption) in which two of the H_{ads} combine and leave the electrocatalyst surface (Eq. (3)) [108].

Volmer step in acidic media:

$$M + H^+ + e^- \rightarrow M^*H_{ads} \quad (1)$$

Heyrovsky step in acidic media:

$$M^*H_{ads} + H^+ + e^- \rightarrow M + H_2 \quad (2)$$

Tafel step in acidic media:

$$H_{ads} + H_{ads} \rightarrow H_2 \quad (3)$$

Notwithstanding HER proceeds similarly under alkaline conditions, the interacting species, in this case, are water molecules instead of protons engendering an additional obligation to first produce protons via water dissociation. The additional water dissociation (Eq. (4)) introduces an extra energy barrier and causes an increase in the overpotential [109,110].

$$H_2O + e^- \rightarrow H_{ads} + OH^- \quad (4)$$

Therefore, the protons deficiency in the alkaline electrolyte makes the HER relatively difficult to pursue and causes the exchange current density to be 2–3 times lower compared to that obtained under acidic conditions. The availability of protons in the acidic environment establishes favorable circumstances for HER. On the other hand, the inherent inadequacy of protons or hydronium ions (H_3O^+) in alkaline conditions not only makes the HER kinetics sluggish but also the plentiful of OH^- ions may cause poisoning of the active moieties and impede the overall reaction kinetics. Hence, electrocatalyst design becomes an important task to realistically improve the HER performance. The modified Volmer step in the alkaline case is again the initial reaction as given in Eq. (5) and HER is likewise followed via Heyrovsky (Eq. (6)) or Tafel step (Eq. (7)).

Volmer step in alkaline media:

$$M + H_2O + e^- \rightarrow M^*H_{ads} + OH^- \quad (5)$$

Heyrovsky step in alkaline media:

$$M^*H_{ads} + H_2O + e^- \rightarrow M + H_2 + OH^- \quad (6)$$

Tafel step in alkaline media:

$$H_{ads} + H_{ads} \rightarrow H_2 \quad (7)$$

HER executes either through Volmer–Heyrovsky or Volmer–Tafel route where the rate-determining step (RDS) can be any of the individual three steps [111,112]. The primary water dissociation step in addition to the Volmer reaction and the interaction of OH^- species on the surface of MoS_2 are the two main challenges in alkaline media. No doubt, MoS_2 could be an efficient electrocatalyst for the adsorption and then recombination of adsorbed protonic intermediates but its insufficient tendency to dissociate water in the alkaline media and improper adsorption of OH^- species are the main causes of MoS_2 sluggish HER activity in alkaline media [110,113]. Therefore, improving the retarded and lower activity of MoS_2 in alkaline media is an essential target that could be achieved by engineering active sites to make them more efficient, robust and performing electrocatalysts [113,114].

In routine practice, the Tafel equation (Eq. (8)) is used to evaluate the underlying HER mechanism and to determine the corresponding RDS [111].

$$\eta = b\log(j) + a \quad (8)$$

The abovementioned Tafel equation is a simplistic relationship among overpotential (η), current density (j), Tafel slope (b) and constant (a), where Tafel slope probes governing HER mechanism and involved RDS. The Tafel slope can be estimated by plotting the logarithmic current density with respect to overpotentials and the slope of the linear part will be the Tafel slope giving a particular value for each RDS. This value indicates the enduring mechanism of the electrocatalytic reaction regarding the kinetics of electron transfer [22]. For instance, current density increasing considerably with respect to the change in overpotential gives a smaller value of the Tafel slope, indicating accelerated kinetics of the given electrocatalytic reaction. When the Volmer step determines the rate, the Tafel slope will be nearly 120 mV dec^{-1} whereas the slope value would be nearly 40 or 30 mV dec^{-1} if the RDS is Heyrovsky or Tafel step, respectively [115]. There would be more Tafel reaction with a higher H_{ad} concentration on the electrocatalyst surface while, in the situation where the concentration of H_{ad} on the electrocatalyst surface is much lower, the Heyrovsky reaction is more probable to occur. For HER electrocatalysis, firstly, the Tafel reaction and then the Heyrovsky reaction as the rate controller is preferred. From the Tafel equation, another important parameter obtained is the exchange current density (J_0) when overpotential (η) is assumed as zero [10]. The J_0 defines the catalytic efficiency and is dependent on the electrode material, the nature of the electrode surface, electrolytic composition and operating temperature. Favorable HER kinetics, fast electronic transformations and higher surface area give rise to a large value of J_0.

As discussed previously, it is clear that hydrogen adsorption (H_{ads}) is successively followed by desorption from the same site of the electrode surface but both phenomena competitively take place where the binding energy of the H_{ads} is the governing factor. Such binding energy should not result in too strong bonding limiting the Heyrovsky and Tafel reactions or too weak limiting the Volmer reaction [116]. In fact, an ideal HER electrocatalyst should demonstrate optimum adsorption and desorption of hydrogen with intermediate bonding energies and satisfy Sabatier's principle of heterogeneous electrocatalysis [39,117,118]. A volcano plot (Fig. 2) is a convenient way to compare HER aptitude for different electrocatalysts as a function of their HER activity and ΔG_{H^*} [119–121] in which peak J_0 can be achieved as ΔG_{H^*} approaches thermoneutrality ($\Delta G_{H^*} \sim 0$) [39,122]. In the volcano map, PGMs find their position nearly at the apex of the volcano representing a benchmark of HER, however, their scarcity and higher prices limit their application [123]. Attractive materials for replacing PGMs as electrocatalysts are therefore TMDCs [124]. Among them, metal sulfides, especially MoS_2, present closer values to the optimal ΔG_{H^*} (nearly 0.08 eV). However, the exchange current density is much lower ($j_0 \sim 10^{-5}$ A cm^{-2}) than the noble metal. In fact, noble metals have an exchange current density in the range of $10^{-4} < j_0 < 10^{-2}$ A cm^{-2} [125–127]. MoS_2 was shown to be one of the most promising electrocatalysts for HER in acidic media owing to its good stability in strong acids. The bulk form of MoS_2 is a weak HER electrocatalyst compared to nanoparticle MoS_2. This result comes from the fact that active edge sites of nanoparticles are much more than their bulk form. Unsaturated sulfide atoms, located on the edge of the structure, work as an active site for HER to adsorb hydrogen with small free energy [128].

Moreover, one of the most important performance descriptors is the overpotential determining the energy required to carry out the electrocatalytic HER [129]. Quite easy to understand that if the overpotential is much higher, HER will be extremely difficult to proceed, and the subsequent reactions will no longer be probable to occur. Overpotential can be estimated by obtaining linear sweep voltammograms (LSVs) at slower scan rates and its value is often taken at the current density of 10 mA cm^{-2} which corresponds to solar water-splitting efficiency of 12.3% [10,23,64]. In

addition to overpotential, Tafel slope and exchange current density the other parameters to analyze and compare the HER performance of the electrocatalysts usually reported in the literature are onset potential, turnover frequency (TOF), specific and mass activities, Faradaic efficiency and operational durability [10,83,130,131]. The onset potential is pretty unclear and a so-called indicator to asses HER activity and is often measured at the current density of 0.5–2 mA cm^{-2} [10]. To avoid the inconsistency among reported values of onset potential the referenced current density must be mentioned. Specific activity can be calculated by normalizing the current at a particular overpotential with respect to the surface area which could be an electrochemical surface area (ESCA), or geometric surface area of the electrode, or the surface area calculated via Brunauer–Emmett–Teller (BET) [130]. Activity can also be reported by normalizing the current with respect to the electrocatalyst loading on the electrode. However, it is then referred to as mass activity. There could be some limitations to using these metrics [130,132] for instance: the calculation of ECSA is technique specific and its value may differ considerably when calculated through different techniques such as cyclic voltammetry (CV) and impedance spectroscopy, leading to possible miscalculations. On the other hand, BET surface area cannot be referred to as the active surface taking part in electrocatalysis. Moreover, the mass activity demonstrates the least accuracy because electrocatalysts with dissimilar morphological characteristics and particle sizes cannot be compared, hence a fair comparison becomes impossible [130].

TOF can be another performance descriptor for HER defined as the average moles of hydrogen produced at a particular active site per unit of time. TOF can be estimated using the following equation (Eq. (9)) [47]:

$$TOF = \frac{I \times N_A}{F \times n \times \Gamma} \tag{9}$$

Here '*I*' represents the current density, N_A corresponds to the Avogadro constant, '*F*' is Faraday's constant and 'Γ' is the number of active sites whereas '*n*' is the number of electrons transferred during HER. However, it is very difficult to measure the TOF accurately as this value may often involve some significant errors [10,130]. The major limitation is the precise calculation of the active sites present on the electrocatalyst surface which may lead to significant errors if the electrocatalyst is composed of more than one element because of the presence of various heterogeneous sorts of active sites. On the one hand, TOF estimation is solely based on the active species located on the surface or at the accessible locations of the electrocatalyst while on the other hand sometimes TOF is calculated by considering all the active sites present in the material irrespective of their unequal accessibility and unclear activity. In spite of being potentially imprecise, TOF can be still used to compare the performance of electrocatalysts of a similar nature. Faradaic efficiency (also coulombic efficiency) is another descriptor for the assessment of charge transfer during an electrochemical reaction [23,47]. Faradaic efficiency is more meaning full for the evaluation of complete water splitting. However, for HER it can be calculated by taking the ratio between the experimentally calculated hydrogen evolution (via gas chromatography, etc.) and the estimated theoretically (charge transfer calculations using potentiostatic integrations). Its value exhibits the efficiency of the electrocatalytic system and specifies the selectivity of the electrocatalyst. Efficiency loss may occur due to the unwanted production of side reactants and heat generation.

Lastly, working durability over a period of time is one of the essential criteria for the assessment of HER electrocatalysts, usually performed either through continuous CV measurements or chronopotentiometric and chronoamperometric analysis [23,47,130]. For stability measurements via CV cycling the initial LSV and final LSV are compared (usually more than 500 cycles are applied) where an increase in overpotential specifies the performance durability. If the difference is less than 10%, it can be regarded as acceptable endurance. Whereas for chronopotentiometric (*i-t* plots) or chronoamperometric (*v-t* plots), analysis variations in current or potential are monitored at the fixed potential or fixed current, respectively (usually related to 10 mA cm^{-2}). Generally, the tests are carried out for 10 h. Among various aforediscussed HER performance descriptors, overpotential, Tafel slope and working durability are the most important, and therefore, are mostly reported [132].

4. Engineering of MoS_2 active sites

MoS_2 is a graphene-like 2D material whose basal surface is electrocatalytically ineffective. To enhance the intrinsic activity of MoS_2-based electrocatalyst many aspects during the site engineering have to be considered such as (i) improving the electronic conductivity, (ii) ionic intercalation and doping of heteroatoms, (iii) defect engineering and introducing atomic vacancies, (iv) morphological modifications, (v) stabilizing the 1 T phase of MoS_2, and (vi) compositing with highly conductive and active substrates [69,83]. However, the electrocatalytic activity mostly comes from active sites located along the edges of MoS_2 layers or more specifically from the defects present in the material. Both substitutional atoms (dopants) [133–136] and atomic vacancies [137–139] generate localized electronic states in the MoS_2 lattice that act as sites for electrocatalysis by decreasing the adsorption energy of the reagent and making the electrocatalytic activity easy.

The most diffused vacancies are single-atom vacancies formed due to the removal of a single atom of Mo or S from the MoS_2 lattice; however, more complex multi-atomic vacancies, are often present in many materials [140]. While single-atom vacancies are usually controllable in statistical distribution multi-atomic vacancies are challenging to control, and often their detrimental effects are higher than the beneficial ones. The electrocatalytic properties of defects were confirmed by both experimental and computational research [128,141]. The importance of the unsaturated sulfur atoms on the edges comes from the fact that they activate the hydrogen evolution. By knowing this fact, materials with structure-sensitive properties at the nanoscale can be constructed to improve the HER activity. Thus, decreasing the size of the particles and lowering the dimensionality due to the quantum confinement effect, can enhance the electrocatalytic activity by increasing

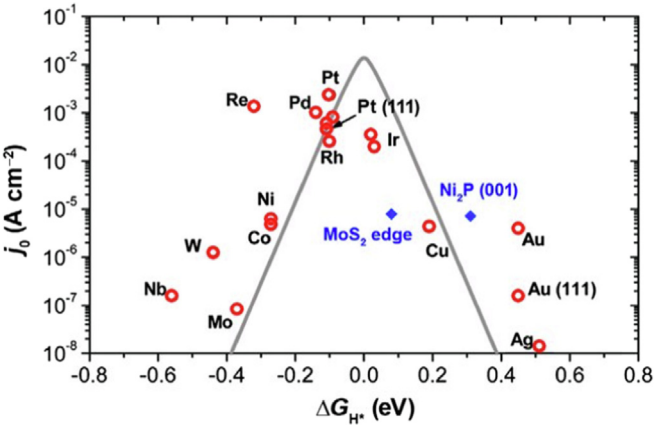

Fig. 2. The activity of the electrocatalysts towards HER has a volcano plot relationship with the free energy change of adsorbed atomic hydrogen [121]. Reproduced with permission from Ref. [121]. Copyright 2014, Royal Society of Chemistry (RSC).

the edge site density [142,143]. Therefore, HER predominantly relies on the structural defects that provide electrocatalytically active sites by tuning the morphological infrastructures and hence electronic interactions. Surface defects, such as zero-dimensional point defects, one-dimensional line defects, and two-dimensional plane defects, are more significant for electrocatalysis because they are located at the surface/interface of the electrocatalysts. [144–146].

Moreover, such defects and atomic vacancies also act as preferred anchoring sites for the dopant atoms and benefit the HER kinetics due to preferable structural modulation. A suitable example comes from a very recent work of Jiang and co-workers in which they developed an amazing fabrication scheme to confine the nickel and iron atoms within the Van der Waals gap of MoS_2 while utilizing isolated sulfur vacancies as favorable anchoring sites for the dual atoms [147]. In this way, a robust electrocatalyst was evolved in which due to interlayer-confinement the dual atomic substitutions remained protected to survive under the extremely acidic environment and demonstrated higher TOF for overall water splitting with nearly 100% faradaic efficiency at the current density of 100 mA cm^{-2}. Furthermore, just the presence of the active sites does not solve the problem of inferior performance instead the present active site should also be exposed and available to participate in the electrochemical reaction. In such regard, Liang et al. reported the coupling of MoS_2(O) with mesoporous carbonic arrays (OMCA) which ensured a significant increase in the exposure of active sites and facilitated the electronic transitions between MoS_2 edges and the substrate material [148]. In this way, they modulated the *d* orbital of molybdenum by modifying the electrons withdrawing/donating ability and hence energetically favor the binding of hydrogen on MoS_2(O). Such an engineered architecture demonstrated intrinsically high per-site activity with TOF of 0.067 s^{-1} at the overpotential of −10 mA cm^{-2} along with operational stability of above 20 h.

No doubt the launching of atomic vacancies boosts intrinsic activity but in some cases, the vacant sites can affect the structural robustness of TMDCs [149,150] and hence the vacancy engineering approach can be less effective [151]. Luckily, the doping of secondary elements can give rise to covalent bonding between the substituting element and the host atoms of TMDCs that not only considerably increase the intrinsic activity of TMDCs due to the synergic effect of doped species but also provide structural stability. However, doping of MoS_2 with transition metals gives more pronounced effects compared to doping of chalcogenides and other heteroatoms which usually modulate the optical bandgap [69]. The metallic substitutions are relatively robust and an abundance of *d* orbitals promotes favorable modifications in phase transformations, conductivity and magnetic characteristics of TMDCs which in turn improve the intrinsic electrocatalytic performance by optimizing the ΔG_{H^*}. Actually, the intrinsic activity of MoS_2 particularly of the 1 T phase can be improved by installing vertical orbitals at the Fermi levels of substrate that enhance the rate of adsorption and desorption of hydrogen intermediates which are otherwise not available in the basal planes. These new orbitals enhance electron transportation to the given active sites and improve the adsorption of hydrogen whereas the drop in transition state energy also promotes the desorption of the intermediates. The molybdenum atoms have *d* orbitals normal to the basal plane but located at the central sub-layers which inhibit hydrogen adsorption. On the other side, sulfur atoms have p_x/p_y orbital at the Fermi level which also makes an adverse scenario for the desorption of the hydrogen because of the unfavorable orientation of the orbitals [69]. However, the empty *d* orbitals of transition metal dopant can stimulate the HER activity by acting as electrophilic groups or providing electron lone pairs that can help in optimizing the 3*d* electronic configuration via chemical bonding. The definitive importance of the 1 T phase of MoS_2 for electrocatalysis, owing to its metallic nature, enhanced conductivity and activity, is well-known however, its metastable nature is the key bottleneck that imparts serious structural instability [69]. However, the instability of the 1 T phase can be reduced by engineering the MoS_2 structure via doping, lithiation, covalent functionalization, ammonia intercalation and so on [69,152–156]. If the parameters of the adopted route are accurately developed, enhanced HER activity can be ensured. For instance, recently Zhang proposed an effective strategy to stabilize the 1 T phase in the MoS_2 nanosheets by anchoring them on a black TiO_{2-x} substrate during in-situ growth on a titanium plate [90]. They anticipated that TiO_{2-x} acts as an electron donor and increases the charge density in the T phase which in turn reduces the asymmetrical possession of electrons in the molybdenum 4*d* orbitals and efficaciously stabilizes the metastable 1 T-MoS_2. Moreover, this structural engineering secured the large surface area with highly exposed active sites and hampered the 1 T-MoS_2 agglomeration during the activity. Owing stabilization of 1 T-MoS_2 on black TiO_{2-x}, the derived electrocatalyst demonstrated excellent HER activity with a very low Tafel slope of 42 mV dec^{-1} (overpotential of 146 mV) and confirmed outstanding electrocatalytic durability over 24 h.

5. Stability of Mo and MoS_2 in acid and alkaline

The stability under a wide potential window is a matter of utmost importance for building practical water electrolyzers. Indeed, HER can operate in a wide range of potentials that depend on the required current output which might be driven by the renewable energy supply. Remarkably, a water electrolyzer can work with peak current densities up to 5 A cm^{-2} to buffer production peaks by intermittent energy source, while constant operation may be in the 1–2 A cm^{-2} range. Recently, it has been demonstrated that in a pressurized PEMWE at a current density of 1.2 A cm^{-2}, the pure activation contribution of the cathode may exceed 150 mV with Pt and might easily exceed 200 mV with PGM-free electrocatalysts [157]. These values might be significantly higher while operating at higher current densities. Accordingly, the range of potential at which the cathode must operate is large. Additionally, at shutdown, the system can go to the open circuit potential, meaning that in practice the cathode electrocatalyst must be stable in a potential window of at least a few hundred mV.

The stability of MoS_2 for HER has been analyzed deeply in recent work by Wang et al. [158]. While MoS_2 has been reported to be stable under HER conditions, experimental data show that degradation by dissolution happens at the open circuit potential. MoS_2 degradation has been indeed observed in refs. [101,159]. The calculated Pourbaix diagram Fig. 3 for MoS_2 indicates that MoS_2 has excellent stability in the −0.4–0 V vs. RHE (reversible hydrogen electrode) potential window. At a more negative potential, the decomposition to H_2S in solution and solid molybdenum can happen; however, these transformations are kinetically sluggish, at least in acidic conditions. Such slow kinetics can practically hamper the decomposition of the materials at such negative potentials. However, severe degradation may happen at positive potentials. In Wang et al.'s work, it was shown that at above 0.35 V vs. RHE, MoS_2 decomposes to HSO_4^- and to MoO_2 (S) or MoO_3 (s) [158]. Remarkably, these potentials can happen, e.g., when placing MoS_2 in contact with an electrolyte at the OCP; Chen et al. and Ledendecker et al. reported sulfide dissolution at OCP up to 0.5 V in 0.1 M $HClO_4$ [101,159].

The Pourbaix diagram provided in Fig. 3 also shows that the region of stability of MoS_2 shrinks with the increase of the pH (towards alkaline values). Indeed, the interval between the hydrogen evolution line and the occurrence of dissolution increases. Region

14 in Fig. 3 shows the prevalence of molybdates in solution at a potential only slightly higher than the HER line (ca. 150 mV at pH 14). Even the cathodic stability region decreases with region 12 (Fig. 3), which corresponds to the decomposition to solid molybdenum and S_2^- which is roughly 200 mV lower than the HER lines. This finding supports the evidence that MoS_2 is not a stable electrocatalyst for the HER in an alkaline environment. However, care should be taken when drawing stability conclusions from the Pourbaix diagram. Deviations from Pourbaix predictions may happen for the absolute mass of the reactants in the environment, the volume and the flow rate of the electrolytes and/or for kinetics factors (e.g., the sluggish degradation of MoS_2 in acidic conditions for potentials lower than ca. −0.4 V RHE). We highlight that the Pourbaix diagrams can be experimental or calculated. Experimental data can be attainable but is not always available and may not be easy to obtain. Simultaneously, calculated diagrams derived from the density functional theory (DFT) may be accurate but the quality strongly depends on the selected function. At present, the SCAN functional seems to be the most accurate. Using SCAN potential overcomes the limitation of the stability that can be derived from the MP PBE potential [160]. Pourbaix diagrams analysis might be followed by experimental validation in actual conditions. An assessment of the reported Pourbaix has been done in acidic conditions by coupling potentiostatic tests of MoS_2 electrodes with chemical analysis of the electrolyte. This analysis showed that with MoS_2, the MP PBE functional cannot predict the actual stability of the material, while the Pourbaix determined with the use of the SCAN potential shows a larger adherence to the experimental evidence for dissolution [158]. The SCAN approach is the one that has been used to get Fig. 3 data.

6. Fabrication of MoS_2-based HER electrocatalysts

6.1. Hydrothermal growth

One of the routes vastly used for the synthesis of MoS_2 is the hydrothermal technique which is an important methodology of inorganic chemistry and includes the crystallization and growth from aqueous solutions at high temperatures and high vapor pressures. In this method, the reactants are sealed in an autoclave reactor and then the reaction is subjected to a chemical transmission to a high pressure at the temperature usually above the boiling point of the solvent which is mostly water. Due to the synergic effect of high pressure and increased temperature crystalline inorganic material can be produced as a single-step process. Compared to other state-of-the-art preparation methodologies for the growth of 2D materials, the hydrothermal offers several benefits such as cost-effectiveness, simple experimental setups, higher yield, ease to handle and optimize the reaction, convenience in tuning the morphologies and exposed edge states and compositing with other nanomaterials as hierarchical structures [161–163]. More importantly, the performance of the MoS_2 synthesized by the hydrothermal method has shown to be promising as a cathode electrocatalyst for HER. However, longer reaction times, lower crystallinity, and lesser uniformity in the achieved material could be possible challenges of this method [163–165]. Pu et al. hydrothermally grew MoS_2 thin film on the Mo foil (MoS_2/Mo) electrode which demonstrated impressive performance in acidic media (0.5 M H_2SO_4) by requiring an overpotential of 0.168 V at the current density (j) of 10 mA cm^{-2}, together with a remarkable operational durability of 17 h [166]. Moreover, the HER electrocatalytic activity of MoS_2 can be further improved by scientifically modifying the growth methods as discussed in the following sections. Constructing electrocatalytically active sites and phases, engineering the structural parameters, creating more intrinsic defects, and enhancing the reaction kinetics through doping and making heterojunctions are the featured strategies pursued in the paradigm of hydrothermal synthesis to improve MoS_2 performance. This method can be further classified into sub-synthesis techniques such as heat treatment, phase transformation, ion exchange, etc. In this section, various scientific attempts to improve the HER performance of the hydrothermally synthesized MoS_2 electrocatalyst are described. Table 1 summarizes the performance of the MoS_2-based electrocatalysts prepared through the hydrothermal growth method.

6.1.1. Engineering structure and morphology

As mentioned earlier, MoS_2 is a graphene-like 2D material whose basal surface is catalytically inactive. However, engineering the edge structure can improve the catalytic performance. Materials with structure-sensitive properties at the nanoscale can be constructed to improve the HER activity. Thus, decreasing the size of the material and lowering the dimensionality due to the quantum confinement effect, can enhance the electrocatalytic activity by increasing the edge sites [142,143]. The morphology and distribution of the electrocatalytically important edge sites of MoS_2 are found to be sensitive to the synthesis conditions. Kumar and coworkers by controlling process parameters of the typical hydrothermal method such as sulfur precursor and reaction temperature, developed MoS_2 with varying morphologies, for instance, nano-sheets, nano-capsules and nano-flakes [167]. Fig. 4(a–c) show field emission scanning electron microscopy (FE-SEM) images of three different MoS_2 materials obtained by varying the heating temperature of the autoclave. It is clear that each variant possesses its own intrinsic morphology, for example, the MoS_2 nano-sheet in Fig. 4(a) shows a thin sheet-like morphology whereas the MoS_2 nano-capsule in Fig. 4(b) has a capsule-like structure with 10–100 nm diameter. Moreover, it can be seen that a few of the damaged capsule walls indicate that capsules are made up of hollow inner space. Unlike the MoS_2 nano-capsule, a single MoS_2 flake was a few hundred nm in length as can be seen in Fig. 4(c). It is demonstrated that even though all three electrocatalysts were prepared through the hydrothermal procedure but a slight alteration in temperature and precursor type could lead to significant changes in the resultant nano-structures as well as morphologies of MoS_2 material. With the adopted methodology, they were able to increase the exposed edge sites which, in turn, ensured superior electrochemical performance under acidic conditions (0.5 M H_2SO_4). MoS_2 nano-capsules (S02) carried out HER with an overpotential ~120 mV (j = 10 mA cm^{-2}) as can be appreciated in Fig. 4(d) and remained stable when integrated into a single-cell PEM water electrolysis for 200 h [167].

The size of the nanostructures also plays an important role in determining the rate of electrocatalytic activity. For instance, small-size particle-like single atoms, clusters, and quantum dots (QDs) have higher electrocatalytic activity in comparison to their bulk [169–172]. By decreasing their size, the overall amount of exposed surface atoms is increased [173]. Mohanty et al. synthesized small-size and highly luminescent MoS_2 QDs (MSQDs) and MoS_2 nanosheets (MSNSs) by a simple hydrothermal method from single carbon-free ammonium tetrathiomolybdate [$(NH_4)_2MoS_4$] precursor as presented in Fig. 4(e) [168]. The as-synthesized MSQDs exhibited HER overpotentials of 0.210, 0.270, and 0.335 V (j = 10 mA cm^{-2}) with Tafel slope of 65, 78 and 116 mV dec^{-1} in 0.5 M H_2SO_4, 1 M KOH, and 1 M PBS, respectively, as demonstrated in Fig. 4(f–h).

6.1.2. Phase transition

As it was mentioned before, MoS_2 has different crystal phases. The most stable phase is 2H which is a semiconductor in nature

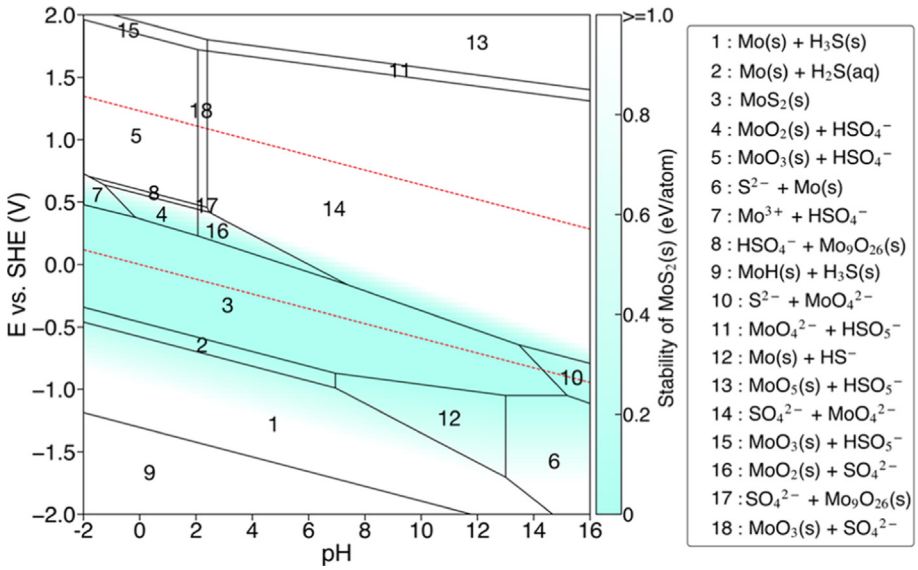

Fig. 3. Calculated Pourbaix diagram of MoS_2 in a 10^{-6} M sulfide concentration reporting the prevalent species in each pH-Potential region [158]. Reproduced with permission from Ref. [158]. Copyright 2021, American Chemical Society (ACS).

and restricts the electrocatalytic performance because of its relatively low conductivity. Thus, for having better HER performance and higher charge transfer kinetics, a metallic phase such as the distorted octahedral 1 T phase of MoS_2 is desired. In this way, sulfur atoms in the basal plane get activated and hence hydrogen absorption is enhanced compared to the 2H phase [174–176]. On the other hand, due to π-π van der Waals interaction, the 1 T phase is unstable and spontaneously converts to the 2H phase over time [177,178]. Lv et al. developed a facile one-step hydrothermal method to synthesize structurally stable ultra-thin 1 T MoS_2 in situ attached to graphene networks as schematically illustrated in Fig. 5(a) [179]. The synthesized 1 T MoS_2/ GO contains a 76.7% 1 T MoS_2 content. GO inhibits the transition from the 1 T phase to the 2H phase. Raman spectra of MoS_2/GO samples are shown in Fig. 5(b). For the 1 T MoS_2/GO, the peaks located at 147.1, 194.2, 235.5, 282.8 and 335.4 cm^{-1} correspond to the characteristic phonon vibration patterns of 1 T-phase MoS_2 [180,181]. The weak peaks at 376.1 and 403.4 cm^{-1} can be attributed instead to the inplane (E^1_{2g}) and out-of-plane (A_{1g}) vibration mode of 2H-phase MoS_2 [88,181]. The developed 1 T MoS_2/GO demonstrated a lower HER overpotential of 0.209 V (j = 10 mA cm^{-2}) with a Tafel slope of 45.5 mV dec^{-1} in 0.5 M H_2SO_4. (Fig. 5c and d). Xie et al. proposed hydrothermally fabricated defect-rich and ultrathin MoS_2 nanosheets with lateral sizes between 100 and 200 nm and nine S-Mo-S layers [182]. They designed a reaction involving high concentrations of precursors to stabilize the nanosheet morphology, and varying amounts of thiourea to induce the formation of a defect-rich structure. Such a strategy resulted in the partial cracking of the inert basal plane and exposed additional active edge sites. Thus, the achieved HER performance of defect-rich ultrathin MoS_2 in acidic media showed an onset overpotential of 0.120 V (j = 10 mA cm^{-2}) and a Tafel slope of 50 mV dec^{-1} in 0.5 M H_2SO_4 (Fig. 5e).

6.1.3. Heterojunction method

Structural adjustment and development for electrocatalytic performance can be realized by forming heterojunctions. The pivotal role of this strategy towards HER is the launching of additional electrocatalytic sites, which increase the reaction kinetics. Recently, Chen et al. reported the growth of starfish-like remarkable heterostructures of MoS_2/CoS with interface engineering on nickel foams (NF) as displayed in Fig. 6(a) [183]. Firstly, ZIF-67 was in-situ grown on the NF under ambient conditions and subjected to vulcanization to produce hollow frameworks of CoS polyhedrons which were subsequently modified by MoS_2 through hydrothermal reaction. The achieved MoS_2/CoS/NF HER electrode demonstrated the lower overpotential of just 67 mV at 10 mA cm^{-2} (Tafel slope of 56 mV dec^{-1}) along with outstanding stability in the alkaline medium (1.0 M KOH) as presented in Fig. 6(b). In another attempt, Hu et al. assembled MoS_2/NiCo-layered double hydroxide (LDH) heterostructures as highly efficient electrocatalysts by employing two facile and fast microwave hydrothermal processes [113]. LDHs, especially those based on Co, Fe and Ni are well-known as an emerging family of efficient electrocatalysts for oxygen evolution reaction (OER) in alkaline media, and can effectively adsorb hydroxyl species and catalyze their dissociation [185–187]. Using the as-obtained MoS_2/NiCo-LDH composite as an HER electrocatalyst, the reaction overpotential was remarkably reduced to 78 mV (j = 10 mA cm^{-2}) with a low Tafel slope of 76.6 mV dec^{-1} in 1.0 M KOH solution (Fig. 6c and d). Moreover, the MoS_2/NiCo-LDH demonstrated a marginal increase of just 3 mV in overpotential during chronopotentiometry measurements for 48 h at the current density of 20 mA cm^{-2} as clearly shown in Fig. 6(e). Another way to enhance the activity of MoS_2 is to make a heterojunction with nickel sulfides (NiS, NiS_2, and Ni_3S_2). This approach can also uplift the electrocatalytic stability under alkaline conditions. Moreover, due to the addition of nickel sulfides, these electrocatalysts also demonstrate their efficacy towards OER too and hence can be utilized as bifunctional electrocatalysts [188,189]. Some research has been done on Mo-Ni-based heterostructured bimetallic sulfides for alkaline water electrolysis and worth reading scientific endeavors can be found in the literature [190–192]. In this context, Liu et al. prepared a hybrid of non-stoichiometric nickel sulfide and MoS_2 (MoS_2@$Ni_{0.96}S$) through a facile one-step hydrothermal strategy followed by thermal annealing to obtain an electrocatalytically active interface for overall water splittings (Fig. 6f) [184]. The deconvoluted X-rays photoelectron spectroscopy (XPS) profiles of Mo 3d for the hybrid $Ni_{0.96}S$ and MoS_2 nanosheets shown in Fig. 6(g) indicated a negative shift in Mo^{+4}, $3d_{5/2,}$ and $3d_{3/2}$ peaks is due to the hybridization of MoS_2 [193,194]. The fitting analysis further (Fig. 6h) revealed the fact that two types of Ni $2p_{3/2}$ photoelectron peaks including Ni_{2p} and Ni_{3p} in pristine $Ni_{0.96}S$ give a positive shift in the $MoS_2Ni_{0.96}S$-1 h

Table 1
HER performance of the electrocatalysts fabricated via hydrothermal growth.

Sr. No.	Synthesis Controls	Strategy to improve HER	Overpotentials (mV) at j = 10 mA cm^{-2}	Tafel slope (mV dec^{-1})	Electrolyte	Ref.
1	Controlling the reaction temperature and sulfur precursor employed	Changing morphology by producing nano-capsule	120	–	0.5 M H_2SO_4	[167]
2	Used carbon-free ammonium tetrathiomolybdate [$(NH_4)_2MoS_4$] precursor	Production of MoS_2 quantum dots	210 in 0.5 M H_2SO_4 and 270 in 1 M KOH	65 in 0.5 M H_2SO_4 78 in 1 M KOH	0.5 M H_2SO_4 and 1 M KOH	[168]
3	Combining hydrothermal method with plasma treatment	Reducing the particle size	60	33	0.5 M H_2SO_4	[233]
4	Varying amounts of thiourea	Defects inducement	120	50	0.5 M H_2SO_4	[182]
5	Optimization of 2-MoS_2/CoS/NF	Interface engineering by making heterojunctions	67	56	1 M KOH	[183]
6	Combination of two fast microwave hydrothermal processes	MoS_2/NiCo-(layered double hydroxide) LDH heterostructures	78	76.6	1 M KOH	[113]
7	One-step hydrothermal method, followed by annealing at 400 °C	Hybrid of nickel sulfide and MoS_2	104	84	1 M KOH	[184]
8	Using rGO as a conductive support	MoS_2 particles decorated on rGO sheets	140	50	0.5 M H_2SO_4	[208]
9	The dual-step hydrothermal method associated with a facile selective etching	Use of conductive support by designing ZnS@C@MoS_2 core–shell nanostructure	118	55	1 M KOH	[216]
10	Composite electrocatalysts of g–C_3N_4/FeS_2/MoS_2 with bridging function of FeS_2	Fe-N and Fe-S bonding to increase the conductivity and restrict the MoS_2 agglomeration	193	87.7	0.5 M H_2SO_4	[221]
11	Ionic-liquid mediated synthesis of MoS_2/graphene composites	MoS_2/graphene composites where graphene as a conductive support	152	52	0.5 M H_2SO_4	[217]
12	Catkin carbonized with a pyrolysis method at 900 °C for 4 h under a nitrogen atmosphere.	Catkins/MoS_2 hybrids (conductive support)	136	62	0.5 M H_2SO_4	[224]
13	Atmosphere-controlled pyrolysis for waste carbonization.	MoS_2/CWM (heat-treated melamine wastes) nanocomposites	56	36.6	0.5 M H_2SO_4	[225]
14	Controlling the phase transformation	Graphene oxide (GO) inhibits the transition from the 1 T phase to the 2H phase	209	45	0.5 M H_2SO_4	[179]

hybrid [195]. The upshifting of Ni $2p_{3/2}$ binding energy and downshifting of Mo 3*d* binding energy in the hybrid strongly suggest the occurrence of a charge transfer process between $Ni_{0.96}S$ and MoS_2 due to the intimate heterojunction interfaces with strong electronic interactions in the hybrid. Such structural attributes help in dropping the binding energies of intermediates together with an improvement in electrocatalytic rates and thus overall electrocatalytic performance is enhanced. In this way, the developed MoS_2@$Ni_{0.96}S$ hybrid showed an HER overpotential of 104 mV (j = 10 mA cm^{-2}) with a Tafel slope of 84 mV dec^{-1} in 1.0 M KOH electrolyte [184].

6.1.4. Conductive supports

As detailed discussed above, one of the reasons behind the limited HER performance of MoS_2 is its low intrinsic electronic conductivity. This is because most of the edge catalytic sites in bulk MoS_2 are located adjacent to each other slowing down the electron transport [196–200]. It is known that the electrochemical performance of MoS_2 can be elevated by improving mass transfer and electron transportation [201]. Plenty of methods can be used for enhancing the electronic conductivity such as by improving the surface area, increasing the exposure of active edges, and the number of active sites in the electrocatalyst. Therefore, various efforts have been made to modify the characteristics of the material by coupling the MoS_2 with conductive supports like graphite, carbon paper, graphene nanosheets, Ni foam, graphene oxide, and carbon nanotubes [202–207]. Aditya et al. reported a novel synthesis of MoS_2 particles decorated on reduced graphene oxide (rGO) sheets [208]. The hydrothermal procedures were used at different stages of the synthesis pathway where graphene oxide was primarily synthesized by the Hummers' method [209]. Related to the MoS_2 nanoparticles on rGO sheets, the characteristic XPS deconvoluted peaks for Mo^{+4} (Fig. 7a) were identified at 229.3 and 232.4 eV. The Mo $3d_{3/2}$ and $3d_{5/2}$ are split into doublets with 0.9 eV separation due to the co-presence of 1 T and 2H MoS_2, at 232.2, 231.3, 230.2 and 229.3 eV, where the lower energy corresponds to the 1 T phase. This change in phase causes the enhancement in electron transfer because electron transfer is higher in a metallic environment compared to semiconductors. Therefore, the developed electrocatalyst performed outstanding HER in 0.5 M H_2SO_4 with 0.140 V overpotential (j = 10 mA cm^{-2}) and a Tafel slope of 50 mV dec^{-1}.

Similar work was done by Xu et al. on the HER activity of MoS_2 [210]. A typical defect-rich architecture containing nitrogen-doped reduced graphene oxide (rGO) with MoS_2 loading was prepared through a pyrolysis/hydrothermal step method as schematized in Fig. 7(b). The rGO and MoS_2 played a synergetic role in reducing the ΔG_H value to create favorable reaction states and eventually carried out HER with an overpotential of 0.102 V (j = 10 mA cm^{-2}) which was considerably lower compared to that of bare rGO. Another way of enhancing electrochemical performance is to shorten charge transport lengths and improve the surface area is combining the MoS_2 with porous carbonaceous nanostructures [211–214]. Not long ago, when Ge et al. presented a novel strategy to enhance the HER kinetics by vertically growing MoS_2 nanolayers on rGO with cross-bridging metallic ions that not only modulated the MoS_2 growth preferences but also acted as effective channels for the rapid charge transfer between MoS_2 and rGO [215]. Such a remarkable composite structure demonstrated superior HER in an acidic medium. Furthermore, Liu et al. adopted a dual-step hydrothermal bottom-up route in combination with a facile selective etching to design hierarchical ZnS@C@MoS_2 core–shell nanostructures [216]. In the first step, the core of zinc sulfide (ZnS) nanospheres were fabricated via a simple hydrothermal method and then ZnS@ Polydopamine (PDA) was prepared by the polymerization of dopamine in a Tris-buffer solution. In this way, a porous carbonaceous shell was coated on ZnS nanospheres when ZnS@PDA suffered from carbonization and selective etching in acidic conditions. Lastly, MoS_2 nanosheets were hydrothermally developed on ZnS@C mesoporous nanospheres to produce hierar-

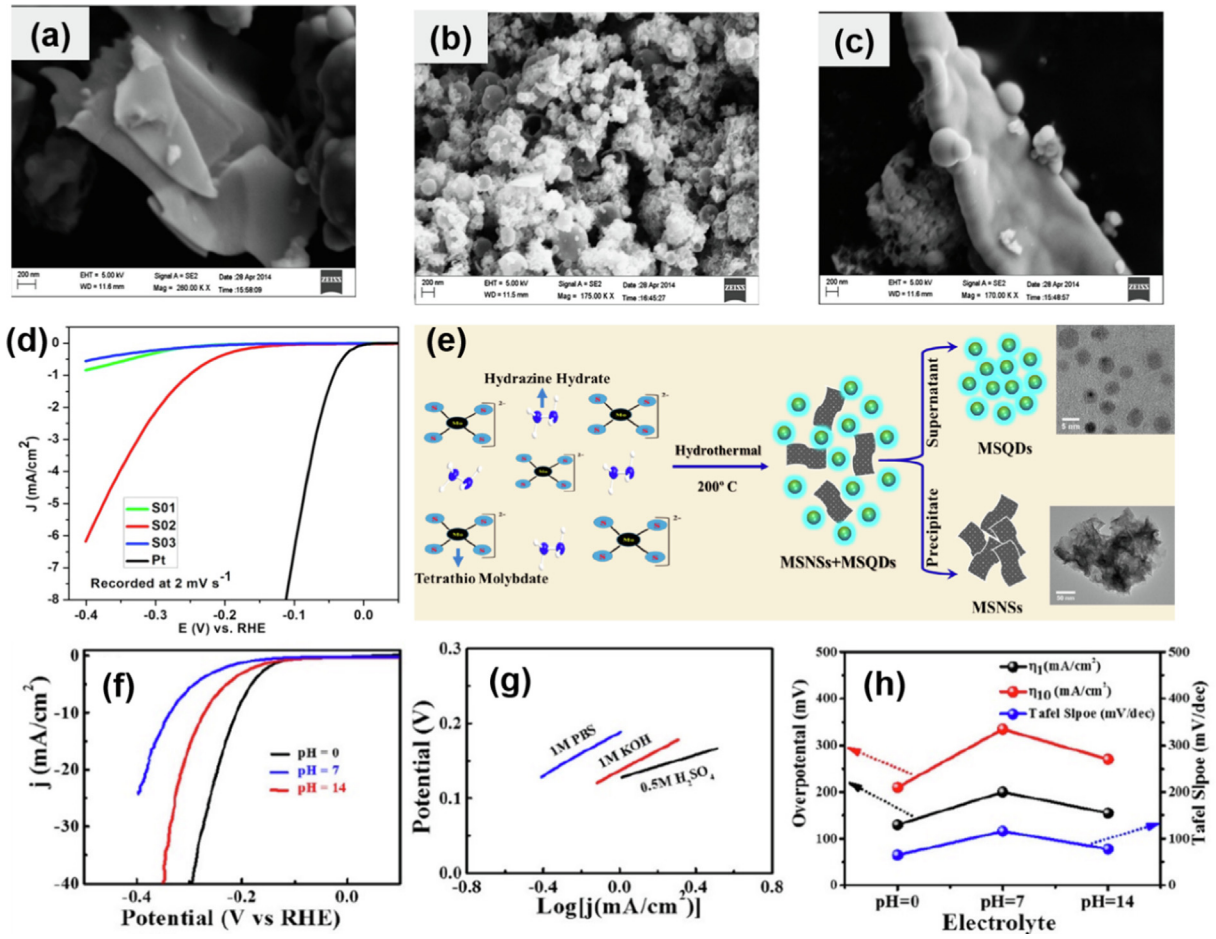

Fig. 4. FE-SEM images of (a) MoS_2 nano-sheets (S01), (b) MoS_2 nano-capsules (S02) and (c) MoS_2 nano-flakes with their corresponding HER performance (d) in N_2-rich 0.5 M H_2SO_4 [167]. Schematic representation of the synthesis process to prepare MSQDs and MSNSs (e). HER LSVs (at 5 mV s^{-1}) obtained by MSODs under different pH conditions (f), along with respective Tafel plots (g) and trends of overpotential & Tafel slope (h) at the current densities of 1 and 10 mA cm^{-2} [168]. (a–d) Reproduced with permission from Ref. [167]. Copyright 2016, Elsevier Ltd. (e–h) Reproduced with permission from Ref. [168]. Copyright 2020, American Chemical Society (ACS).

chical ZnS@C@MoS_2 core–shell nanostructures. From the SEM images, it can be understood that pure ZnS nanospheres were monodispersed and had spherical morphology but a rough surface with a diameter of about 280 nm is shown in Fig. 7(d). After coating PDA, the surface gets smoother and the diameter was enlarged (Fig. 7e). However, after being annealed and selectively acid-etched, ZnS@C kept a uniform spherical morphology but with a rough surface (Fig. 7f). After further hydrothermal treatment, MoS_2 nanosheets grew on ZnS@porous carbon to form the hierarchical ZnS@C@MoS_2 core–shell nanostructures as a whole (Fig. 7g). Finally, the hierarchical ZnS@C@MoS_2 performed HER with an overpotential of 0.118 V (j = 10 mA cm^{-2}) and a Tafel slope of 55.4 mV dec^{-1} which came out to be superior compared to pristine MoS_2 as shown in Fig. 7(g).

Ye et al. proposed another scheme to enhance the electronic conductivity and the number of active sites on the MoS_2 electrocatalyst surface [217]. In this work, the ionic liquid (IL, 1-butyl-3-methylimidazolium tetrafluoroborate ([BMIM]BF_4)) in the presence of graphene oxide was used to facilitate the formation of MoS_2/graphene nanocomposites (MoS_2/G-IL10) via a single-step hydrothermal method. This methodology provides up-wrapped sheets of MoS_2 with short slab lengths and discontinuous crystal fringes are well dispersed and anchored on the surface of the curved graphene. The developed MoS_2/G-IL10 demonstrated many de-layered MoS_2 sheets having shorter slab dimensions and irregular crystal fringes on the graphene's surface, which uplifted the number of active sites for HER. As a fact, carbon materials usually improve the HER performance of MoS_2 when combined with it [218–220]. Recently, Li et al. used a hydrothermal approach to develop an efficient HER electrocatalyst (g–C_3N_4/FeS_2/MoS_2) by growing MoS_2 nanosheets g-C_3N_4 substrates with FeS_2 sites as the bridging connections [221]. The chemical bonds such as the Fe–S bonds between MoS_2 and FeS_2 and the Fe–N bonds between g-C_3N_4 and FeS_2 acted as direct pathways for the charge transformation and improved the conductivity of the derived electrocatalyst. Besides performing the bridging function in the nanocomposite, FeS_2 sites confirmed the vertical growth of highly uniform MoS_2 nanosheets with exposed edges by restricting the agglomeration of nanosheets. Such attributes translated into an outstanding electrocatalytic activity with an overpotential of 193 mV and operational durability.

In the variety of carbon precursors, biomass is an interesting source, not only for its large specific surface area and hierarchical porous architecture but also for its high coverage of surface heteroatoms like O, P, etc. Biomass-based materials can be obtained at a low price and are environment-friendly and green [222,223]. Tong et al. worked on synthesizing the novel nanoflake-on-tubular microstructure containing ultrathin MoS_2 nanoflakes on carbonized catkin microtubes, named catkins/MoS_2 hybrids [224]. This method, by increasing the active sites and enhancing conductivity, improved the overall performance.

With a similar idea, Zhao et al. studied HER activities over the MoS_2/CWPU (polyurethane wastes) and MoS_2/CWM (heat-treated melamine wastes) nanocomposites which were synthesized by

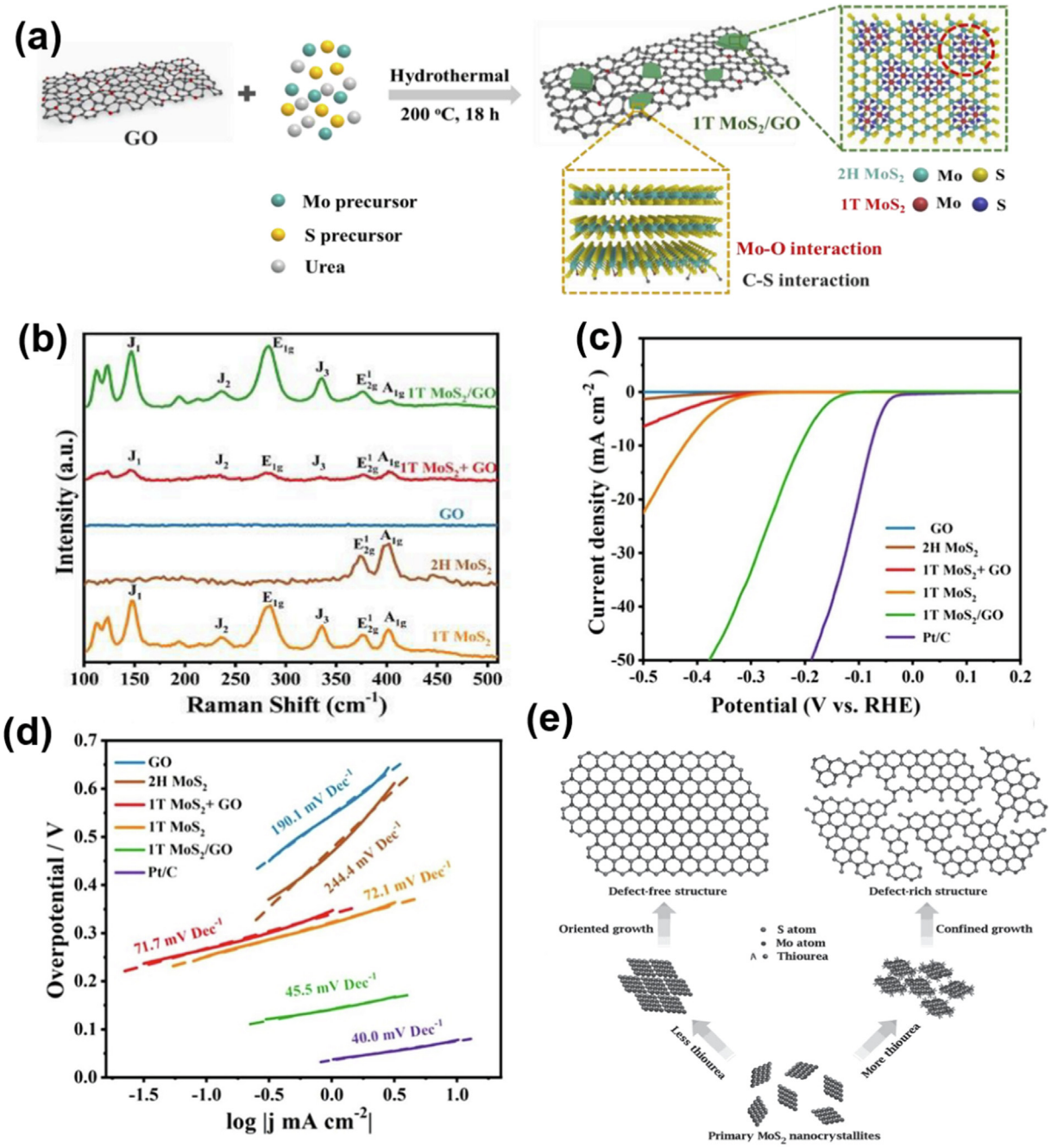

Fig. 5. Schematic illustration of the preparation process of 1 T MoS_2/GO composites through a hydrothermal strategy (a). Raman spectra (b) HER LSVs in 0.5 M H_2SO_4 (c) and corresponding Tafel curves (d) of GO, 1 T MoS_2/GO, 1 T MoS_2 + GO, 1 T MoS_2, 2H MoS_2 [179]. Fabrication routes (e) to obtain defect-free and defect-rich MoS_2 [182]. (a–d) Reproduced with permission from Ref. [179]. Copyright 2019, Elsevier Ltd. (e) Reproduced with permission from Ref. [182]. Copyright 2013, John Wiley and Sons.

atmosphere-controlled pyrolysis at 800 °C for 4 h to synthesize the CWM and CWPU support followed by a hydrothermal method for the synthesis of MoS_2/CWM and MoS_2/CWPU [225]. MoS_2/CWM 1:1 nanocomposite showed superior electrocatalytic performance for HER. The ultrathin nanosheets of MoS_2 demonstrated optimum electrical conductivity and plenty of active sites where the support with higher nitrogen content has rapid electron transfer and efficient hydrogen production. MoS_2/CWM 1:1 displayed an impressive overpotential of 56 mV (j = 10 mA cm^{-2}), a Tafel slope of 36.6 mV dec^{-1}, and a high exchange current density of 0.35 mA cm^{-2} along with long-term operational stability in 0.5 M H_2SO_4.

6.1.5. Plasma treatment

Surface structure and properties have paramount importance for HER performance. As explained earlier electrocatalytic activity of the material is more likely dependent on particle size, conductivity, and electrochemically active surface area. A way for surface modification is using the plasma which has reactive chemical species [226–229]. By creating defects, bandgap controlling, and enhancing electrical conductivity, plasma engineering has proven to have positive effects on improving HER in MoS_2 [230–232]. Niyitanga and Jeong used the plasma method for improving HER in the MoS_2 electrocatalyst [233]. MoS_2 was produced via the hydrothermal technique in combination with ambient plasma. Plasma was

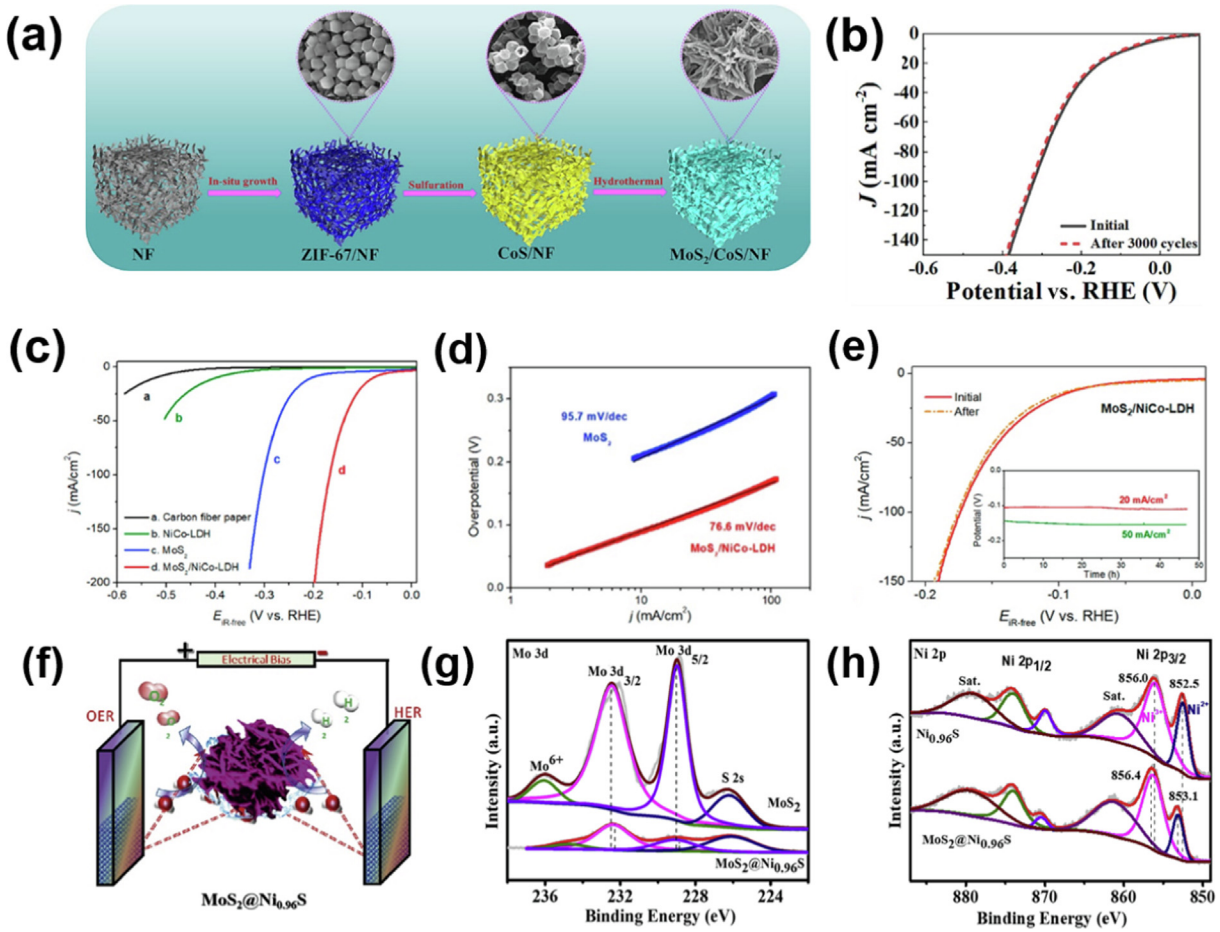

Fig. 6. Schematic of steps involved in the development of starfish-like MoS_2/CoS/NF heterostructure (a) and corresponding initial and 3000th HER polarization curves demonstrating the stability (b) [183]. HER polarization curves (c) of MoS_2/NiCo-LDH and other counterparts along with corresponding Tafel plots (d) obtained in 1 M KOH at a scan rate of 5 mV s^{-1}. LSVs obtained for MoS_2/NiCo-LDH before (solid line) and after (dotted line) the chronopotentiometry measurement (e) at −20 mA cm^{-2} of 48 h. whereas the recorded chronopotentiometry responses (η- t) at high current densities of 20 and 50 mA cm^{-2} are displayed in the inset [113]. MoS_2@$Ni_{0.96}S$ bifunctional hybrid for OER and HER (f) fabricated via a hydrothermal and annealing pathway. Deconvolution X-ray photoelectron spectra of (g) Mo 3*d* and (h) Ni 2*p* in the hybrid for $Ni_{0.96}S$ and MoS_2 [184]. (a and b) Reproduced with permission from Ref. [183]. Copyright 2022, Elsevier Ltd. (c–e) Reproduced with permission from Ref. [113]. Copyright 2017, Elsevier Ltd. (f–h). Reproduced with permission from Ref. [184]. Copyright 2020, Elsevier Ltd.

used to reduce the particle size of the electrocatalyst. The plasma treatment was done after hydrothermal synthesis of MoS_2, for different time durations (15, 30, 60, and 120 min) as shown in Fig. 8.

SEM micrographs given in Fig. 8(a) specify ~2 μm flakes of MoS_2 became fluffy after the plasma treatment, as illustrated in Fig. 8(b). In the meantime, H-MoS_2 had a lot of very small flakes in Fig. 8(c), and that larger chunk having tiny flakes reduced in size as the plasma treatment was done for 30 min, as shown in Fig. 8(d). The small flakes got evenly dispersed among chunks due to plasma treatment, as exhibited in the SEM micrographs of H-P-MoS_2 (60 min) and H-P-MoS_2 (120 min) in Fig. 8(e and f), expecting increased surface area as well as high electrocatalytic activity for HER. H-P-MoS_2 (120 min) gave the least overpotential of just 0.06 V with a small Tafel slope of 33 mV dec^{-1} in 0.5 M H_2SO_4. Where the plasma treatment modifies the morphological parameter it also affects the surface chemistry and therefore can alter the electrode/electrolyte interaction [234–236]. Tao et al. induced various physical and chemical defects in the 2D MoS_2 using Ar and O_2 plasma treatment that improve the HER performance of the derived electrocatalysts due to enhanced affinity between electrode and electrolyte [234]. Although the morphological effects of Ar and O_2 plasma treatment were similar, O_2 plasma increased the valency of molybdenum due to the generation of MoO_3, specifying the oxygen inducement in the MoS_2 structure by making Mo–O bonds. Similarly, the oxidation of sulfur increased up to + 6 which indicated the presence of S–O bonds. Such oxygen incorporation via plasma treatment benefited the hydrophilicity by reducing the contact angle from 96.5° of pristine MoS_2 to 48.4° of plasma-treated MoS_2 that in turn reduced the charge transfer resistance and uplifted the HER kinetics.

6.2. Chemical vapor deposition

In the last decade, novel TMDCs such as MoS_2 prepared by chemical vapor deposition (CVD), have attracted scientific attention because of their unique properties and tremendous potential applications in various domains. In CVD solid nanomaterials can be effectively deposited on the substrate by chemical gas or vapor-phase reaction taking place on or in a close vicinity of the heated substrate. The nanomaterials could be in the form of single crystals, amorphous power and thin films whereas their physiochemical properties can be altered by varying experimental conditions. No doubt, the previously discussed technique of hydrothermal synthesis of MoS_2 provides ease and cost-effectiveness due to the absence of highly expensive types of equipment and requirements of the vacuum. However, the precision in the dispersion, morphology, stoichiometry and surface coverage may remain challenging. Moreover, the involvement of long

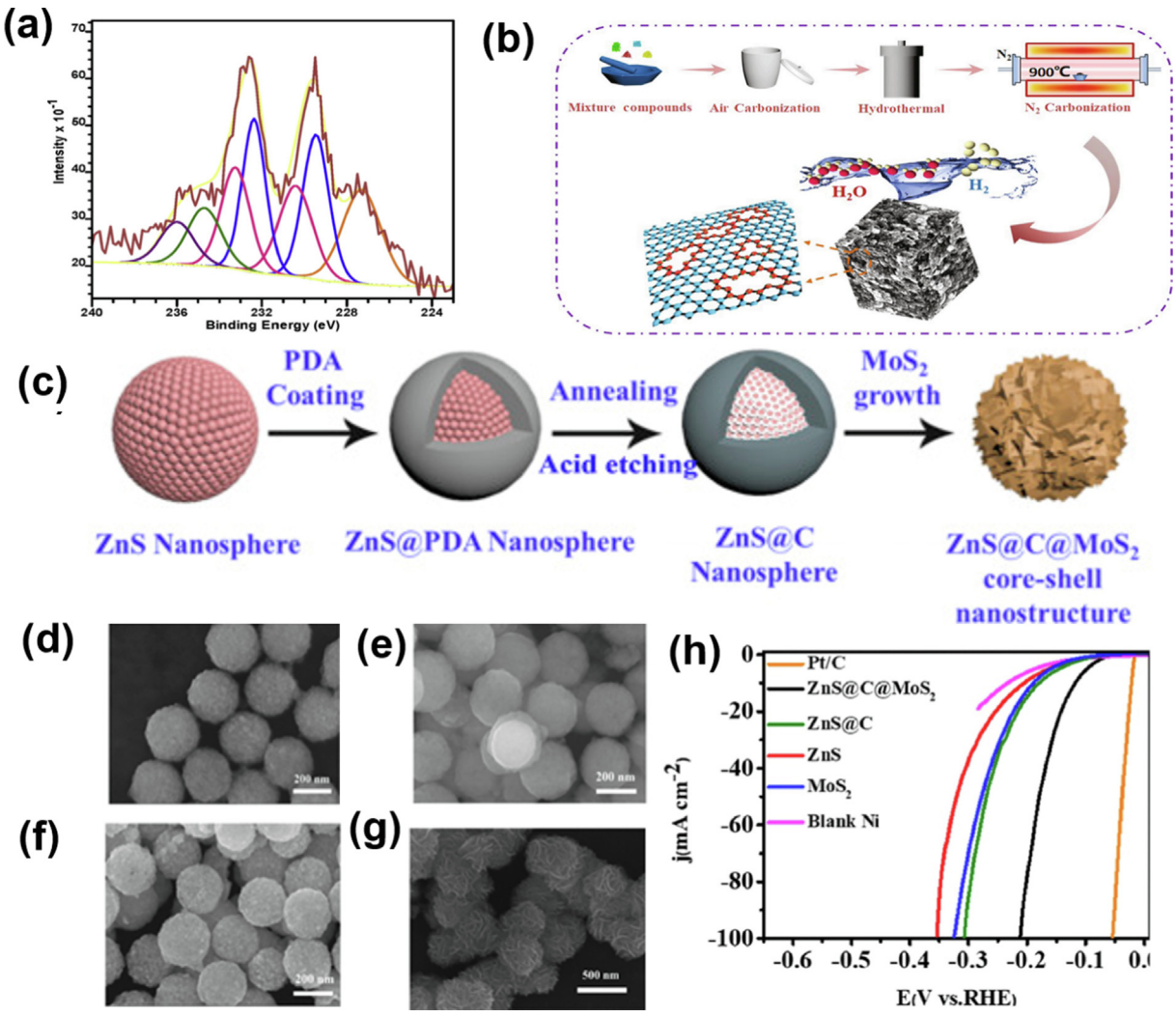

Fig. 7. XPS spectra of Mo 3*d* in $MSRGO_2$ (a) [208]. The schematic preparation process of the RGO/MoS_2 composite (b) [210]. The preparation of hierarchical ZnS@C@MoS_2 core–shell nanostructure (c) and SEM images of (d) ZnS, (e) ZnS@PDA, (f) ZnS@C and (g) ZnS@C@MoS_2 along with a corresponding HER performance in (h) [216]. (a) Reproduced with permission from Ref. [208]. Copyright 2016, Elsevier Ltd. (b) Reproduced with permission from Ref. [210]. Copyright 2021, Elsevier Ltd. (c–h) Reproduced with permission from Ref. [216]. Copyright 2019, Elsevier Ltd.

reaction times, as long as 24 h and the requirement of dangerous precursors, i.e., molybdenum chloride might lead to low efficiency and potential hazards, respectively [236]. In parallel to other methods, CVD provides an opportunity to grow atomically thin MoS_2 while being compatible with advanced industrial fabrication technologies and paves the way for conformal, cost-effective, homogeneous, and highly pure production [237,238]. CVD typically involved lower vapor pressure that ensures a uniform flow of vapor precursors and hence homogeneous growth of the materials is evolved [239]. Controlling the CVD parameters such as modifications in the synthesis steps, optimization of growth temperatures, precursor designing and substrate engineering, the characteristics of derived 2D material can be tuned according to the demands of the application [240]. During MoS_2 film deposition via CVD, sometimes maintaining the smooth uniformity of film thickness due to the concentration gradient of the precursor vapors over the substrate could be challenging, however, by optimizing the process parameters such issues can be resolved. In the upcoming section strategic endeavors to uplift the HER capability of MoS_2-based electrocatalysts through CVD as a governing methodology have been summarized.

6.2.1. Structural modifications during CVD

Another effective approach to upturn the HER activity is to increase the given geometric area. Li et al. used a scalable single-step CVD to deposit highly porous thin films consisting of edge-rich MoS_2 nanoplatelets on a wide range of substrates, including silicon wafers, glassy carbon, graphite, and single-wall nanotubes [241]. To separately control the temperature of MoO_3 and S precursors that were in powder form, a two-zone method was used. The deposition was carried at 830–900 °C. The schematic setup for CVD growth is shown in Fig. 9(a). The tilted SEM micrograph of the sample deposited at 866 °C (while keeping the deposition time for 120 min) in an Ar atmosphere (Fig. 9b), showed the evolution of multilayered nanoplatelets. The observation of nanoplatelets perpendicular to the substrate proposes the stacking of previously formed layers of smaller platelets under the larger nanoplatelets. Hence the film had three regimes: a bottom layer consisting of very fine crystals with an average size of less than 0.5 μm, the middle layer containing crystals of intermediate size (mostly between 1–2 μm), and finally the uppermost layer carrying the platelets of ~5 μm. In another attempt, Ruiz et al. prepared MoS_2 vertically standing nanosheets by metal–organic CVD (MOCVD) employing molybdenum hexacarbonyl and 1,2-ethanedithiol as precursors

[242]. By depositing the films at different temperatures (T_{dep} between 500 and 800 °C), the effects of different surface morphologies, from nanoparticles to vertically standing nanosheets were investigated. XPS of MoS_2 films composed of nanoparticles and nanosheets prepared at all deposition temperatures is demonstrated in Fig. 9(c). The left figure shows Mo 3*d*and S 2*s* peaks on the left whereas the S 2*p* peaks are demonstrated in the right fig. All the XPS peaks shifted to lower binding energy with decreasing deposition temperatures. MoS_2 film prepared at 600 °C exhibits the lowest value of overpotential (0.355 V (j = 10 mA cm^{-2})), where the Tafel slope varied from 68 to 94 mV dec^{-1} in 0.5 M H_2SO_4 (Fig. 9d). This indicates the definitive effects of microstructural attributes on the final electrochemical performance. The carbonaceous matter has been considered the main reason causing the shifting of Mo and S peaks to lower energies in the XPS spectra due to the interaction between carbon and MoS_2 [243–245]. Carbon has been recognized as a factor to degrade the electrocatalytic activity due to coke poisoning on the active sites [246]. As we know that active site in MoS_2 is the sulfur-rich edge of the nanosheet, while the basal planes are inert. Therefore, the vertically standing nanosheets with smaller carbon content and larger edge density would have higher electrocatalytic performance.

Although remarkable attempts have been made to achieve large-area MoS_2 monolayers, it is not straightforward to obtain high crystalline quality continuous monolayer films. Thus, growing a large grain size MoS_2 monolayer in the bare CVD process remains a challenge. It has been reported that the growth of MoS_2 is very sensitive to the prior substrate treatment. Since the amorphous SiO_2 substrate is not the best candidate to grow large-area thin crystalline film on it, thereby, exploiting seeding promoter molecules on the substrate could enhance the planer nucleation of MoS_2 [247]. In this regard, the usage of organic promoters such as perylene-3,4,9,10-tetracarboxylic acid tetra potassium salt (PTAS) during the CVD process has contributed to lowering the free energy for nucleation and consequently a possible decrease in the growth temperature [248–250]. Among different promoters, alkali metal halides (AMH) like NaCl, KBr, and KCl are beneficial for the suppression of the nucleation of new MoS_2 domains on the substrate and may also have an electrocatalytic role to increase the surface reaction rate [251–253].

Zhu et al. investigated the HER activity of salt-templated low-pressure CVD-grown MoS_2 nanosheets using NaCl micro-sized cubic crystal powders as three-dimensional (3D) templates [254]. Higher growth temperature can accelerate the volatilization of Mo precursor, and thus increase the nucleation density of MoS_2 on the crystal facets. This fact can explain why MoS_2 nanosheets occurred on the facets of NaCl crystals, and their coverage was increased with the increasing growth temperature. SEM images of NaCl@MoS_2 powders which were grown at 550 °C can be appreciated in Fig. 9(e and f). For these samples, the electrocatalytic HER performance showed the overpotential of 0.30–0.36 V (j = 10 mA c m^{-2}) and a Tafel slope of 87.6–103.9 mV dec^{-1} in 0.5 M H_2SO_4 electrolyte which tended to uplift by increasing the growth temperature due to enhanced nanosheet thickness.

The number of edge sites in MoS_2 can also be increased by synthesizing large-area MoS_2 with dendritic architecture, which has a desirable edge-rich monolayer structure. Xu et al. performed an atmospheric pressure CVD (APCVD) to tailor the substrate construction and the monolayer MoS_2 evolved from triangular to dendritic morphology because of the change in growth conditions [255]. The monolayer dendrites showed strong photoluminescence, indicating direct band gap emissions sustained after being transferred. However, post-transfer S-annealing restored the structural discontinuities and lowered the extent of n-type doping in MoS_2 monolayers. Basal plane with superior crystallinity and dendritic edges were also observed in the optical microscopic and SEM visualizations. MoS_2 dendrites after annealing exhibited optimum and stable HER performance with a large current density of 32 μA cm^{-2}.

Depositing nanocrystals (NCs) or QDs with extremely low dimensions (size below < 5 nm) could also be an exciting strategy to increase the edge sites and make the maximum usage of surface area that can definitely benefit the HER activity. NCs or QDs of MoS_2 are traditionally developed through colloidal chemistry or molecular beam epitaxy in Stranski–Krastanov growth fashion. Although such methodologies can give acceptable crystallinity, the removal of organic ligands attached to the QDs from colloidal solution is not an easy task and also homogeneous dispersion of QDs on the substrate is difficult, eventually leading to inferior electrocatalytic activities [256,257]. Moreover, during the epitaxy method, the growth of TMDCs in the Stranski – Krastanov fashion is undesirable due to the weak van der Waals interaction of the depositing TMDCs with the substrate. To mitigate such problems, recently, Wang et al. grew single-layer MoS_2 NCs with particle size ca. 5 nm on the sapphire substrate with full surface coverage using CVD. Monodispersed and abundance of exposed edges remarkably improved the HER activity with an onset potential of 50 mV and Tafel slope of 57 mV dec^{-1} [258].

6.2.2. Heterostructures via CVD

To improve the electrical conductivity and increase the density of active sites, Nikam et al. proposed very efficient 3D heterostructures with MoS_2 nanosheets on conductive MoO_2 [259]. Both the backbone of the conductive oxide layer of MoO_2 and the 3D MoO_2 structure that create structural disorders in MoS_2 nanosheets, cause to facilitate interfacial charge transport and expose tremendous active sites, respectively. Low-pressure CVD (LPCVD) was used for the 3D MoS_2/MoO_2 heterostructures synthesis. The metallic 3D MoO_2 cores were grown using a commercially available carbon cloth as substrate scaffold followed by the formation of distorted MoS_2 nanosheets on metallic 3D MoO_2. The synthesized 3D MoS_2/MoO_2 hybrid demonstrated an overpotential of 142 mV (j = 10 mA cm^{-2}), a low Tafel slope of 35.6 mV dec^{-1}, and superior durability in 0.5 M H_2SO_4 electrolyte.

In another work, Wan et al. made an effort to enhance the activity performance not only by improving the conductivity but also by increasing the number of active sites [260]. Thus, the fractal-shaped single-layer MoS_2 with large tensile strain was directly synthesized on fused silica, then transformed the MoS_2 on the graphene substrate. The electrocatalytic capability of the developed 2D hybrid heterostructures was influenced due to the synergic combination of electrocatalytically active MoS_2 edges and highly conductive graphene. CVD with a dual-temperature-zone system that used sulfur and MoO_3 as precursors, was used to grow fractal-shaped single-layer MoS_2.

Zhou et al. studied the MoS_2/WTe_2 heterostructure using an electrochemical microreactor to investigate the role of the interface between the monolayer of MoS_2 in the semiconducting 2H phase and the monolayer of WTe_2 in the metallic T_d phase [261]. The MoS_2/WTe_2 heterostructure can exhibit improved HER activity due to a lower Schottky barrier at the interface, improved contact due to the large area heterointerface, and reduced electron transport pathways. Transmission electron microscopy (TEM) characterization of the MoS_2/WTe_2 hybrids (Fig. 10a and b) shows few-layer MoS_2 nanosheets intimately anchored on WTe_2 nanoflakes. High-resolution TEM images show MoS_2 interlayer spacing of 0.62 nm (Fig. 10b), suggesting that the MoS_2 layers are oriented vertically as well as horizontally with respect to the WTe_2 flakes. Fig. 10(b) shows the WTe_2 (020) plane spacing of 0.30 nm. Based on TEM analysis, ultrathin MoS_2 layers whose layer alignment is vertical to the WTe_2 flakes appear dominant over the horizontal layer alignment. Such attributes lead MoS_2/WTe_2 to deliver HER

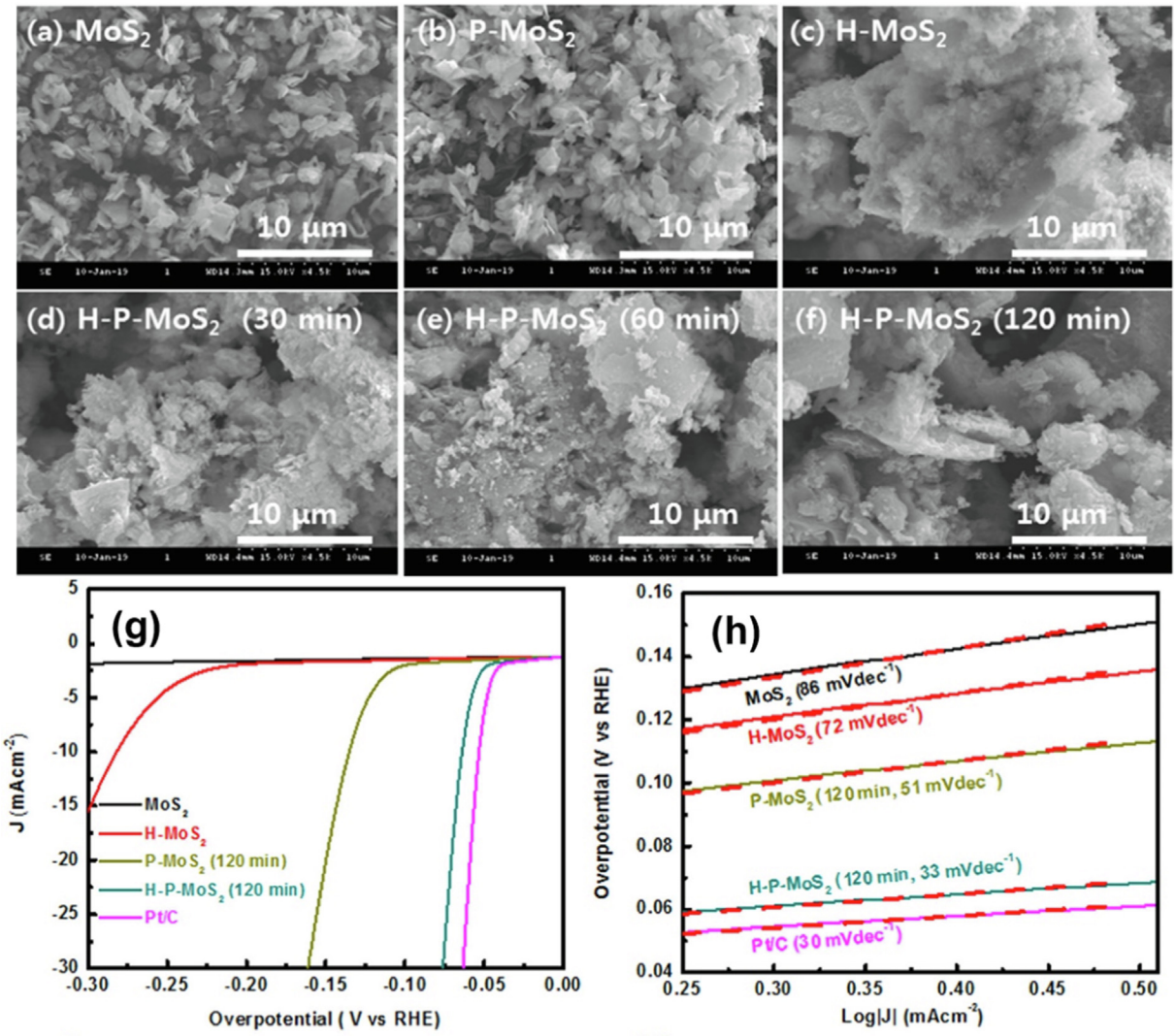

Fig. 8. SEM images of (a) MoS_2, (b) P-MoS_2, (c) H-MoS_2, (d) H-P-MoS_2 (30 min), (e) H-P-MoS_2 (60 min) and (f) H-P-MoS_2 (120 min). HER polarization curves (g) and the corresponding Tafel plot (h) of the aforementioned samples in 0.5 M H_2SO_4 [233]. Reproduced with permission from Ref. [233]. Copyright 2019, Elsevier Ltd.

overpotential of 0.14 V (j = 10 mA cm^{-2}) with a Tafel slope of 40 mV dec^{-1} in 0.5 M H_2SO_4.

In another study, Yu et al. worked on the synthesis of the MoS_2/VS_2 hybrid by in situ growing the MoS_2 micro flowers on the VS_2 micro flakes using a single-step CVD process (Fig. 10c) [262]. An improvement was observed in the HER activity of the hybrid electrocatalyst due to the formation of lightly vanadium-doped MoS_2 as vanadium dopants can effectively enhance the in-plane electrical conductivity and intrinsic activity of MoS_2 simultaneously. Raman spectra of the MoS_2/VS_2 hybrid, pristine MoS_2, and VS_2 are shown in Fig. 10(d). The in-plane vibration mode (E^2_{1g}) and out-of-plane vibration mode (A_{1g}) of the pristine MoS_2 which were at ~382.8 and ~408.4 cm^{-1}, respectively, red-shifted to ~381.1 (E^2_{1g}) and ~407.3 cm^{-1} (A_{1g}) after thermal hybridization with VS_2 [263,264]. This observation indicated the incorporation of vanadium dopants into the MoS_2 matrix. Also, the vibrational frequency difference between A_{1g} and (E^2_{1g}) of the MoS_2/VS_2 hybrid (25.6 cm^{-1}) was far greater than the typical value of the monolayer of MoS_2 (18 cm^{-1}), revealing its bulk state structure [265]. The A_g and E_g vibration peaks of the VS_2 were not observed in the MoS_2/VS_2 hybrid because of the full coverage of on-top MoS_2 micro flowers. The MoS_2/VS_2 required an overpotential of 199.6 mV (j = 10 mA cm^{-2}) while the HER capability of the pristine MoS_2 and VS_2 remained at the overpotential of 330.8 and 259.7 mV (j = 10 mA cm^{-2}), respectively in 0.5 M H_2SO_4 (Fig. 10e).

With a similar idea, Oh et al. established a 3D heterostructure based on MoS_2 and graphene stack on carbon cloth with outstanding HER performance due to the superior electrochemical activity and stability of carbon-based materials like graphene [266]. In this study, they exploited sequential growth steps, in which nickel electrodeposition was performed on carbon cloth (CC), followed by thermal CVD growth of graphene on top of Ni/CC pre-deposited stack to achieve Graphene/CC. The sequential 3D heterostructure of MoS_2 and graphene can provide a platform with increased active edge sites. The TEM image in Fig. 10(f) taken from the magnified view of the selected area presented in Fig. 10(g), shows the MoS_2 with a d-spacing of 0.27 nm on the multiple layers of graphene with a d-spacing of 0.34 nm. The surface changed from activated carbon of CC to CVD-grown graphene due to the deposition of graphene on CC is reflected in the formation of the 2D peak with large full width at half maximum (FWHM) in the Raman spectra obtained from the MoS_2/Gr/CC stack (Fig. 10h). In addition, the Raman shift separation of E_{2g} and A_{1g} peaks (~27 cm^{-1}) confirms the formation of bulk MoS_2 (Fig. 10i). MoS_2/Gr/CC exhibited encouraging HER activity with an overpotential of 91 mV (j = 10

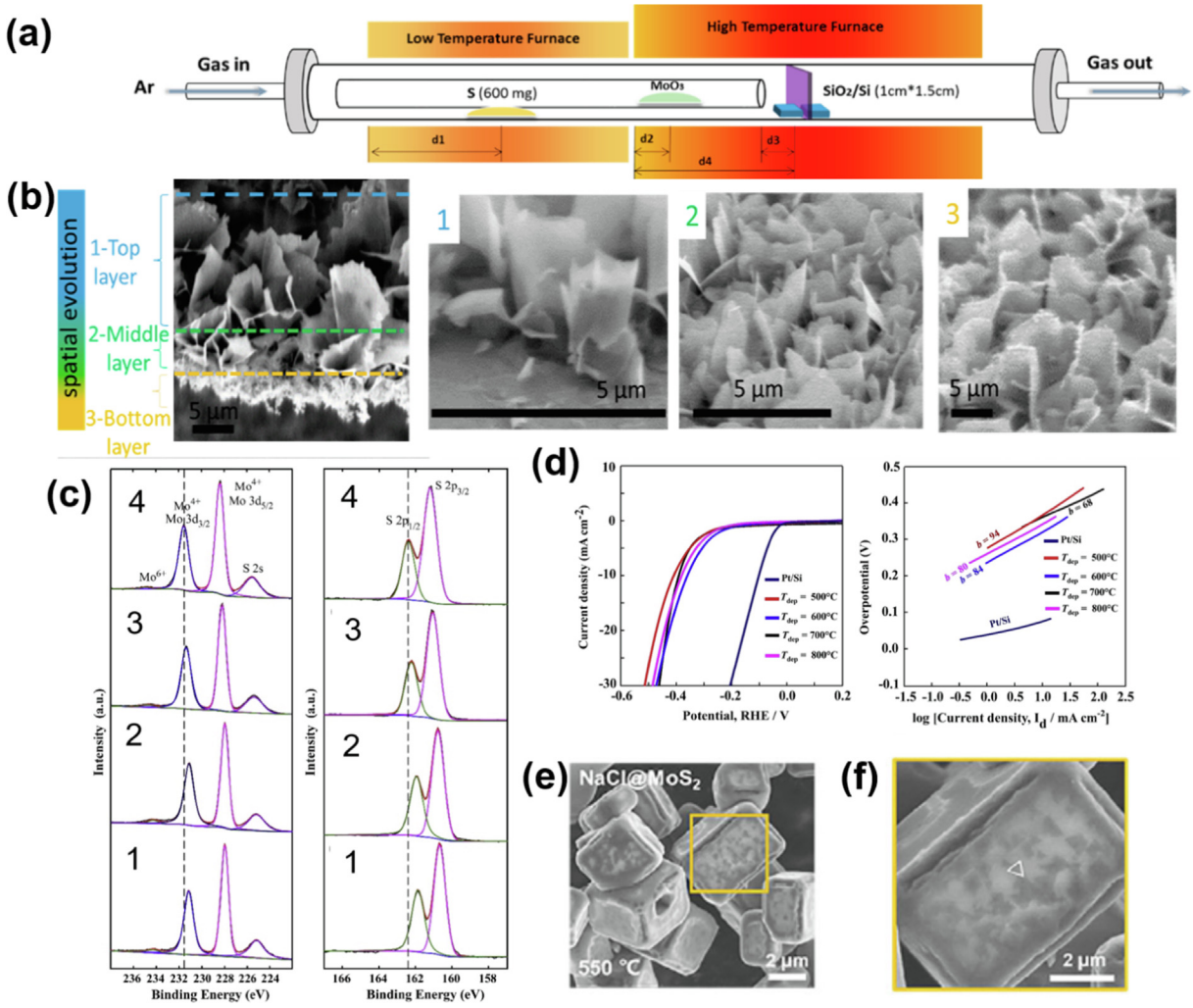

Fig. 9. Atmospheric pressure CVD synthesis of an edge-exposed MoS_2 nanoplatelet network on various substrates (a). Spatial growth of MoS_2 thin-film perpendicular to the substrate surface, having three layers of varying platelet sizes (as indicated by dashed lines) (b) [241]. XPS spectra of MoS_2 films (c) prepared at deposition temperature = (1) 500, (2) 600, (3) 700 and (4) 800 °C. LSVs and Tafel plots (d) of MoS_2 films deposited on Au foil at different temperatures [242]. SEM images (e and f) of NaCl@MoS_2 powders (grown at 550 °C for 20 min) [254]. (a and b) Reproduced with permission from Ref. [241]. Copyright 2017, American Chemical Society (ACS). (c and d) Reproduced with permission from Ref. [242]. Copyright 2018, Elsevier Ltd. (e and f) Reproduced with permission from Ref. [254]. Copyright 2020, Springer Publishing Group.

mA cm^{-2}) and a Tafel slope of 48 mV dec^{-1} with 48 h stability in 0.5 M H_2SO_4.

Another work by Yang et al. reported an efficient method of synthesis for a $MoS_{2(1x)}Se_{2x}$ ternary alloy using CVD on carbon nanofibers (CNFs) as the substrate and utilized them directly as hydrogen evolution cathodes which showed a 144 mV dec^{-1} Tafel slope [267]. This means that the reactions follow the Volmer-Heyrovsky or the Volmer-Tafel process with the Volmer reaction as the RDS. It was also proposed by Huang et al. to sulfurize drop-coated $CoCl_2/MoCl_5$ substrates to obtain vertically aligned Co-doped MoS_2 nanosheet arrays with excellent electrocatalytic activity thanks to the high electron mobility in the basal planes [268]. The authors reported that tuning of $CoCl_2$ concentration in $CoCl_2$-$MoCl_5$ precursor impacts the nanosheet density, due to the sulfur vapor diffusion direction. For the vertically grown Co-doped MoS_2-2 array, the as-grown nanosheets are parallel to the sulfur vapor diffusion direction, whereas, for the Co-doped MoS_2-3 array, the growth direction is not guaranteed (Fig. 11a). HRTEM image of the Co-doped MoS_2-2 array deposited on graphite foil substrate (Fig. 11b and c) shows (100) planes of hexagonal crystalline MoS_2 with a lattice spacing of 0.27 nm and the intersection angle of lattice fringe of 60 °C. Due to the high amount of active sites in the Co-doped MoS_2 nanosheet, it demonstrated an overpotential of 185 mV (j = 10 mA cm^{-2}) and a Tafel slope of 65 mV dec^{-1} in 0.5 M H_2SO_4.

Gnanasekar et al. utilized CVD to develop the heterostructures of NbS_2/MoS_2 vertical nanosheets grown on carbon nanofiber (CNF) with a high aspect ratio (Fig. 11d) [269]. As presented in Fig. 11(e and f), FE-SEM micrographs show the bare CNF with a high rough surface of the carbon nanofiber and tiny NbS_2 nano patches that are homogenously distributed on vertically aligned MoS_2 nanosheets grown on CNF. Fig. 11(g) shows ultra-thin MoS_2 nanosheets with a thickness ranging from 0.6 to 3.9 nm corresponding to the presence of 1–5 layers of MoS_2. Other dark patches of NbS_2 with a radius of 50 nm were observed over MoS_2 nanosheets. Fig. 11(h) illustrates NbS_2 patches forming over MoS_2 with interplanar distances of 0.286 and 0.27 nm and clear lattice fringes corresponding to NbS_2 (yellow) and MoS_2 (red) planes. The developed NbS_2/MoS_2 electrocatalyst exhibited outstanding HER activity with low overpotentials i.e., 0.23, 0.21, 0.33 V in acidic, neutral and alkaline conditions, respectively, measured at j = 50 mA cm^{-2}.

6.2.3. Substrate effect

Li et al. found that substrates can affect the electrocatalytic activity of MoS_2 in two ways [270]: (1) change in the chemical nature of MoS_2 through charge transformation i.e., proximity doping, (2) the development of an interfacial tunneling barrier with MoS_2. Outstanding electrocatalytic performance with the monolayer MoS_2 films was realized by employing the substrates that can induce n-type doping in MoS_2, i.e., Ti and give rise to low interfacial tunneling barriers with MoS_2. For the synthesis by the self-limiting CVD method, molybdenum chloride ($MoCl_5$) powder and sulfur powder were used as the precursors. By controlling the growth temperature in the range of 700–900 °C, the density of sulfur vacancies could be controlled [271]. Also, the authors managed to control the layers number of the films by using different amounts of $MoCl_5$ [272]. MoS_2 films onto various conductive substrates were transferred by using a surface-energy-assisted transfer method [273]. Raman and XPS results are similar everywhere for as-grown films but exhibit an obvious difference for the films transferred onto different substrates. The A_{1g} Raman peak red-shifted with the density of electrons (n-doping level) of MoS_2 indicating obvious variation among the monolayer films on the different substrates [274] as illustrated in Fig. 12(a). XPS peaks collected from the MoS_2 films Fig. 12(b), which were known to shift to higher energy with n-doping, indicated that the n-doping level of the film is the highest on Pt substrates and lowest on gold and this observation was consistent with the Raman measurement [274,275]. The HER measurement in 0.5 M H_2SO_4 clarified the influence of the substrate on the overall electrochemical performance, as the film on Ti substrate exhibited HER activity similar to that of bare Pt. Whereas the film on the Pt substrate further improved the performance as can be seen in Fig. 12(c and d).

6.2.4. Magnetic improvement

Generally, improving electron transfer is one of the main objectives of enhancing the HER activity of electrocatalysts. Until today, many studies refer to a significant change in the nonmagnetic ground state of semiconductor TMD nanomaterials, caused by imperfect structures of TMDCs [276–279]. One of these approaches is to introduce ferromagnetic properties in 2D MoS_2 through nanostructure designing followed by applying an external magnetic field on ferromagnetic MoS_2 to improve the electron transfer efficiency and trigger the magnetic enhancement of HER.

Zhou et al. designed the ferromagnetic bowl-like MoS_2 flakes by using a modified step-by-step CVD method with a tilted substrate [280]. The magnetic HER enhancement happens when an external vertical magnetic field is employed over ferromagnetic bowl-like MoS_2 flakes and electrons transmit easily from the glassy carbon electrode to active sites to drive HER. The step-by-step CVD synthesis, schematically shown in Fig. 12(e and f), used a tilted SiO_2/Si substrate, a tube furnace system with S and MoO_3 as precursors and high-purity Ar as carrier gas. In Fig. 12(g) magnetization versus magnetic field (M–H) trends for the bowl-like MoS_2 flakes and reference CVD-grown bilayer MoS_2 flakes on Si substrates measured at 5 K have been presented. Different from the bilayer MoS_2 flakes, the magnetic results here clearly show the evolution of ferromagnetism for bowl-like MoS_2 flakes. The ferromagnetically (with external vertical field) grown bowl-like MoS_2 delivered the best HER activity by giving an overpotential of 0.113 V (j = 10 mA cm^{-2}) and a Tafel slope of 59 mV dec^{-1} in 0.5 M H_2SO_4.

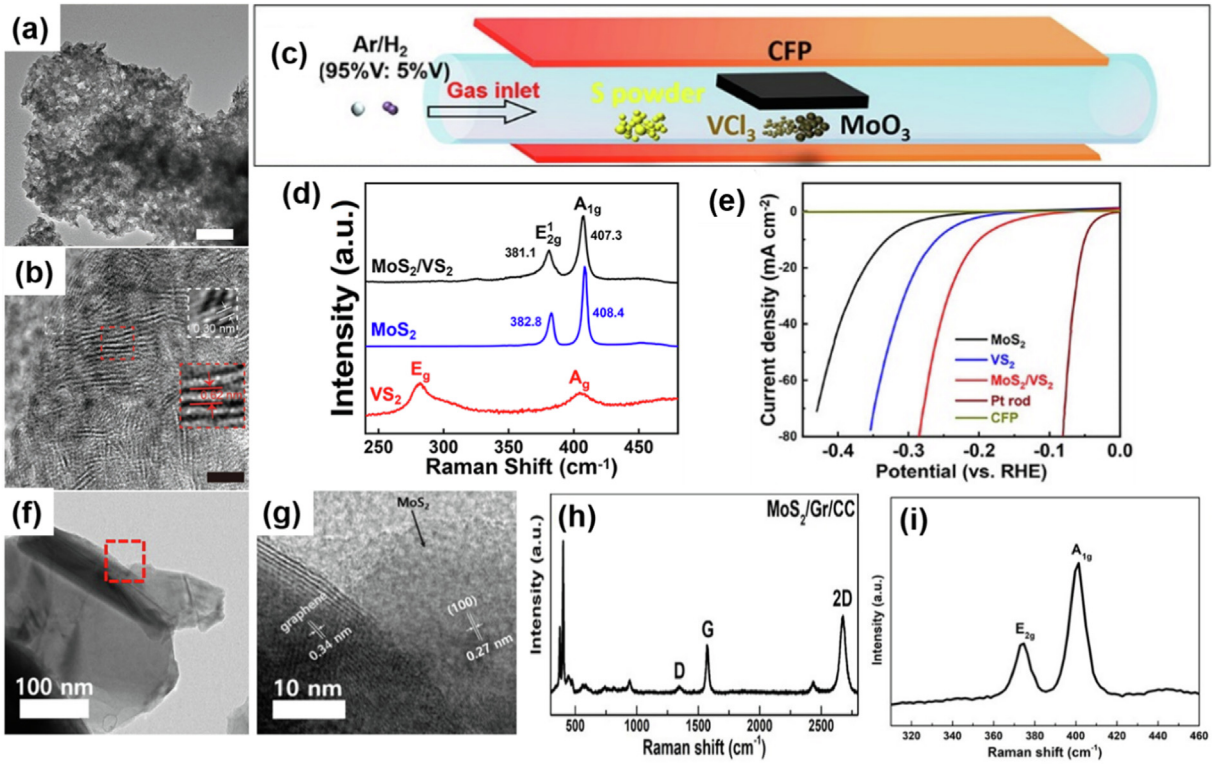

Fig. 10. TEM image (a) of a MoS_2/WTe_2 with a scale bar of 100 nm at lower magnification. HRTEM image (b) of a MoS_2/WTe_2; scale bar, 5 nm. The inset of micrograph (b) indicates the lattice spacing of 0.62 and 0.3 nm, corresponding to the (002) plane of MoS_2 and (020) plane of WTe_2, respectively [261]. Schematic representation (c) of MoS_2/VS_2 fabrication via a one-pot CVD process. Raman spectrographs (d) of MoS_2/ VS_2, MoS_2, and VS_2 and their HER performance (e) in 0.5 M H_2SO_4 [262]. FE-TEM micrograph (f) shows a small grain of MoS_2/Gr/CC while the magnified view (g) shows d-spacings of MoS_2 (0.27 nm) and graphene (0.34 nm). Raman spectra of MoS_2/Gr/CC (h) with D, G, and 2D peaks, indicating the existence of sp^2 carbon on the surface. Raman spectra of MoS_2/Gr/CC (i) showing the E_{2g} and A_{1g} modes of MoS_2 [266]. (a and b) Reproduced with permission from Ref. [261]. Copyright 2019, John Wiley and Sons. (c–e) Reproduced with permission from Ref. [262]. Copyright 2018, Elsevier Ltd. (f–i) Reproduced with permission from Ref. [266]. Copyright 2020, Elsevier Ltd.

6.2.5. Doping and morphological engineering of MoS_2 via CVD

In the recent past, Xu et al. communicated a defect engineering approach to boost the HER activity of basal planes of 2D MoS_2 by inducing Frenkel defects [281]. First MoS_2 monolayer was deposited via CVD and then annealed in the Ar atmosphere for a short period of time at 400 °C which causes the spontaneous migration of Mo atoms from the lattice positions to interstitial locations leaving atomic vacancies behind. Hence, an outstanding charge distribution was introduced due to such Freckle defects that made the interstitial Mo atoms more prone to optimal H adsorption and ensure subsequent reduction in the overpotential (164 mV at J of 10 mA cm^{-2}) in 0.5 M H_2SO_4 [281].

Doping has been largely studied in MoS_2-based electrocatalysts as the doped MoS_2 is more stable at operative conditions. Dopants while acting as defects in MoS_2 introduce midgap states close to the Fermi level which alters the spatial homogeneity of electronic states, thus generating the extra electrocatalytic sites. In the event of atom replacement, localized electronic states are generated directly by the heteroatom or by the alteration of the bond length and bond angle in the lattice. In the case of vacancies, they are generated by the electronic reorganization of unsaturated bonds around the vacancy [140]. Importantly, a limited density of dopants has no relevant effects on the long-range crystalline structure of the materials.

The substitutional doping of some Mo atoms in MoS_2 with Pd may improve electrocatalytic activity for HER [282]. Another approach involves nonmetal doping, e.g., substituting a sufficient number of S with Se in MoS_2 [135,283]. In defective MoS_2 sulfur vacancies change electron distribution in the proximity of Mo atoms, mainly within a few Å radius surrounding the vacancies, which gives rise to localized midgap states below the minima of the conduction band [284,285]. Electrocatalytic activity is generally proportional to the density of active sites and thus to the defect density. On the other hand, as discussed earlier, defects can significantly reduce the electrical conductivity which may negatively impact the kinetics and thus the turnover frequency of the electrochemical reactions. The ideal condition can be obtained by accurate defects engineering, paying particular attention to the defect spatial distribution and the main distance. Pak et al. changed the energy band structure of the MoS_2 monolayer by employing the p-doping and n-doping in the MoS_2 monolayer, for controlling carrier densities in a MoS_2 monolayer which led to modifying MoS_2 electrochemical performance [286]. Doping the MoS_2 monolayer with octadecyltrichlorosilane (ODTS) and (3-aminopropyl)-triethoxysilane (APTES) to produce p-doping and n-doping samples, respectively resulted in the raising and/or lowering of the Fermi levels as demonstrated in Fig. 12(h). The electron-rich MoS_2 exhibited a drop in overpotential and Tafel slope in comparison with the MoS_2 having surface functionals. The overpotential for APTES-MoS_2 came out to be 382 mV (j = 10 mA cm^{-2}) while the Tafel slope was calculated at 110 mV dec^{-1} under acidic conditions. Very recently, Son et al. developed a facile way for the doping of MoS_2 basal plan with vanadium concentration as high as 16% due to reactivity enhancement effects of the mixed precursors of transition metals during the intermediate-reaction-mediated CVD process [151]. It was observed that a high concentration coalescence of atomic vanadium realized the availability of the plentiful states near MoS_2 fermi levels which instigate the transformation of n-type semiconducting characteristics of MoS_2 to the metallic state together with optimization of the ΔG_{H^*} of V-MoS_2 to the near-zero level. In this way not only did the basal plane got activated but the electrical conductivity was considerably enhanced. These factors guarantee the outstanding performance of V-MoS_2 with an overpotential of 100 mV and a low Tafel slope of 36 mV dec^{-1} where the remarkably good TOF (14.2 s^{-1}) confirmed the boosting of the intrinsic activity of MoS_2 via coalesced doping of vanadium atoms.

6.3. Chemical and electrochemical etching

Li et al. exploited two approaches for gas phase etching of the CVD-grown vertically standing MoS_2 nanoplates to maximize the usage of electrode area and activation of the electrocatalytically inert basal plane [287]. As a defect engineering approach for improving the HER performance of MoS_2 flakes, the oxygen (O_2) plasma exposure and hydrogen (H_2) annealing indicated that H_2 etching resulted in an increase in HER performance due to the creation of efficient active sites and a higher surface area. O_2 plasma led to the formation of a less active MoO_x phase in the electrocatalyst system and negatively impacted the HER activity. H_2 annealing as a defect engineering approach demonstrated higher performance compared to the O_2 plasma exposure. The H_2-annealed defect-rich MoS_2 electrocatalysts showed a Tafel slope of 94 mV dec^{-1} and low onset overpotential of 193 mV (j = 10 m A cm^{-2}) in 0.5 M H_2SO_4. Another efficient defect-creation method was developed by Zhang et al. in which electrochemically active sites in MoS_2 were increased by combining the chemical etching with O_2 plasma pretreatment [288]. In order to etch CVD-grown monolayer MoS_2 samples, a low concentration of NaClO solution was used in which the edges were etched after 5 min. The etching of CVD-grown MoS_2 after chemical activation showed etched edges after 10 min where centers remained unetched, confirming that the dangling bonds at the MoS_2 edge are more active. Whereas for some CVD-grown MoS_2, the etching started in the basal plane rather than the edge.

Active sites can also be generated electrochemically by transferring the proton and electron to the sulfur atoms in the basal plane which causes desorption of H_2S(g) leaving behind an S-vacancy [137]. Despite some problems of defect clustering, the density of electrochemically generated defects can be controlled by acting on the ramp of applied potential at the electrode. The process allowed the fabrication of up to ca. 25% defects in the basal plane of MoS_2. Above this value, the conductivity of MoS_2 is compromised and desorption became difficult. Remarkably, electrochemical etching can be combined with several electrochemical lithographic techniques [289], such as parallel local oxidation [290]. These methods allow spatial control with a resolution of a few tens of nanometers. A summary of HER activity demonstrated by different MoS_2-based electrocatalysts derived via CVD involving routes has been presented in Table 2.

6.4. Exfoliation

Typically, there are two main methods for 2D TMDCs, especially MoS_2, the top-down and the bottom-up approaches. Compared with the top-down method, bottom-up synthesis offers more opportunities to engineer the structure of MoS_2 nanomaterials. However, top-down strategies such as exfoliation, are efficient ways to obtain nanoscale MoS_2 with more exposed edges due to the abundance of bulk MoS_2 (molybdenite) in nature. Aiming at the technological exploitation of 2D materials, the development of approaches to synthesize large-scale and high-quality films is mandatory and here exfoliation can provide a way to obtain very clean and crystalline nanosheets of atomic-level thickness [291]. Many studies reported the synthesis of ultrathin crystals but with limited lateral extension (in the micrometer range) using mechanical and chemical exfoliation, or solution-based chemical approaches [292]. It can be regarded as the easiest way to obtain MoS_2 single crystals due to the weak Van der Waals bonds between the layers that can be broken during mechanical exfoliation. It was also the first method to isolate a monolayer of graphite in 2004 by using scotch tape [293]. However, this method does not have control over the flakes' thickness, shape, or size, and also results in low yield [291]. On the other hand, liquid exfoliation based on mixing

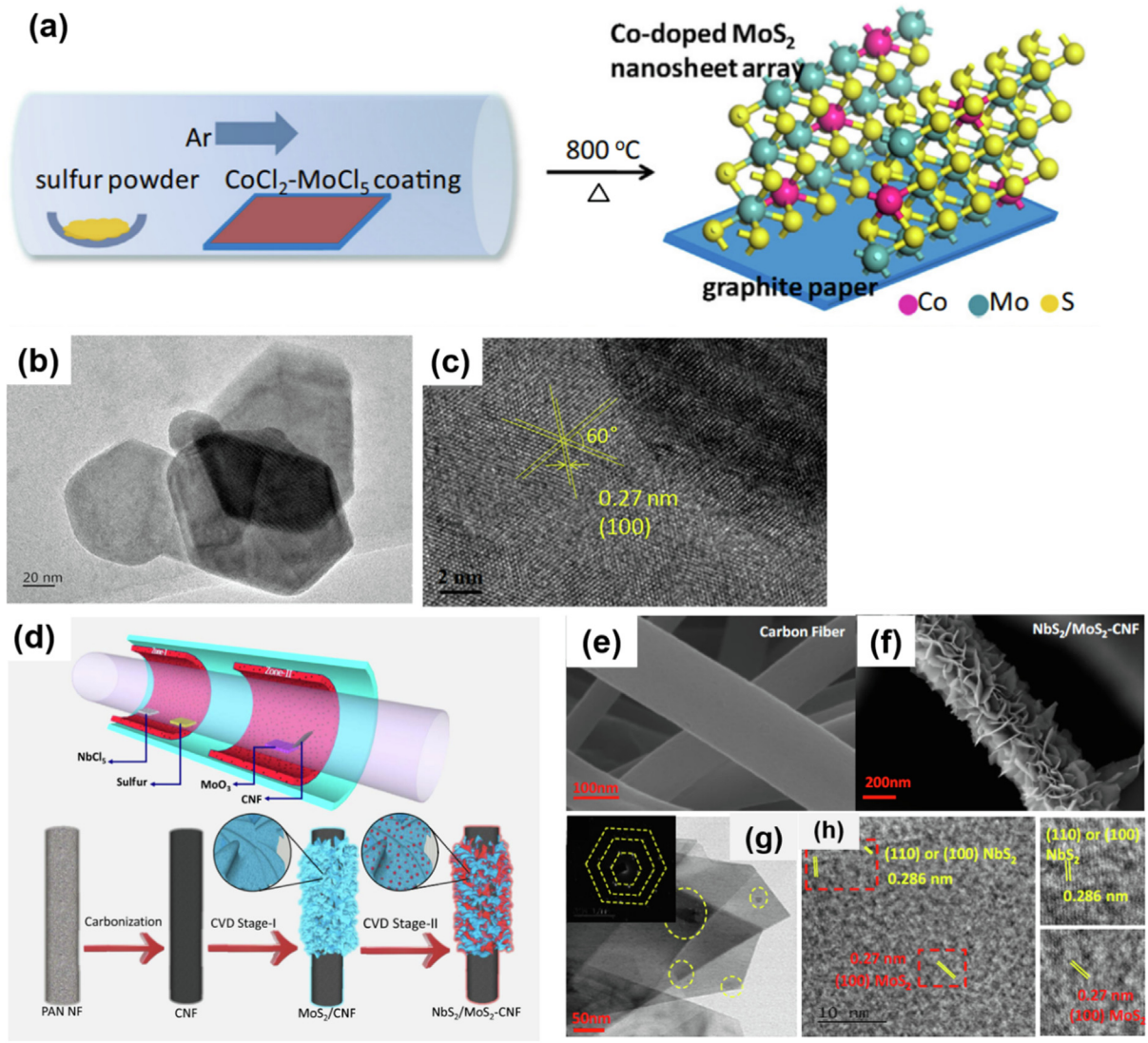

Fig. 11. Fabrication pathway and as-developed Co-doped MoS_2 (a). TEM image of Co-doped MoS_2-2 (b) and its analogous HRTEM (c) [268]. Schematic demonstration (d) of single-step CVD synthesis of NbS_2/MoS_2-CNF hybrid electrocatalyst. FE-SEM images of (e) bare CNF, (f) NbS_2/MoS_2-CNF. (g and h) TEM and HRTEM micrographs of NbS_2/MoS_2-CNF [269]. (a–c) Reproduced with permission from Ref. [268]. Copyright 2019, Elsevier Ltd. (d–h) Reproduced with permission from Ref. [269]. Copyright 2020, American Chemical Society (ACS).

and dispersing materials in a solution allows the production of MoS_2 flakes with a controllable thickness. To overcome the inferior quality of typical exfoliation, an intercalation-assisted exfoliation pathway can be adopted [70]. This can be carried out by reacting the intercalating agent of cations, i.e., lithium with powdered MoS_2. In this way, a violent reaction takes place between water and protons carrying solvent followed by a stripping process. Finally, through ultrasonic extraction high-quality single-layer MoS_2 can be achieved. Intercalation can twice increase the lattice parameter 'c' of MoS_2 by decreasing the Van der Waal forces of pristine MoS_2 and hence single layer 1 T phase becomes stable whereas the substitution of intercalating atoms induces sulfur vacancies that synergistically improve the HER performance. Wu et al. analyze the stabilization and HER performance enhancement of 1 T MoS_2 due to the adsorption and intercalation of lithium [294]. In addition to intercalation, the adsorption of lithium uplifts the HER activity of the derived electrocatalyst. The intercalation of lithium induces the phase 2H to 1 T phase transformation, which confirms the electronic conductivity, the lithium adsorption promotes the HER active edge sites by favorably modifying the ΔG_{H^*}. However, the traditional lithium intercalation inevitably requires organolithium agents for instance *n*-butyllithium (*n*-BuLi) and the severe reductive potential of *n*-BuLi may cause the decomposition of the $LiMoS_2$ precursor to metallic molybdenum [295,296]. To overcome this limitation, Zhao et al. synthesized exfoliated monolayers of MoS_2 through the intercalation of zero-valent TMs, i.e., cobalt, nickel and copper under mild conditions that effectively avoided the unwanted material decomposition during intercalation-assisted exfoliation [295]. The MoS_2-based electrocatalysts developed using exfoliation pathways have been summarized in Table 3.

6.4.1. Morphological engineering via exfoliation

For promoting more active sites and accelerating electron/ion transmission in MoS_2 nanosheets, Li et al. used an efficient and scalable method consisting of ball-milling in combination with liquid-phase exfoliation [297]. They used ammonium bicarbonate as an exfoliation aid to accelerate the delamination and pulveriza-

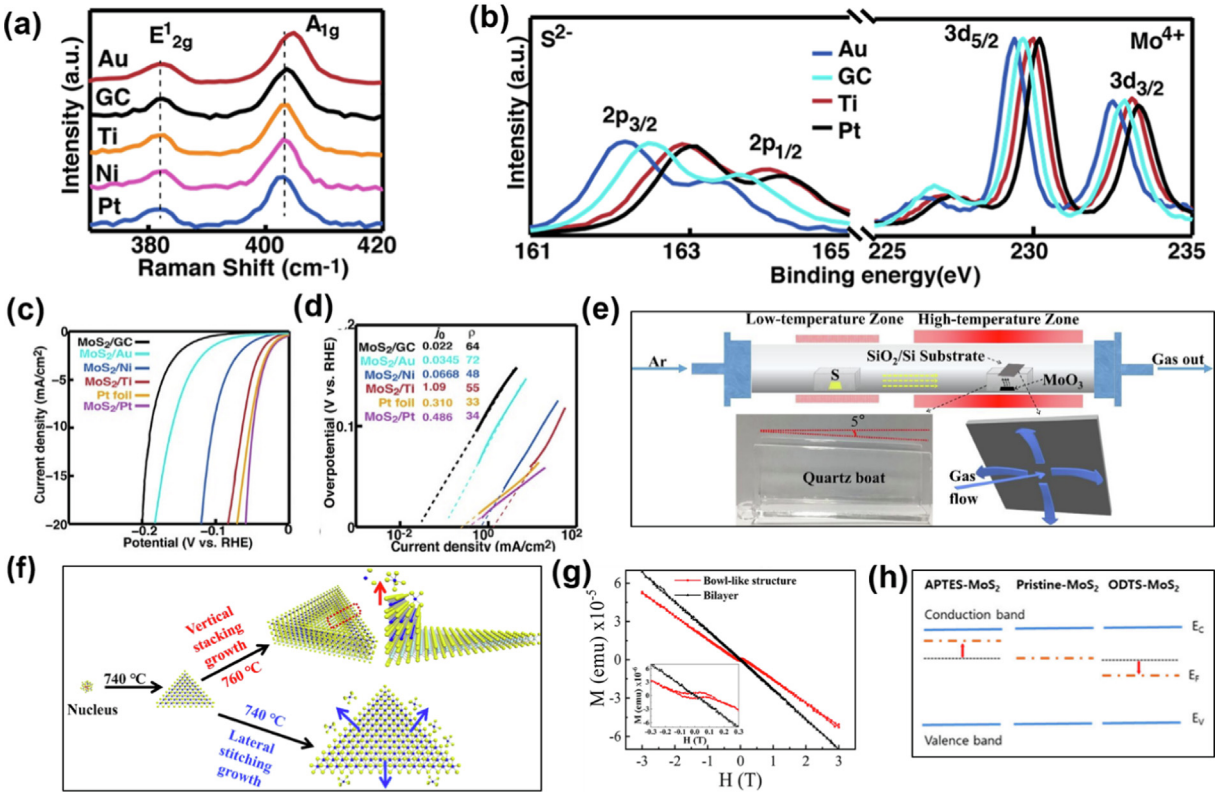

Fig. 12. Raman spectra (a) of the monolayer MoS_2 films on Au, glassy carbon (GC), Ti, Ni, and Pt substrates. The dashed lines indicate the position of the E^1_{2g} and A_{1g} peaks of the film on Ti substrates. XPS spectra (b), HER polarization curves (c) and Tafel plots (d) of MoS_2 films on different substrates [270]. Synthesis route (e) of bowl-like MoS_2 flakes while the schematic illustration of lateral stitching and vertical stacking growth of MoS_2 flakes is presented in (f). Magnetic hysteresis loop (g) at 5 K for bowl-like MoS_2 flakes and reference CVD-grown bilayer MoS_2 flakes (the inset is an expanded view of the same magnetic hysteresis loop at 5 K) [280]. Energy band diagram (h) of MoS_2 monolayer depicting the change in the Fermi-level upon surface functionalization with either ODTS or APTES [286]. (a–d) Reproduced with permission from Ref. [270]. Copyright 2019, American Chemical Society (ACS). (e–g) Reproduced with permission from Ref. [280]. Copyright 2020, American Chemical Society (ACS). (h) Reproduced from Ref. [286]. Under Creative Commons Attribution (CC BY) license (http://creativecommons.org/licenses/by/4.0/).

tion of bulk MoS_2 during preparation. Then, the ball-milled MoS_2 was further exfoliated by high-speed shear-exfoliation (H-MoS_2NS) to obtain MoS_2 nanosheet dispersion with high concentration. Most H$eMoS_2$NS have lateral dimensions less than 150 nm. The H-MoS_2NS mixed with multiwalled carbon nanotubes (MWCNT) could form H-MoS_2NS/MWCNT composites with a good conductive network, which is a prerequisite for suitable an HER electrocatalyst (Fig. 13a). Because cavitation during sonication only occurs at specific locations, it is still difficult for applying sonication in the industrial preparation of MoS_2 nanosheets. Thus an easy operating method such as the high-speed dispersion homogenizer was used to shear-exfoliate the bulk MoS_2 [298,299]. When bulk MoS_2 was shear-exfoliated for 2 h, the concentration of MoS_2 nanosheets was as high as 0.64 mg mL^1 (i.e., H-MoS_2NS). About 94% of the H-MoS_2NS were below 150 nm in the lateral dimension as shown in Fig. 13(b). Also, most H-MoS_2NS had irregular edges, which could expose more edge active sites for enhancing the HER activity. The HRTEM image of the H-MoS_2NS in Fig. 13(c) showed that the interlayer spacing of H-MoS_2NS was significantly enlarged, resulting in discontinuous edge streaks [300]. The best performance for this method belongs to the H-MoS_2NS/MWCNT composites which contain 56 wt% H-MoS_2NS. It had an overpotential of 284 mV (j = 10 mA cm^{-2}), a Tafel slope of 97 mV dec^{-1}, and good stability in 0.5 M H_2SO_4.

6.4.2. Defect inducement and doping during exfoliation

In a different work, Li et al. designed MoS_2 nano-meshes with homogeneously dispersed holes and defects to effectively utilize the 2H-MoS_2 basal planes through a combination of the ball-milling and ultrasonic methods [301]. The obtained electrocatalyst had a monolayer, porous and defective structure, which maximized performance for both electrocatalytic and photocatalytic evolution of hydrogen (Fig. 13d). The HRTEM images of pristine MoS_2 and MoS_2 nano-mesh are given in Fig. 13(e–h). The atomic arrangement at the basal surface got considerably disturbed after ball-milling and ultrasonic processes and even short-range ordering of nanodomains was not clearly observed. That is because these clusters and atoms are highly mobile and thermodynamically prone to form a disordered structure of MoS_2. The pristine MoS_2 nanosheets have perfect crystals while the MoS_2 nano-meshes have a completely disordered atomic arrangement. The disordered structure makes the MoS_2 nano-mesh more stable, and there are more dangling bonds available to provide active sites for higher HER performance [302]. Li et al. developed MoS_2 nano-mesh that possessed homogeneously dispersed holes and defects to activate 2H-MoS_2 basal planes by benefiting from the combination of ball-milling and ultrasonic methods. It showed impressive HER activity (overpotential of 160 mV (j = 10 mA cm^{-2})) with a low Tafel slope of 46 mV dec^{-1} in 0.5 M H_2SO_4 [301].

As it is obvious, increasing the electrical conductivity and the amount of exposed active sites improves the performance of the electrocatalyst. Wei et al. performed a one-step electrochemical exfoliation strategy to fabricate 2D Ni-doped MoS_2 nanosheets (Ni-EX-MoS_2) [303]. The synthetic route for Ni-EX-MoS_2 is presented in Fig. 13(i). High-resolution XPS spectra given in Fig. 13 (j) showed two characteristic peaks corresponding to Mo $3d_{5/2}$ and Mo $3d_{3/2}$ present in the 2H phase of bulk MoS_2 [304,305]. On the other hand, Ni-EX-MoS_2 showed three characteristic peaks of

Mo^{6+}, Mo $3d_{5/2}$, and Mo $3d_{3/2}$, respectively [305,306]. The reduction in the binding energy was perhaps because of the shifting of the Fermi energy level. Extra electrons occupied the *d* orbitals due to the partial phase transformation, which was confirmed by the co-occurrence of 1 T and 2H phases of MoS_2 heterojunction [307,308]. It can be concluded that the rapid electrochemical exfoliation enables synchronous exfoliation of bulk MoS_2 and incorporation of Ni species into Ni-EX-MoS_2 nanosheets. The stable 1 T/2H phase MoS_2 interface and the existence of Ni elements with tuning the electronic structure as an active center of Ni-EX-MoS_2, favored the HER with a low overpotential of 145 mV (j = 10 mA cm^{-2}) as well as a low Tafel slope of 89 mV dec^{-1} in alkaline medium. Bayat et al. demonstrated an interesting exfoliation-based methodology to vertically grow MoS_2 QDs and nanoflakes (NFs) on a transparent conducting substrate consisting of fluorine-doped-tin-oxide (FTO) [309]. It showed a small charge transport resistance of 16 Ω and a Tafel slope of 74 mV dec^{-1}. As well, Liu et al. used a lithium insertion method to exfoliate 1 T MoS_2 nanosheets from bulk MoS_2 powder and combined them with Porous graphene (P-rGO) [310]. The obtained 1 T MoS_2/P-rGO displayed an overpotential of ∼130 mV (j = 10 mA cm^{-2}) and a Tafel of ∼75 mV dec^{-1}. However, despite several advantages, the exfoliation methods could be tiresome and laborious because of lengthy procedures, complicated steps and involvement of hazardous and toxic solvents [311].

6.5. Colloidal synthesis

In the previous sections, many bottom-up and top-down approaches to synthesizing MoS_2-based electrocatalysts have been discussed along with their pros and cons which are also summarized in Table 4. In addition, colloidal synthesis is another important bottom-up technique to fabricate MoS_2 with delicate precision in morphology, ease in tuning the structure and chemistry, doping and atomic substitution, better dispersion and high purity without requiring high pressures, toxic solvents expensive equipment and special protocols [313–315]. The liquid-phase colloidal method includes several chemical reactions for which a chemical reactor is important [314]. However, the method is par-

Table 2
HER performance of the electrocatalysts fabricated via CVD.

Sr. No.	Synthesis Control	Strategy to improve HER	Overpotentials (mV) at the j = 10 mA cm^{-2}	Tafel slope (mV dec^{-1})	Electrolyte	Ref.
1	Tailoring of the CVD parameters to vertically grow MoS_2 platelets	High-porosity edge-exposed MoS_2 network	640	90	0.5 M H_2SO_4	[241]
2	Metal-organic chemical vapor deposition (MOCVD) at different temperature	Vertically standing MoS_2 nanosheets	335	94	0.5 M H_2SO_4	[242]
3	Salt-templated low-pressure CVD (LPCVD)	Growing 3D MoS_2 nanosheets salt templates	300–355	87–104	0.5 M H_2SO_4	[254]
4	Double-walled quartz tubes and a cuboid box substrate with APCVD	Large-area highly branched MoS_2 dendrites	–	76	0.5 M H_2SO_4	[255]
5	Defect engineering via post-CVD annealing in Ar	Frenkel-defected monolayer MoS_2	164	36	0.5 M H_2SO_4	[281]
6	Chemical etching in conjunction with O_2– plasma pretreatment	Morphology alteration	340 (at 0.5 mA cm^{-2})	138	0.5 M H_2SO_4	[288]
7	H_2– annealing as a defect engineering approach	Introducing vacancy defects	193	93	0.5 M H_2SO_4	[287]
8	Doping the MoS_2 monolayer with Octadecyltrichlorosilane (ODTS) and (3-aminopropyl)-triethoxysilane (APTES) to have p-doping and n-doping samples, respectively	n-doped MoS_2 monolayer	382	110	0.5 M H_2SO_4	[286]
9	Use of mixed precursors of transition metals during the intermediate-reaction-mediated CVD	the high doping concentration of V above 16%	100	36	0.5 M H_2SO_4	[151]
10	Sulfurize drop-coated $CoCl_2$/$MoCl_5$ substrates	Co-doped MoS_2 nanosheet arrays	185	65	0.5 M H_2SO_4	[268]
11	Two-step low-pressure CVD (LPCVD)	3D heterostructures of MoS_2/MoO_2 nanosheets	142	35.6	0.5 M H_2SO_4	[259]
12	CVD with a dual-temperature-zone system	MoS_2/graphene heterostructures	185	45	0.5 M H_2SO_4	[260]
13	Applying mechanically exfoliated WTe_2 monolayer was on top of the CVD-grown MoS_2 monolayer.	Heterostructures of MoS_2/WTe_2	140	40	0.5 M H_2SO_4	[261]
14	Growth in a single CVD process	Heterostructures of MoS_2 micro flowers/VS_2	199.6	95	0.5 M H_2SO_4	[262]
15	1. nickel electrodeposition on carbon cloth (CC). 2. thermal CVD growth of graphene. 3. two-zone CVD furnace for MoS_2.	Heterostructures of MoS_2/Gr/CC	91	48	0.5 M H_2SO_4	[266]
16	Synthesis in a single CVD process	Heterostructures of$MoS_{2(1x)}Se_{2x}$ ternary alloy with carbon nanofibers (CNFs)	150	144	0.5 M H_2SO_4	[267]
17	One-step CVD synthesis of NbS_2/MoS_2-CNF heterostructure	Growing nanosheets of NbS_2/MoS_2 vertically on CNFs	227 in 0.5 M $HClO_4$, 207 in 0.5 M Na_2SO_4 and 334 in 0.5 M KOH (at 50 mA cm^{-2})	29.5 in 0.5 M $HClO_4$, 28 in 0.5 M Na_2SO_4 and 33 in 0.5 M KOH	0.5 M $HClO_4$ (pH ∼ 0), 0.5 M Na_2SO_4 (pH ∼ 7) and 0.5 M KOH (pH ∼ 14)	[269]
18	Applying an external vertical magnetic field on CVD-grown MoS_2 flakes	Making imperfect structures and introducing ferromagnetic properties into 2D MoS_2	113	59	0.5 M H_2SO_4	[280]

Table 3
HER performance of the electrocatalysts produced through the exfoliation method.

Sr. No,	Synthesis control	Strategy to improve HER	Overpotentials (mV) at j = 10 mA cm^{-2}	Tafel slope (mV dec^{-1})	Electrolyte	Ref.
1	Combining ball-milling and liquid-phase exfoliation	Changing morphology to MoS_2 nanosheets	284	97	0.5 M H_2SO_4	[297]
2	Ball-milling with ultrasonic methods	Introducing defect	160	46	0.5 M H_2SO_4	[301]
3	one-step electrochemical exfoliation strategy	2D Ni-doped MoS_2 nanosheets (Ni-EX-MoS_2)	145	89	1 M KOH	[303]
4	Exfoliation and binder-free deposition on fluorine-doped tin oxide (FTO)	vertical deposition of MoS_2 QDs/NFs	250	74	0.5 M H_2SO_4	[309]
5	Applying pulsed laser irradiation in liquid to perform single-step exfoliation	Production of S vacancies and 2H-to-1 T phase transition	180	54	0.5 M H_2SO_4	[312]
6	Lithium insertion method to exfoliate 1 T MoS_2 nanosheets method	Combining 1 T MoS_2 nanosheets with porous rGO	130 mV	75	0.5 M H_2SO_4	[310]

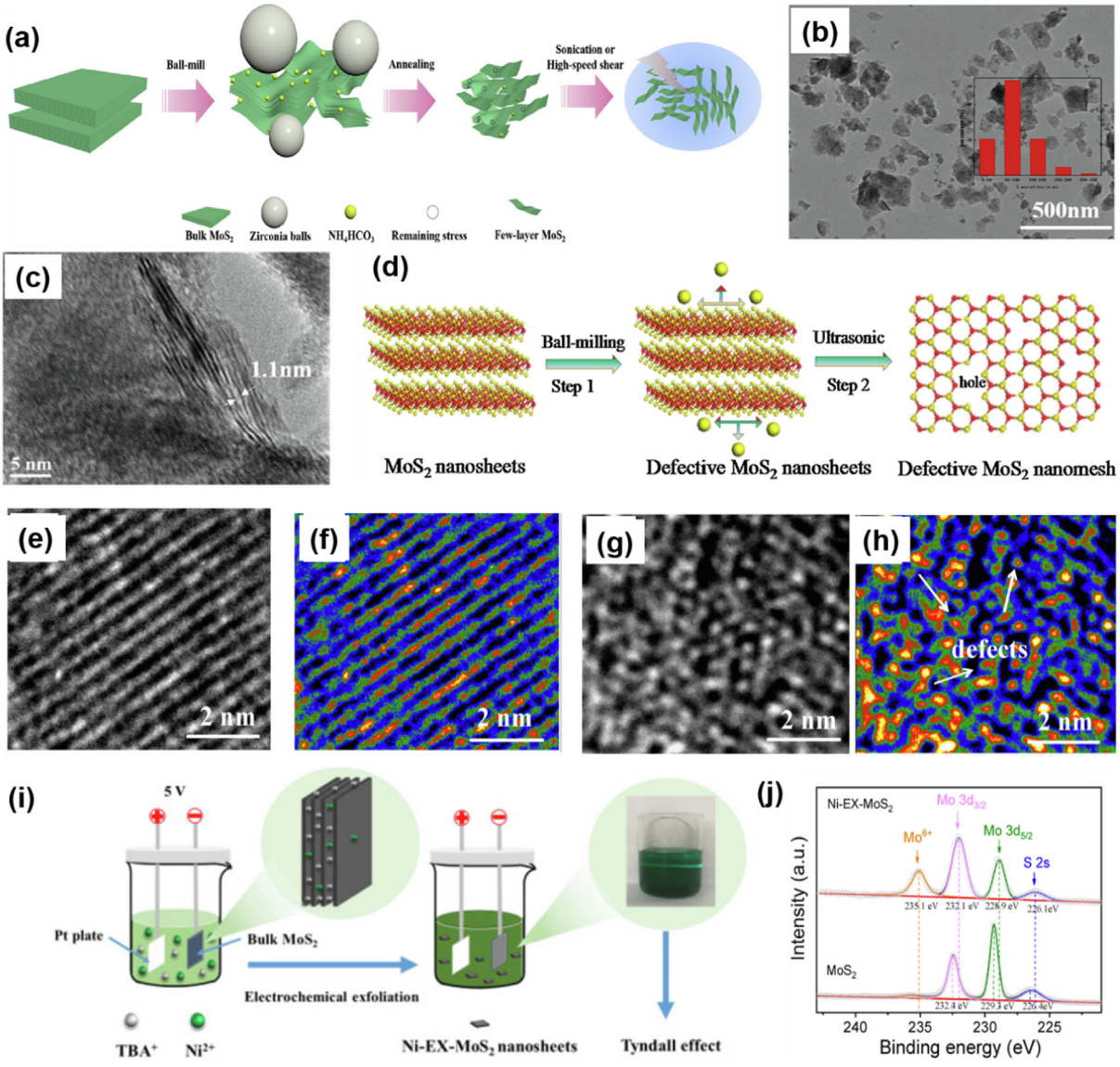

Fig. 13. Schematic diagram (a) of MoS_2 exfoliation by a combination of ball-milling and LPE. The typical TEM image (b) of H-MoS_2NS and its corresponding lateral dimension statistics histogram (inset). The typical HRTEM image (c) of H-MoS_2NS [297]. Schematic illustration of the fabrication (d) of monolayer MoS_2 nano-mesh with defective atomic-sized pores in the basal plane for amplifying HER catalysis. HRTEM images of (e) MoS_2 nanosheets and (g) MoS_2 nano-mesh. (f and h) are false–color images responding to (e and g), respectively [301]. Schematic diagram (i) of the electrochemical exfoliation and synthetic procedure and high-resolution XPS spectra (j) of Mo 3*d* for Bulk MoS_2 and Ni-EX-MoS_2 [303]. (a–c) Reproduced with permission from Ref. [297]. Copyright 2020, Elsevier Ltd. (d–h) Reproduced with permission from Ref. [301]. Copyright 2018, Elsevier Ltd. (i and j) Reproduced with permission from Ref. [303] Copyright 2023, Elsevier Ltd.

Table 4
summarizes the advantages and challenges of major fabrication techniques traditionally used for MoS_2 electrocatalysts.

Synthesis techniques	Advantages	Challenges
Hydrothermal Synthesis	Cost-effectiveness, simple experimental setups, easy to perform, provide a high quality of dispersion and reaction optimization	Inferior reproducibility, longer reaction times, lower crystallinity, and lesser uniformity
CVD	Grow atomically thin MoS_2, compatibility with industrial setups, optimum purity, better reproducibility	Requires precursor designing and substrate engineering, toxic reactive gases gas, optimization of synthesis parameters, flammable vapors
Exfoliation	Low cost, easier to break the van der Waal forces	Long procedures, difficult to control thickness, lower yield, sometimes hazardous solvents, reproducibility issue

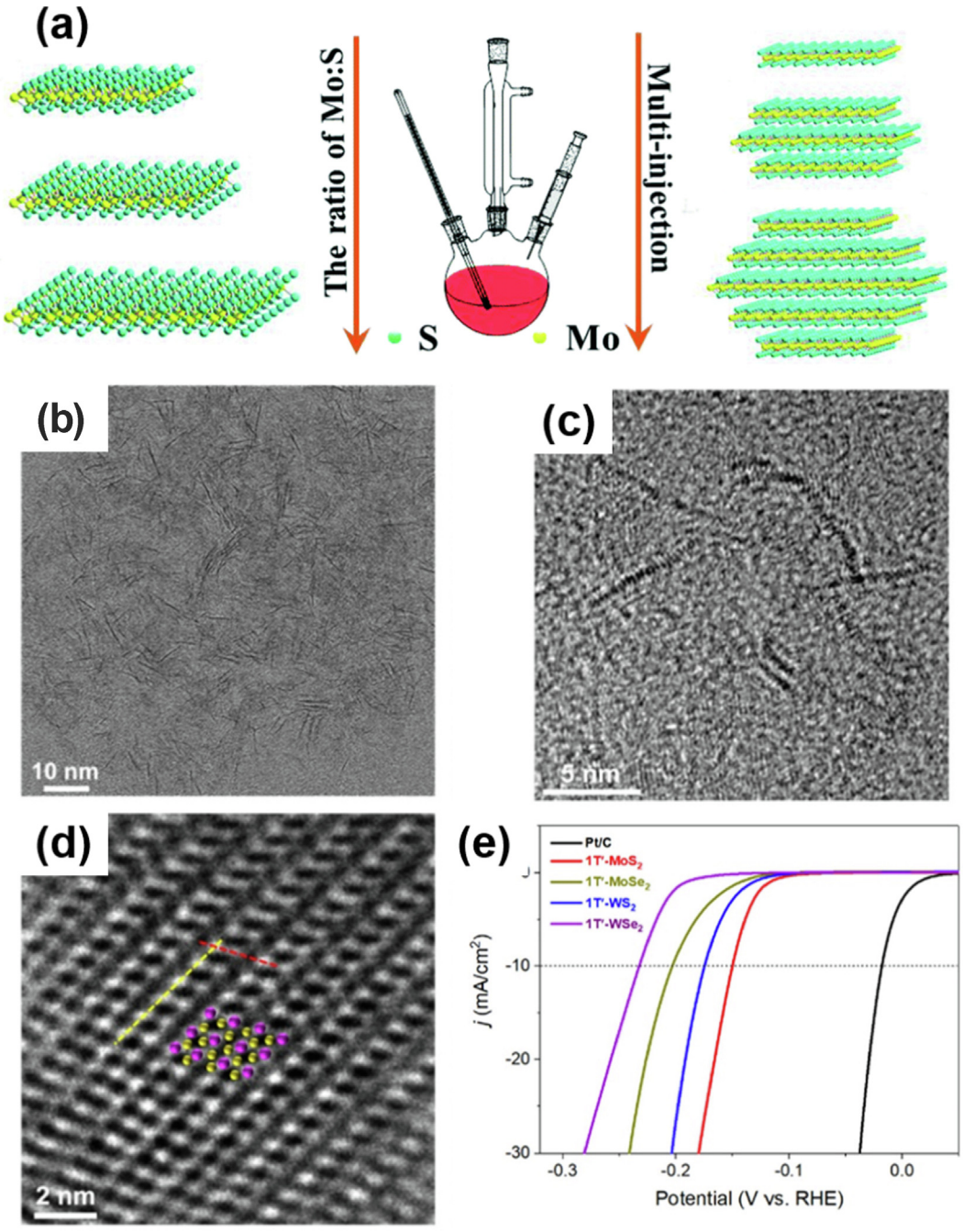

Fig. 14. Conceptual illustration of the colloidal synthesis of monolayer MoS_2 nanosheets (a) where the average lateral size is decided by the molybdenum to sulfur ratio while the number of MoS_2 layers was controlled by the multi-injection method [316]. TEM micrographs of as-developed MoS_2 taken at lower (b) and higher (c) magnifications whereas the HRTEM image (d) of monolayers of 1 T phase of MoS_2 nano-monolayer clearly shows the zigzag chains of molybdenum atoms as specified with purple balls. Polarization curves of the TMDCs synthesized via colloidal synthesis (e) indicate the best performance of MoS_2 [317]. (a) Reproduced with permission from Ref. [316]. Copyright 2016, Royal Society of Chemistry (RSC). (b–e) Reproduced with permission from Ref. [317]. Copyright 2022. American Chemical Society (ACS).

ticularly popular for the synthesis of QDs and NCs of semiconducting inorganic materials. Zhou et al. attempted to extend the spectrum of the colloidal synthesis and produced single and multilayer MoS_2 with exclusive control over their anisotropic growth [316]. The adopted colloidal synthesis with a hot-injection method is schematically illustrated in Fig. 14(a). The lateral size of the achieved monolayers of MoS_2 can be varied from 8 to 25 nm just by changing the ratio of sulfur and molybdenum precursors whereas the multi-junction method helps in controlling the number of MoS_2 layers in odd numbers as 1, 3 and 5 layers. The ultrathin and small-sized 2D MoS_2 especially in the monolayer configuration showed remarkably good HER activity and durability with a minimal overpotential of 100 mV and Tafel slope of 52 mV dec^{-1}. Recently, Liu and co-researchers applied a colloidal synthesis approach to produce monolayer and highly pure 1 T phase TMDCs, importantly MoS_2 with very good yield [317]. The TEM micrographs presented in Fig. 14(b) revealed properly defined single layers of 1 T phase of MoS_2 whereas the side wide given in Fig. 14(c) specifies the good crystallinity of obtained MoS_2 with a uniform thickness of ca. 0.65 nm; however, the average size of the formed nanosheets was nearly 7.2 nm. Moreover, the HRTEM analysis (Fig. 14d) of the monolayer evidently confirmed the single crystal growth and zigzag atomic chains of molybdenum which is a particular feature of 1 T distorted phase. Such remarkable features of the obtained MoS_2 realized the best HER performance compared to other TMDCs in 0.5 M H_2SO_4 as can be appreciated in Fig. 14(e). The overpotential at 10 mA cm^{-2} was calculated to be 149 mV with a Tafel 42 mV dec^{-1} and exhibited very good operational durability. Such an amazing HER activity was originated from the edge-rich and highly strained nano-engineered structure of 1 T MoS_2 whose basal planes were extraordinarily active. Maiti et al. synthesized $Cu_{2-x}S$–MoS_2 hybrid for HER application using a single-pot colloidal approach and the obtained material consisted of octahedral $Cu_{2-x}S$ cores embedded in the 1–2 layers cages of MoS_2 [318]. The developed $Cu_{2-x}S$–MoS_2 hybrid outperformed the MoS_2 and Cu_2S with a relatively lower overpotential of 340 mV in 0.5 M H_2SO_4. The in-depth analysis and theoretical calculation provide insights into the origin of enhanced HER activity. It was elucidated that mobile copper atoms aid the transformation to stability of 1 T phase of MoS_2 while the MoS_2 layers promote the electronic rearrangement that finally enhances the electrocatalytic activity of sulfur atoms located in the basal plane.

7. Conclusions

2D layered MoS_2 owing to its cost-effectiveness and efficient electrocatalytic activity with ΔG_{H^*} is emerging as a reliable candidate to replace expensive and scarce PGMs. In MoS_2 electrocatalytically active sites can exist along the exposed edges, grain boundaries, defects and discontinuities, heterojunctions and so on. However, in bulk form, it shows negligible activity due to low conductance and less availability of reaction sites. Moreover, the stable 2H phase is a semiconductor in nature with very high resistance for charge carrier mobility and inactive basal plan whereas the highly efficient metallic 1 T phase of MoS_2 is metastable and might undergo underside transformation over time. The major issues limiting the mass-scale deployment of MoS_2 as PGM-free electrocatalysts for HER are related to lower electronic conductivity, inactive basal plane, limited edges sites, unexposed active site structures and instability of 1 T phase. Nevertheless, such problems can be effectively dealt by modulating the electronic structure, engineering the edges, activating the basal plane, defect inducement, controlling phase transformation, heteroatomic doping, downsizing, forming heterostructures and developing nanocomposites through target-oriented fabrication strategies. In the given pursuit, major attention should be given to enhancing conductivity, arriving at near-benchmark electrocatalytic activity and operational durability. The presented review provides a thorough understanding of structural parameters, nature and engineering of the active site, stability and performance metrics for MoS_2 and primarily focuses on the fabrication techniques used so far to uplift the performance of derived electrocatalysts, i.e., hydrothermal synthesis, CVD, exfoliation, plasma treatment, colloidal synthesis etc. It is quite evident from the literature that a suitable experimental design can assure the development of definitive site structures that can directly influence performance.

Despite the highly acknowledgeable scientific endeavors invested over the last few decades to rationalize the employment of MoS_2 as a PGM-free electrocatalyst for efficient HER still, several challenges are to be addressed and therefore, the prospective developments can target the following aims: (1) no doubt CVD, hydrothermal and exfoliation-based synthesis can provide ultrathin MoS_2-based electrocatalysts the commercial-scale production of MoS_2 is still very far and therefore, the methods have to be elevated up to industrial-levels without affecting the material's quality. (2) Presently, scientific developments are more focused on improving the HER performance by engineering the structural parameters; however, fundamental knowledge about the reaction mechanism and its corresponding relationship with the structure and composition of MoS_2 active sites is still ambiguous so the in-situ analysis to figure out the role of site structures could be another important research hotspot. (3) Regarding the catalytic mechanism, the activation of the MoS_2 basal plane has been recently proposed to achieve high electrocatalytic activity, which is different from the common understanding in which the catalytic behaviors only appear at the edge of the MoS_2 therefore, in-depth investigation is required to resolve this discrepancy. (4) The activity and stability of 1 T MoS_2 over the whole pH window need to be elucidated. (5) As underlined in the stability section, Mo and MoS_2 are stable in a smaller potential window and a slow but constant dissolution can probably occur in alkaline electrolytes affecting negatively the durability required for large-scale AWEs or AEMWEs. In fact, it is not the case that when these materials are tested in alkaline electrolyte, durability tests or accelerated stress tests are missing and information on dissolution or post-mortem/end-of-life analysis are always absent.

Declaration of Competing Interest

The authors declare that they have no known competing financial interests or personal relationships that could have appeared to influence the work reported in this paper.

Acknowledgments

C.S. would like to thank the support from: 1) the Italian Ministry of University and Research (MUR) through the "Rita Levi Montalcini 2018" Fellowship (Grant number PGR18MAZLI) and 2) ENEA – UNIMIB PNRR agreement (Attività 1.1.3 del PNRR POR H_2). L.E., C. S., M.A. and M.D.A. would like to acknowledge the Ministry of Science and Technology (State of Israel) and the Ministry of Foreign Affairs and International Cooperation – Directorate General for Cultural and Economic Promotion and Innovation (Italian Republic), respectively, within the bilateral project Italy-Israel (WE-CAT). A. L. thanks the Italian ministry MUR for funding through the FISR 2019 project AMPERE (FISR2019_01294).

References

[1] R. Saidur, E.A. Abdelaziz, A. Demirbas, M.S. Hossain, S. Mekhilef, Renew. Sustain. Energy Rev. 15 (2011) 2262–2289.

[2] T. Wang, L. Xue, P. Brimblecombe, Y.F. Lam, L. Li, L. Zhang, Sci. Total Environ. 575 (2017) 1582–1596.
[3] A. Mahmoud, M. Shuhaimi, M. Abdel Samed, Energy 34 (2009) 190–195.
[4] F. Perera, Int. J. Environ. Res. Public Health 15 (2018) 16.
[5] N.S. Lewis, D.G. Nocera, Proc. Natl. Acad. Sci. 103 (2006) 15729–15735.
[6] Q. Wang, R. Guo, Z. Wang, D. Shen, R. Yu, K. Luo, C. Wu, S. Gu, Fuel 293 (2021).
[7] J.O.M. Bockris, Int. J. Hydrog. Energy 38 (2013) 2579–2588.
[8] R. Sun, X. Huang, J. Jiang, W. Xu, S. Zhou, Y. Wei, M. Li, Y. Chen, S. Han, Dalton Trans. 51 (2022) 15205–15226.
[9] Z. Abdin, A. Zafaranloo, A. Rafiee, W. Mérida, W. Lipiński, K.R. Khalilpour, Renew. Sustain. Energy Rev. 120 (2020).
[10] X. Zou, Y. Zhang, Chem. Soc. Rev. 44 (2015) 5148–5180.
[11] A.M. Elberry, J. Thakur, J. Veysey, J. Energy Storage 44 (2021).
[12] A. Evans, V. Strezov, T.J. Evans, Renew. Sustain. Energy Rev. 16 (2012) 4141–4147.
[13] M. Yekini Suberu, M. Wazir Mustafa, N. Bashir, Renew. Sustain. Energy Rev. 35 (2014) 499–514.
[14] M. Anvari, G. Lohmann, M. Wächter, P. Milan, E. Lorenz, D. Heinemann, M.R.R. Tabar, J. Peinke, New J. Phys. 18 (2016).
[15] J.A. Turner, Science 285 (1999) 687–689.
[16] C. Santoro, A. Lavacchi, P. Mustarelli, V. Di Noto, L. Elbaz, D.R. Dekel, F. Jaouen, ChemSusChem 15 (2022) e202200027.
[17] H.A. Miller, K. Bouzek, J. Hnat, S. Loos, C.I. Bernäcker, T. Weißgärber, L. Röntzsch, J. Meier-Haack, Sustain. Energy Fuels 4 (2020) 2114–2133.
[18] S. Shiva Kumar, V. Himabindu, Mater. Sci. Energy Technol. 2 (2019) 442–454.
[19] N. Du, C. Roy, R. Peach, M. Turnbull, S. Thiele, C. Bock, Chem. Rev. 122 (2022) (1895) 11830–11831.
[20] Y. Yan, P. Wang, J. Lin, J. Cao, J. Qi, J. Energy Chem. 58 (2021) 446–462.
[21] F. Zhou, Y. Zhou, G.-G. Liu, C.-T. Wang, J. Wang, Rare Met. 40 (2021) 3375–3405.
[22] S. Wang, A. Lu, C.-J. Zhong, Nano Converg. 8 (2021) 4.
[23] J. Wang, F. Xu, H. Jin, Y. Chen, Y. Wang, Adv. Mater. 29 (2017) 1605838.
[24] W. Moschkowitsch, O. Lori, L. Elbaz, ACS Catal. 12 (2022) 1082–1089.
[25] B. Owens-Baird, Y.V. Kolen'ko, K. Kovnir, Chem. – Eur. J. 24 (2018) 7298–7311.
[26] M. Muhyuddin, J. Filippi, L. Zoia, S. Bonizzoni, R. Lorenzi, E. Berretti, L. Capozzoli, M. Bellini, C. Ferrara, A. Lavacchi, C. Santoro, ChemSusChem 15 (2022) e202102351.
[27] D.V. Esposito, S.T. Hunt, Y.C. Kimmel, J.G. Chen, J. Am. Chem. Soc. 134 (2012) 3025–3033.
[28] A. Eftekhari, Int. J. Hydrog. Energy 42 (2017) 11053–11077.
[29] J. Wei, M. Zhou, A. Long, Y. Xue, H. Liao, C. Wei, Z.J. Xu, Nano-Micro Lett. 10 (2018) 75.
[30] S.A. Mirshokraee, M. Muhyuddin, R. Morina, L. Poggini, E. Berretti, M. Bellini, A. Lavacchi, C. Ferrara, C. Santoro, J. Power Sources 557 (2023).
[31] A. Chen, J. Cai, Z. Wang, Y. Han, S. Ye, J. Li, J. Energy Chem. 78 (2023) 268–276.
[32] S.A. Mirshokraee, M. Muhyuddin, J. Orsilli, E. Berretti, L. Capozzoli, A. Lavacchi, C.L. Vecchio, V. Baglio, A. Galli, A. Zaffora, F.D. Franco, M. Santamaria, L. Olivi, S. Pollastri, C. Santoro, Ind. Chem. Mater. (2023).
[33] E. Lee, B.P.T. Fokwa, Acc. Chem. Res. 55 (2022) 56–64.
[34] Y. Yao, Z. Zhang, L. Jiao, ENERGY Environ. Mater. 5 (2022) 470–485.
[35] S. Gupta, M.K. Patel, A. Miotello, N. Patel, Adv. Funct. Mater. 30 (2020) 1906481.
[36] Y. Abghoui, E. Skúlason, J. Phys. Chem. C 121 (2017) 24036–24045.
[37] L. Lin, S. Piao, Y. Choi, L. Lyu, H. Hong, D. Kim, J. Lee, W. Zhang, Y. Piao, EnergyChem 4 (2022).
[38] P. Yu, F. Wang, T.A. Shifa, X. Zhan, X. Lou, F. Xia, J. He, Nano Energy 58 (2019) 244–276.
[39] M. Zeng, Y. Li, J. Mater. Chem. A 3 (2015) 14942–14962.
[40] D. Siegmund, N. Blanc, M. Smialkowski, K. Tschulik, U.-P. Apfel, ChemElectroChem 7 (2020) 1514–1527.
[41] J.H. Nam, M.J. Jang, H.Y. Jang, W. Park, X. Wang, S.M. Choi, B. Cho, J. Energy Chem. 47 (2020) 107–111.
[42] A. Bar-Hen, S. Hettler, A. Ramasubramaniam, R. Arenal, R. Bar-Ziv, M. Bar Sadan, J. Energy Chem. 74 (2022) 481–488.
[43] T. Guo, Y. Song, Z. Sun, Y. Wu, Y. Xia, Y. Li, J. Sun, K. Jiang, S. Dou, J. Sun, J. Energy Chem. 42 (2020) 34–42.
[44] Y. Li, W. Wang, B. Huang, Z. Mao, R. Wang, B. He, Y. Gong, H. Wang, J. Energy Chem. 57 (2021) 99–108.
[45] T. Cui, J. Dong, X. Pan, T. Yu, Q. Fu, X. Bao, J. Energy Chem. 28 (2019) 123–127.
[46] D. Chen, Z. Chen, X. Zhang, Z. Lu, S. Xiao, B. Xiao, C.V. Singh, J. Energy Chem. 52 (2021) 155–162.
[47] H. Zhang, X. Yang, H. Zhang, J. Ma, Z. Huang, J. Li, Y. Wang, Chem. – Eur. J. 27 (2021) 5074–5090.
[48] H. Du, R.-M. Kong, X. Guo, F. Qu, J. Li, Nanoscale 10 (2018) 21617–21624.
[49] Y. Lin, X. Chen, Y. Tuo, Y. Pan, J. Zhang, J. Energy Chem. 70 (2022) 27–35.
[50] L.-M. Cao, J. Zhang, L.-W. Ding, Z.-Y. Du, C.-T. He, J. Energy Chem. 68 (2022) 494–520.
[51] A. Jeremiasse, J. Bergsma, M. Kleijn, M. Saakes, C. Buisman, M. Stuart, H.V.M. Hamelers, Int. J. Hydrog. Energy 36 (2011) 10482–10489.
[52] Z. Chen, X. Duan, W. Wei, S. Wang, B.-J. Ni, J. Mater. Chem. A 7 (2019) 14971–15005.
[53] Y. Zheng, Y. Jiao, Y. Zhu, L.H. Li, Y. Han, Y. Chen, A. Du, M. Jaroniec, S.Z. Qiao, Nat. Commun. 5 (2014) 3783.
[54] S.A. Mirshokraee, M. Muhyuddin, R. Lorenzi, G. Tseberlidis, C.L. Vecchio, V. Baglio, E. Berretti, A. Lavacchi, C. Santoro, SusMat 3 (2023) 248–262.
[55] Z. Chen, S. Yun, L. Wu, J. Zhang, X. Shi, W. Wei, Y. Liu, R. Zheng, N. Han, B.-J. Ni, Nano-Micro Lett. 15 (2022) 4.
[56] M. Muhyuddin, N. Zocche, R. Lorenzi, C. Ferrara, F. Poli, F. Soavi, C. Santoro, Mater. Renew. Sustain. Energy 11 (2022) 131–141.
[57] W. Zhai, Y. Ma, D. Chen, J.C. Ho, Z. Dai, Y. Qu, InfoMat 4 (2022) e12357.
[58] Y. Jiao, Y. Zheng, M. Jaroniec, S.Z. Qiao, Chem. Soc. Rev. 44 (2015) 2060–2086.
[59] V. Vij, S. Sultan, A.M. Harzandi, A. Meena, J.N. Tiwari, W.-G. Lee, T. Yoon, K.S. Kim, ACS Catal. 7 (2017) 7196–7225.
[60] Y. Cheng, J. Gong, B. Cao, X. Xu, P. Jing, S.-P. Feng, R. Cheng, B. Liu, R. Gao, J. Zhang, J. Energy Chem. 68 (2022) 646–657.
[61] Y. Zhu, Q. Lin, Y. Zhong, H.A. Tahini, Z. Shao, H. Wang, Energ. Environ. Sci. 13 (2020) 3361–3392.
[62] C. Yang, R. Zhao, H. Xiang, J. Wu, W. Zhong, W. Li, Q. Zhang, N. Yang, X. Li, Adv. Energy Mater. 10 (2020) 2002260.
[63] Q. Gao, W. Zhang, Z. Shi, L. Yang, Y. Tang, Adv. Mater. 31 (2019) 1802880.
[64] S. Mansingh, K.K. Das, K. Parida, Sustain. Energy Fuels 5 (2021) 1952–1987.
[65] J.D. Benck, T.R. Hellstern, J. Kibsgaard, P. Chakthranont, T.F. Jaramillo, ACS Catal. 4 (2014) 3957–3971.
[66] Y. Yan, B. Xia, Z. Xu, X. Wang, ACS Catal. 4 (2014) 1693–1705.
[67] H. Tributsch, J.C. Bennett, J. Electroanal. Chem. Interfacial Electrochem. 81 (1977) 97–111.
[68] B. Hinnemann, P.G. Moses, J. Bonde, K.P. Jørgensen, J.H. Nielsen, S. Horch, I. Chorkendorff, J.K. Nørskov, J. Am. Chem. Soc. 127 (2005) 5308–5309.
[69] J. Tang, J. Huang, D. Ding, S. Zhang, X. Deng, Int. J. Hydrog. Energy 47 (2022) 39771–39795.
[70] X. Zhang, S. Hua, L. Lai, Z. Wang, T. Liao, L. He, H. Tang, X. Wan, RSC Adv. 12 (2022) 17959–17983.
[71] R. Luo, W.W. Xu, Y. Zhang, Z. Wang, X. Wang, Y. Gao, P. Liu, M. Chen, Nat. Commun. 11 (2020) 1011.
[72] M. Chhowalla, Z. Liu, H. Zhang, Chem. Soc. Rev. 44 (2015) 2584–2586.
[73] M.R. Vazirisereshk, A. Martini, D.A. Strubbe, M.Z. Baykara, Lubricants 7 (2019) 57.
[74] S. Nishimura, Handbook of Heterogeneous Catalytic Hydrogenation for Organic Synthesis, 1st ed., Wiley-Interscience, New York, 2001.
[75] D. Sarkar, D. Das, S. Das, A. Kumar, S. Patil, K.K. Nanda, D.D. Sarma, A. Shukla, ACS Energy Lett. 4 (2019) 1602–1609.
[76] M. Asadi, B. Kumar, A. Behranginia, B.A. Rosen, A. Baskin, N. Repnin, D. Pisasale, P. Phillips, W. Zhu, R. Haasch, R.F. Klie, P. Král, J. Abiade, A. Salehi-Khojin, Nat. Commun. 5 (2014) 4470.
[77] A.S. Walton, J.V. Lauritsen, H. Topsøe, F. Besenbacher, J. Catal. 308 (2013) 306–318.
[78] M. Chhowalla, H.S. Shin, G. Eda, L.-J. Li, K.P. Loh, H. Zhang, Nat. Chem. 5 (2013) 263–275.
[79] G. Fiori, F. Bonaccorso, G. Iannaccone, T. Palacios, D. Neumaier, A. Seabaugh, S. K. Banerjee, L. Colombo, Nat. Nanotechnol. 9 (2014) 768–779.
[80] S. Manzeli, D. Ovchinnikov, D. Pasquier, O.V. Yazyev, A. Kis, Nat. Rev. Mater. 2 (2017) 1–15.
[81] A.C. Ferrari, F. Bonaccorso, V. Fal'ko, K.S. Novoselov, S. Roche, P. Bøggild, S. Borini, F.H.L. Koppens, V. Palermo, N. Pugno, J.A. Garrido, R. Sordan, A. Bianco, L. Ballerini, M. Prato, E. Lidorikis, J. Kivioja, C. Marinelli, T. Ryhänen, A. Morpurgo, J.N. Coleman, V. Nicolosi, L. Colombo, A. Fert, M. Garcia-Hernandez, A. Bachtold, G.F. Schneider, F. Guinea, C. Dekker, M. Barbone, Z. Sun, C. Galiotis, A.N. Grigorenko, G. Konstantatos, A. Kis, M. Katsnelson, L. Vandersypen, A. Loiseau, V. Morandi, D. Neumaier, E. Treossi, V. Pellegrini, M. Polini, A. Tredicucci, G.M. Williams, B.H. Hong, J.-H. Ahn, J.M. Kim, H. Zirath, B. J. van Wees, H. van der Zant, L. Occhipinti, A.D. Matteo, I.A. Kinloch, T. Seyller, E. Quesnel, X. Feng, K. Teo, N. Rupesinghe, P. Hakonen, S.R.T. Neil, Q. Tannock, T. Löfwander, J. Kinaret, Nanoscale 7 (2015) 4598–4810.
[82] D. Jariwala, V.K. Sangwan, L.J. Lauhon, T.J. Marks, M.C. Hersam, ACS Nano 8 (2014) 1102–1120.
[83] Y. Xu, R. Ge, J. Yang, J. Li, S. Li, Y. Li, J. Zhang, J. Feng, B. Liu, W. Li, J. Energy Chem. 74 (2022) 45–71.
[84] S. Jayabal, G. Saranya, J. Wu, Y. Liu, D. Geng, X. Meng, J. Mater. Chem. A 5 (2017) 24540–24563.
[85] X. Xu, L. Pan, Q. Han, C. Wang, P. Ding, J. Pan, J. Hu, H. Zeng, Y. Zhou, J. Catal. 374 (2019) 237–245.
[86] M. Acerce, D. Voiry, M. Chhowalla, Nat. Nanotechnol. 10 (2015) 313–318.
[87] Z. Lei, J. Zhan, L. Tang, Y. Zhang, Y. Wang, Adv. Energy Mater. 8 (2018) 1703482.
[88] X. Geng, W. Sun, W. Wu, B. Chen, A. Al-Hilo, M. Benamara, H. Zhu, F. Watanabe, J. Cui, T. Chen, Nat. Commun. 7 (2016) 10672.
[89] D. Voiry, M. Salehi, R. Silva, T. Fujita, M. Chen, T. Asefa, V.B. Shenoy, G. Eda, M. Chhowalla, Nano Lett. 13 (2013) 6222–6227.
[90] T. Zhang, T. Yang, G. Qu, S. Huang, P. Cao, W. Gao, J. Energy Chem. 68 (2022) 71–77.
[91] Y.-C. Lin, D.O. Dumcenco, Y.-S. Huang, K. Suenaga, Nat. Nanotechnol. 9 (2014) 391–396.
[92] J. Zhu, Z. Wang, H. Yu, N. Li, J. Zhang, J. Meng, M. Liao, J. Zhao, X. Lu, L. Du, R. Yang, D. Shi, Y. Jiang, G. Zhang, J. Am. Chem. Soc. 139 (2017) 10216–10219.
[93] H. He, X. Li, D. Huang, J. Luan, S. Liu, W.K. Pang, D. Sun, Y. Tang, W. Zhou, L. He, C. Zhang, H. Wang, Z. Guo, ACS Nano 15 (2021) 8896–8906.
[94] S.K. C, C. Zhang, S. Hong, R.M. Wallace, K. Cho, 2D Mater. 2 (2015) 035019.
[95] A. Splendiani, L. Sun, Y. Zhang, T. Li, J. Kim, C.-Y. Chim, G. Galli, F. Wang, Nano Lett. 10 (2010) 1271–1275.
[96] A.B. Laursen, S. Kegnæs, S. Dahl, I. Chorkendorff, Energ. Environ. Sci. 5 (2012) 5577–5591.

[97] D. Merki, X. Hu, Energ. Environ. Sci. 4 (2011) 3878–3888.
[98] H. Vrubel, D. Merki, X. Hu, Energ. Environ. Sci. 5 (2012) 6136–6144.
[99] T. Wang, L. Liu, Z. Zhu, P. Papakonstantinou, J. Hu, H. Liu, M. Li, Energ. Environ. Sci. 6 (2013) 625–633.
[100] Y. Li, H. Wang, L. Xie, Y. Liang, G. Hong, H. Dai, J. Am. Chem. Soc. 133 (2011) 7296–7299.
[101] Z. Chen, D. Cummins, B.N. Reinecke, E. Clark, M.K. Sunkara, T.F. Jaramillo, Nano Lett. 11 (2011) 4168–4175.
[102] Y. Yang, K. Zhang, H. Lin, X. Li, H.C. Chan, L. Yang, Q. Gao, ACS Catal. 7 (2017) 2357–2366.
[103] W. Jaegermann, H. Tributsch, Prog. Surf. Sci. 29 (1988) 1–167.
[104] J. Kibsgaard, Z. Chen, B.N. Reinecke, T.F. Jaramillo, Nat. Mater. 11 (2012) 963–969.
[105] D. Kong, H. Wang, J.J. Cha, M. Pasta, K.J. Koski, J. Yao, Y. Cui, Nano Lett. 13 (2013) 1341–1347.
[106] H.I. Karunadasa, E. Montalvo, Y. Sun, M. Majda, J.R. Long, C.J. Chang, Science 335 (2012) 698–702.
[107] V.W. Lau, A.F. Masters, A.M. Bond, T. Maschmeyer, Chem. – Eur. J. 18 (2012) 8230–8239.
[108] F. Bao, E. Kemppainen, I. Dorbandt, R. Bors, F. Xi, R. Schlatmann, R. van de Krol, S. Calnan, ChemElectroChem 8 (2021) 195–208.
[109] J. Zhang, T. Wang, P. Liu, S. Liu, R. Dong, X. Zhuang, M. Chen, X. Feng, Energ. Environ. Sci. 9 (2016) 2789–2793.
[110] Y. Zheng, Y. Jiao, A. Vasileff, S.-Z. Qiao, Angew. Chem. Int. Ed. 57 (2018) 7568–7579.
[111] J. Theerthagiri, S.J. Lee, A.P. Murthy, J. Madhavan, M.Y. Choi, Curr. Opin. Solid State Mater. Sci. 24 (2020).
[112] A.P. Murthy, J. Theerthagiri, J. Madhavan, K. Murugan, PCCP 19 (2017) 1988–1998.
[113] J. Hu, C. Zhang, L. Jiang, H. Lin, Y. An, D. Zhou, M.K.H. Leung, S. Yang, Joule 1 (2017) 383–393.
[114] T. An, Y. Wang, J. Tang, W. Wei, X. Cui, A.M. Alenizi, L. Zhang, G. Zheng, J. Mater. Chem. A 4 (2016) 13439–13443.
[115] B.E. Conway, B.V. Tilak, Electrochim. Acta 47 (2002) 3571–3594.
[116] D. Strmcnik, P.P. Lopes, B. Genorio, V.R. Stamenkovic, N.M. Markovic, Nano Energy 29 (2016) 29–36.
[117] J. Greeley, T.F. Jaramillo, J. Bonde, I. Chorkendorff, J.K. Nørskov, Nat. Mater. 5 (2006) 909–913.
[118] P. Sabatier, Berichte Dtsch. Chem. Ges. 44 (1911) 1984–2001.
[119] M.S. Faber, S. Jin, Energ. Environ. Sci. 7 (2014) 3519–3542.
[120] G. Rothenberg, Catalysis: Concepts and Green Applications, John Wiley & Sons, 2017.
[121] C.G. Morales-Guio, L.-A. Stern, X. Hu, Chem. Soc. Rev. 43 (2014) 6555–6569.
[122] R. Parsons, Trans. Faraday Soc. 54 (1958) 1053–1063.
[123] J. Wang, H. Zhang, X. Wang, Small Methods 1 (2017) 1700118.
[124] T. Wang, H. Xie, M. Chen, A. D'Aloia, J. Cho, G. Wu, Q. Li, Nano Energy 42 (2017) 69–89.
[125] D. Barayang Putungan, S.-H. Lin, J.-L. Kuo, PCCP 17 (2015) 21702–21708.
[126] J. Bonde, P.G. Moses, T.F. Jaramillo, J.K. Nørskov, I. Chorkendorff, Faraday Discuss. 140 (2009) 219–231.
[127] C. Tsai, K. Chan, J.K. Nørskov, F. Abild-Pedersen, Surf. Sci. 640 (2015) 133–140.
[128] T.F. Jaramillo, K.P. Jørgensen, J. Bonde, J.H. Nielsen, S. Horch, I. Chorkendorff, Science 317 (2007) 100–102.
[129] N. Ran, W. Qiu, E. Song, Y. Wang, X. Zhao, Z. Liu, J. Liu, Chem. Mater. 32 (2020) 1224–1234.
[130] M. Ďurovič, J. Hnát, K. Bouzek, J. Power Sources 493 (2021).
[131] B. Ruqia, M. Kanti Kabiraz, J. Wook Hong, S.-I. Choi, J. Energy Chem. 72 (2022) 217–240.
[132] S. Anantharaj, S.R. Ede, K. Sakthikumar, K. Karthick, S. Mishra, S. Kundu, ACS Catal. 6 (2016) 8069–8097.
[133] V. Kiran, D. Mukherjee, R.N. Jenjeti, S. Sampath, Nanoscale 6 (2014) 12856–12863.
[134] X. Ren, Q. Ma, H. Fan, L. Pang, Y. Zhang, Y. Yao, X. Ren, S. (Frank) Liu, Chem. Commun. 51 (2015) 15997–16000.
[135] Q. Hu, G. Li, Z. Han, Z. Wang, X. Huang, H. Yang, Q. Zhang, J. Liu, C. He, Chem. – Eur. J. 26 (2020) 3930–3942.
[136] Z. Li, C. Li, J. Chen, X. Xing, Y. Wang, Y. Zhang, M. Yang, G. Zhang, J. Energy Chem. 70 (2022) 18–26.
[137] C. Tsai, H. Li, S. Park, J. Park, H.S. Han, J.K. Nørskov, X. Zheng, F. Abild-Pedersen, Nat. Commun. 8 (2017) 15113.
[138] L. Li, Z. Qin, L. Ries, S. Hong, T. Michel, J. Yang, C. Salameh, M. Bechelany, P. Miele, D. Kaplan, M. Chhowalla, D. Voiry, ACS Nano 13 (2019) 6824–6834.
[139] D. Le, T.B. Rawal, T.S. Rahman, J. Phys. Chem. C 118 (2014) 5346–5351.
[140] M. Cavallini, D. Gentili, ChemPlusChem 87 (2022) e202100562.
[141] Y. Liang, Y. Li, H. Wang, H. Dai, J. Am. Chem. Soc. 135 (2013) 2013–2036.
[142] Z. Wang, H. Li, Z. Liu, Z. Shi, J. Lu, K. Suenaga, S.-K. Joung, T. Okazaki, Z. Gu, J. Zhou, Z. Gao, G. Li, S. Sanvito, E. Wang, S. Iijima, J. Am. Chem. Soc. 132 (2010) 13840–13847.
[143] K. Yan, L. Fu, H. Peng, Z. Liu, Acc. Chem. Res. 46 (2013) 2263–2274.
[144] Y. Cheng, H. Song, H. Wu, P. Zhang, Z. Tang, S. Lu, Chem. – Asian J. 15 (2020) 3123–3134.
[145] C. Xie, D. Yan, W. Chen, Y. Zou, R. Chen, S. Zang, Y. Wang, X. Yao, S. Wang, Mater. Today 31 (2019) 47–68.
[146] Z. Xiao, C. Xie, Y. Wang, R. Chen, S. Wang, J. Energy Chem. 53 (2021) 208–225.
[147] Z. Jiang, W. Zhou, C. Hu, X. Luo, W. Zeng, X. Gong, Y. Yang, T. Yu, W. Lei, C. Yuan, Adv. Mater. n/a (2023) 2300505.
[148] X. Liang, Y. Han, S. Zhu, Z. Li, S. Wu, L. Ling, Y. Liang, J. Alloy. Compd. 842 (2020).
[149] L. Lin, P. Sherrell, Y. Liu, W. Lei, S. Zhang, H. Zhang, G.G. Wallace, J. Chen, Adv. Energy Mater. 10 (2020) 1903870.
[150] H. Şar, A. Özden, İ. Demiroğlu, C. Sevik, N.K. Perkgoz, F. Ay, Phys. Status Solidi RRL – Rapid Res Lett. 13 (2019) 1800687.
[151] E. Son, S. Lee, J. Seo, U. Kim, S.H. Kim, J.M. Baik, Y.-K. Han, H. Park, ACS Nano 17 (2023) 10817–10826.
[152] S. Palencia-Ruiz, D. Uzio, C. Legens, D. Laurenti, P. Afanasiev, Appl. Catal. A 626 (2021).
[153] Q. Tang, D. Jiang, Chem. Mater. 27 (2015) 3743–3748.
[154] Y. Yin, J. Han, Y. Zhang, X. Zhang, P. Xu, Q. Yuan, L. Samad, X. Wang, Y. Wang, Z. Zhang, P. Zhang, X. Cao, B. Song, S. Jin, J. Am. Chem. Soc. 138 (2016) 7965–7972.
[155] J. Chen, F. Li, Y. Tang, Q. Tang, J. Mater. Chem. C 8 (2020) 15852–15859.
[156] Q. Liu, Q. Fang, W. Chu, Y. Wan, X. Li, W. Xu, M. Habib, S. Tao, Y. Zhou, D. Liu, T. Xiang, A. Khalil, X. Wu, M. Chhowalla, P.M. Ajayan, L. Song, Chem. Mater. 29 (2017) 4738–4744.
[157] G. Correa, P. Marocco, P. Muñoz, T. Falagüerra, D. Ferrero, M. Santarelli, Int. J. Hydrog. Energy 47 (2022) 4315–4327.
[158] Z. Wang, Y.-R. Zheng, J. Montoya, D. Hochfilzer, A. Cao, J. Kibsgaard, I. Chorkendorff, J.K. Nørskov, ACS Energy Lett. 6 (2021) 2268–2274.
[159] M. Ledendecker, J.S. Mondschein, O. Kasian, S. Geiger, D. Göhl, M. Schalenbach, A. Zeradjanin, S. Cherevko, R.E. Schaak, K. Mayrhofer, Angew. Chem. Int. Ed. 56 (2017) 9767–9771.
[160] Z. Wang, X. Guo, J. Montoya, J.K. Nørskov, npj Comput. Mater. 6 (2020) 1–7.
[161] S. Senapati, P. Maiti, in: 2D Nanoscale Heterostruct, Elsevier, Mater., 2020, pp. 243–255.
[162] Y.X. Gan, A.H. Jayatissa, Z. Yu, X. Chen, M. Li, J. Nanomater. 2020 (2020) e8917013.
[163] J. Strachan, A.F. Masters, T. Maschmeyer, J. Mater. Chem. A 9 (2021) 9451–9461.
[164] G. Solomon, R. Mazzaro, V. Morandi, I. Concina, A. Vomiero, Crystals 10 (2020) 1040.
[165] X. Zhang, G. Ma, J. Wang, Tungsten 1 (2019) 59–79.
[166] Z. Pu, Q. Liu, A.M. Asiri, Y. Luo, X. Sun, Y. He, Electrochim. Acta 168 (2015) 133–138.
[167] S.M. Senthil Kumar, K. Selvakumar, R. Thangamuthu, A. Karthigai Selvi, S. Ravichandran, G. Sozhan, K. Rajasekar, N. Navascues, S. Irusta, Int. J. Hydrog. Energy 41 (2016) 13331–13340.
[168] B. Mohanty, A. Mitra, B. Jena, B.K. Jena, Energy Fuels 34 (2020) 10268–10275.
[169] P. Liu, Y. Zhao, R. Qin, S. Mo, G. Chen, L. Gu, D.M. Chevrier, P. Zhang, Q. Guo, D. Zang, B. Wu, G. Fu, N. Zheng, Science 352 (2016) 797–800.
[170] M.S. Chen, D.W. Goodman, Science 306 (2004) 252–255.
[171] H. Yan, Y. Jiao, A. Wu, C. Tian, X. Zhang, L. Wang, Z. Ren, H. Fu, Chem. Commun. 52 (2016) 9530–9533.
[172] U. Kayal, B. Mohanty, P. Bhanja, S. Chatterjee, D. Chandra, M. Hara, B.K. Jena, A. Bhaumik, Dalton Trans. 48 (2019) 2220–2227.
[173] Y. Lei, F. Mehmood, S. Lee, J. Greeley, B. Lee, S. Seifert, R.E. Winans, J.W. Elam, R.J. Meyer, P.C. Redfern, D. Teschner, R. Schlögl, M.J. Pellin, L.A. Curtiss, S. Vajda, Science 328 (2010) 224–228.
[174] Y. Jiao, A.M. Hafez, D. Cao, A. Mukhopadhyay, Y. Ma, H. Zhu, Small 14 (2018).
[175] Y. Zhang, Y. Kuwahara, K. Mori, C. Louis, H. Yamashita, Nanoscale 12 (2020) (1915) 11908–111901.
[176] X. Zang, Y. Qin, T. Wang, F. Li, Q. Shao, N. Cao, ACS Appl. Mater. Interfaces 12 (2020) 55884–55893.
[177] S. Jiménez Sandoval, D. Yang, R.F. Frindt, J.C. Irwin, Phys. Rev. B 44 (1991) 3955–3962.
[178] F. Güller, A.M. Llois, J. Goniakowski, C. Noguera, Phys. Rev. B 91 (2015).
[179] Y. Lv, H. Pan, J. Lin, Z. Chen, Y. Li, H. Li, M. Shi, R. Yin, S. Zhu, Chem. Eng. J. 428 (2022).
[180] L. Yang, A. Mukhopadhyay, Y. Jiao, J. Hamel, M. Benamara, Y. Xing, H. Zhu, J. Mater. Chem. A 5 (2017) 25359–25367.
[181] M.A.R. Anjum, H.Y. Jeong, M.H. Lee, H.S. Shin, J.S. Lee, Adv. Mater. 30 (2018) 1707105.
[182] J. Xie, H. Zhang, S. Li, R. Wang, X. Sun, M. Zhou, J. Zhou, X.W. (David) Lou, Y. Xie, Adv. Mater. 25 (2013) 5807–5813.
[183] W. Chen, X. Zhu, R. Wang, W. Wei, M. Liu, S. Dong, K.K. Ostrikov, S.-Q. Zang, J. Energy Chem. 75 (2022) 16–25.
[184] S. Liu, B. Li, S.V. Mohite, P. Devaraji, L. Mao, R. Xing, Int. J. Hydrog. Energy 45 (2020) 29929–29937.
[185] X. Zou, A. Goswami, T. Asefa, J. Am. Chem. Soc. 135 (2013) 17242–17245.
[186] M. Gong, Y. Li, H. Wang, Y. Liang, J.Z. Wu, J. Zhou, J. Wang, T. Regier, F. Wei, H. Dai, J. Am. Chem. Soc. 135 (2013) 8452–8455.
[187] H. Liang, F. Meng, M. Cabán-Acevedo, L. Li, A. Forticaux, L. Xiu, Z. Wang, S. Jin, Nano Lett. 15 (2015) 1421–1427.
[188] Z. Xing, X. Yang, A.M. Asiri, X. Sun, ACS Appl. Mater. Interfaces 8 (2016) 14521–14526.
[189] G. Zhang, Y.-S. Feng, W.-T. Lu, D. He, C.-Y. Wang, Y.-K. Li, X.-Y. Wang, F.-F. Cao, ACS Catal. 8 (2018) 5431–5441.
[190] P. Kuang, M. He, H. Zou, J. Yu, K. Fan, Appl. Catal. B Environ. 254 (2019) 15–25.
[191] T. Liu, X. Sun, A.M. Asiri, Y. He, Int. J. Hydrog. Energy 41 (2016) 7264–7269.
[192] G. Zhou, Y. Chen, H. Dong, L. Xu, X. Liu, C. Ge, D. Sun, Y. Tang, Int. J. Hydrog. Energy 44 (2019) 26338–26346.
[193] G.M. Bremmer, L. van Haandel, E.J.M. Hensen, J.W.M. Frenken, P.J. Kooyman, Appl. Catal. B Environ. 243 (2019) 145–150.

[194] N. Liu, Y. Guo, X. Yang, H. Lin, L. Yang, Z. Shi, Z. Zhong, S. Wang, Y. Tang, Q. Gao, ACS Appl. Mater. Interfaces 7 (2015) 23741–23749.
[195] X. Shi, X. Ling, L. Li, C. Zhong, Y. Deng, X. Han, W. Hu, J. Mater. Chem. A 7 (2019) 23787–23793.
[196] C.-B. Ma, X. Qi, B. Chen, S. Bao, Z. Yin, X.-J. Wu, Z. Luo, J. Wei, H.-L. Zhang, H. Zhang, Nanoscale 6 (2014) 5624–5629.
[197] L. Hongtao, X. Zichen, Z. Lina, Z. Zhiqiang, X. Li, Chem. Phys. Lett. 716 (2019) 6–10.
[198] J. Deng, H. Li, S. Wang, D. Ding, M. Chen, C. Liu, Z. Tian, K.S. Novoselov, C. Ma, D. Deng, X. Bao, Nat. Commun. 8 (2017) 14430.
[199] M.B. Askari, A. Beheshti-Marnani, M. Seifi, S.M. Rozati, P. Salarizadeh, J. Colloid Interface Sci. 537 (2019) 186–196.
[200] Y. Zhang, J. Du, Z. Wang, M. Luo, Y. Tian, T. Fujita, Q. Xue, M. Chen, ACS Appl. Energy Mater. 1 (2018) 2183–2191.
[201] B. Guo, K. Yu, H. Li, H. Song, Y. Zhang, X. Lei, H. Fu, Y. Tan, Z. Zhu, ACS Appl. Mater. Interfaces 8 (2016) 5517–5525.
[202] A. Gigot, M. Fontana, M. Serrapede, M. Castellino, S. Bianco, M. Armandi, B. Bonelli, C.F. Pirri, E. Tresso, P. Rivolo, ACS Appl. Mater. Interfaces 8 (2016) 32842–32852.
[203] K. Peng, L. Fu, J. Ouyang, H. Yang, Adv. Funct. Mater. 26 (2016) 2666–2675.
[204] Y.-H. Chang, C.-T. Lin, T.-Y. Chen, C.-L. Hsu, Y.-H. Lee, W. Zhang, K.-H. Wei, L.-J. Li, Adv. Mater. 25 (2013) 756–760.
[205] M.A. Lukowski, A.S. Daniel, F. Meng, A. Forticaux, L. Li, S. Jin, J. Am. Chem. Soc. 135 (2013) 10274–10277.
[206] F. Meng, J. Li, S.K. Cushing, M. Zhi, N. Wu, J. Am. Chem. Soc. 135 (2013) 10286–10289.
[207] A.B. Laursen, P.C.K. Vesborg, I. Chorkendorff, Chem. Commun. 49 (2013) 4965–4967.
[208] T. Aditya, A.K. Nayak, D. Pradhan, A. Pal, T. Pal, Electrochim. Acta 313 (2019) 341–351.
[209] W.S.H. Jr, R.E. Offeman, J. Am. Chem. Soc. 80 (1958) 1339.
[210] Y. Xu, R. Wang, J. Wang, J. Li, T. Jiao, Z. Liu, Chem. Eng. J. 417 (2021).
[211] X. Wu, S. Li, B. Wang, J. Liu, M. Yu, PCCP 19 (2017) 11554–11562.
[212] Y. Chen, J. Wang, J. Jiang, M. Zhou, J. Zhu, S. Han, RSC Adv. 5 (2015) 21740–21744.
[213] K.-X. Wang, X.-H. Li, J.-S. Chen, Adv. Mater. 27 (2015) 527–545.
[214] C. Yuan, H.B. Wu, Y. Xie, X.W. (David) Lou, Angew. Chem. Int. Ed. 53 (2014) 1488–1504.
[215] R. Ge, W. Li, J. Huo, T. Liao, N. Cheng, Y. Du, M. Zhu, Y. Li, J. Zhang, Appl. Catal. B Environ. 246 (2019) 129–139.
[216] S. Liu, S. Li, K. Sekar, R. Li, Y. Zhu, R. Xing, K. Nakata, A. Fujishima, Int. J. Hydrog. Energy 44 (2019) 25310–25318.
[217] J. Ye, Z. Yu, W. Chen, Q. Chen, L. Ma, Int. J. Hydrog. Energy 41 (2016) 12049–12061.
[218] H. Huang, W. Huang, Z. Yang, J. Huang, J. Lin, W. Liu, Y. Liu, J. Mater. Chem. A 5 (2017) 1558–1566.
[219] Y. Guo, L. Gan, C. Shang, E. Wang, J. Wang, Adv. Funct. Mater. 27 (2017).
[220] D.H. Youn, S. Han, J.Y. Kim, J.Y. Kim, H. Park, S.H. Choi, J.S. Lee, ACS Nano 8 (2014) 5164–5173.
[221] Y. Li, S. Zhu, Y. Xu, R. Ge, J. Qu, M. Zhu, Y. Liu, J.M. Cairney, R. Zheng, S. Li, J. Zhang, W. Li, Chem. Eng. J. 421 (2021).
[222] D. Kang, Q. Liu, J. Gu, Y. Su, W. Zhang, D. Zhang, ACS Nano 9 (2015) 11225–11233.
[223] B. Hu, K. Wang, L. Wu, S.-H. Yu, M. Antonietti, M.-M. Titirici, Adv. Mater. 22 (2010) 813–828.
[224] S. Tong, S. Ma, Y. Su, Q. Li, X. Wang, X. Han, ACS Sustain. Chem. Eng. 6 (2018) 11255–11264.
[225] Y. Zhao, J. Zhao, Q. Li, C. Gu, B. Zhang, C. Liu, Z. Li, S. Hu, S. Qiao, Electrochim. Acta 331 (2020).
[226] J. Li, P.K. Shen, Z. Tian, Int. J. Hydrog. Energy 42 (2017) 7136–7142.
[227] H. Zhang, Q. Ding, D. He, H. Liu, W. Liu, Z. Li, B. Yang, X. Zhang, L. Lei, S. Jin, Energ. Environ. Sci. 9 (2016) 3113–3119.
[228] P. Xiao, M. Alam Sk, L. Thia, X. Ge, R. Jern Lim, J.-Y. Wang, K. Hwa Lim, X. Wang, Energ. Environ. Sci. 7 (2014) 2624–2629.
[229] Y. Zhang, J. Yan, X. Ren, L. Pang, H. Chen, S. (Frank) Liu, Int. J. Hydrog Energy 42 (2017) 5472–5477.
[230] Q. Xiong, X. Zhang, H. Wang, G. Liu, G. Wang, H. Zhang, H. Zhao, Chem. Commun. 54 (2018) 3859–3862.
[231] Y. Guo, J. Tang, J. Henzie, B. Jiang, H. Qian, Z. Wang, H. Tan, Y. Bando, Y. Yamauchi, Mater. Horiz. 4 (2017) 1171–1177.
[232] H. Tan, J. Tang, J. Henzie, Y. Li, X. Xu, T. Chen, Z. Wang, J. Wang, Y. Ide, Y. Bando, Y. Yamauchi, ACS Nano 12 (2018) 5674–5683.
[233] T. Niyitanga, H.K. Jeong, J. Electroanal. Chem. 849 (2019).
[234] L. Tao, X. Duan, C. Wang, X. Duan, S. Wang, Chem. Commun. 51 (2015) 7470–7473.
[235] R. Bose, S.K. Balasingam, S. Shin, Z. Jin, D.H. Kwon, Y. Jun, Y.-S. Min, Langmuir 31 (2015) 5220–5227.
[236] G.R. Bhimanapati, T. Hankins, Y. Lei, R.A. Vilá, I. Fuller, M. Terrones, J.A. Robinson, ACS Appl. Mater. Interfaces 8 (2016) 22190–22195.
[237] L. Li, R. Long, O.V. Prezhdo, Nano Lett. 18 (2018) 4008–4014.
[238] A.M. van der Zande, P.Y. Huang, D.A. Chenet, T.C. Berkelbach, Y. You, G.-H. Lee, T.F. Heinz, D.R. Reichman, D.A. Muller, J.C. Hone, Nat. Mater. 12 (2013) 554–561.
[239] Y. Zhang, Y. Yao, M.G. Sendeku, L. Yin, X. Zhan, F. Wang, Z. Wang, J. He, Adv. Mater. 31 (2019) 1901694.
[240] X. Jiang, F. Chen, S. Zhao, W. Su, CrstEngComm 23 (2021) 8239–8254.
[241] S. Li, S. Wang, M.M. Salamone, A.W. Robertson, S. Nayak, H. Kim, S.C.E. Tsang, M. Pasta, J.H. Warner, ACS Catal. 7 (2017) 877–886.
[242] K. Hernandez Ruiz, J. Liu, R. Tu, M. Li, S. Zhang, J.R. Vargas Garcia, S. Mu, H. Li, T. Goto, L. Zhang, J. Alloy. Compd. 747 (2018) 100–108.
[243] J. Zhou, H. Xiao, B. Zhou, F. Huang, S. Zhou, W. Xiao, D. Wang, Appl. Surf. Sci. 358 (2015) 152–158.
[244] S. Xiaodai Lim, K. Whye Woo, J. Ng, J. Lu, S. Yi Kwang, Z. Zhang, E. Soon Tok, C.-H. Sow, Nanoscale 7 (2015) 17538–17546.
[245] J. Eun Lee, J. Jung, T. Yeoung Ko, S. Kim, S.-I. Kim, J. Nah, S. Ryu, K. Tae Nam, M. Hyung Lee, RSC Adv. 7 (2017) 5480–5487.
[246] B.M. Vogelaar, P. Steiner, A. Dick van Langeveld, S. Eijsbouts, J.A. Moulijn, Appl. Catal. A 251 (2003) 85–92.
[247] H.F. Liu, S.L. Wong, D.Z. Chi, Chem. Vap. Depos. 21 (2015) 241–259.
[248] Y.-H. Lee, X.-Q. Zhang, W. Zhang, M.-T. Chang, C.-T. Lin, K.-D. Chang, Y.-C. Yu, J.-T.-W. Wang, C.-S. Chang, L.-J. Li, T.-W. Lin, Adv. Mater. 24 (2012) 2320–2325.
[249] X. Ling, Y.-H. Lee, Y. Lin, W. Fang, L. Yu, M.S. Dresselhaus, J. Kong, Nano Lett. 14 (2014) 464–472.
[250] C. Martella, E. Kozma, P.P. Tummala, S. Ricci, K.A. Patel, A. Andicsovà-Eckstein, F. Bertini, G. Scavia, R. Sordan, L.G. Nobili, M. Bollani, U. Giovanella, A. Lamperti, A. Molle, Adv. Mater. Interfaces 7 (2020) 2000791.
[251] A. Singh, M. Moun, M. Sharma, A. Barman, A. Kumar Kapoor, R. Singh, Appl. Surf. Sci. 538 (2021).
[252] L. Seravalli, M. Bosi, Materials 14 (2021) 7590.
[253] V.M.A. Arreola, M.F. Salazar, T. Zhang, K. Wang, A.H.B. Aguilar, K.C.S. Reddy, E. Strupiechonski, M. Terrones, A.D.L. Bugallo, 2D Mater. 8 (2021).
[254] L. Zhu, P. Yang, Y. Huan, S. Pan, Z. Zhang, F. Cui, Y. Shi, S. Jiang, C. Xie, M. Hong, J. Fu, J. Hu, Y. Zhang, Nano Res. 13 (2020) 3098–3104.
[255] W. Xu, S. Li, S. Zhou, J.K. Lee, S. Wang, S.G. Sarwat, X. Wang, H. Bhaskaran, M. Pasta, J.H. Warner, ACS Appl. Mater. Interfaces 10 (2018) 4630–4639.
[256] E.W.I. Elliott, R.D. Glover, J.E. Hutchison, ACS Nano 9 (2015) 3050–3059.
[257] M. Cargnello, C. Chen, B.T. Diroll, V.V.T. Doan-Nguyen, R.J. Gorte, C.B. Murray, J. Am. Chem. Soc. 137 (2015) 6906–6911.
[258] S. Wang, J.-K. Huang, M. Li, A. Azam, X. Zu, L. Qiao, J. Yang, S. Li, ACS Appl. Mater. Interfaces 13 (2021) 47962–47971.
[259] R.D. Nikam, A.-Y. Lu, P.A. Sonawane, U.R. Kumar, K. Yadav, L.-J. Li, Y.-T. Chen, ACS Appl. Mater. Interfaces 7 (2015) 23328–23335.
[260] Y. Wan, Z. Zhang, X. Xu, Z. Zhang, P. Li, X. Fang, K. Zhang, K. Yuan, K. Liu, G. Ran, Y. Li, Y. Ye, L. Dai, Nano Energy 51 (2018) 786–792.
[261] Y. Zhou, J.V. Pondick, J.L. Silva, J.M. Woods, D.J. Hynek, G. Matthews, X. Shen, Q. Feng, W. Liu, Z. Lu, Z. Liang, B. Brena, Z. Cai, M. Wu, L. Jiao, S. Hu, H. Wang, C.M. Araujo, J.J. Cha, Small 15 (2019) 1900078.
[262] S.H. Yu, Z. Tang, Y. Shao, H. Dai, H.Y. Wang, J. Yan, H. Pan, D.H.C. Chua, ACS Appl. Energy Mater. 2 (2019) 5799–5808.
[263] S. Ahmed, X. Ding, N. Bao, P. Bian, R. Zheng, Y. Wang, P.P. Murmu, J.V. Kennedy, R. Liu, H. Fan, K. Suzuki, J. Ding, J. Yi, Chem. Mater. 29 (2017) 9066–9074.
[264] X. Sun, J. Dai, Y. Guo, C. Wu, F. Hu, J. Zhao, X. Zeng, Y. Xie, Nanoscale 6 (2014) 8359–8367.
[265] H. Li, Q. Zhang, C.C.R. Yap, B.K. Tay, T.H.T. Edwin, A. Olivier, D. Baillargeat, Adv. Funct. Mater. 22 (2012) 1385–1390.
[266] I. Oh, J.-S. Youn, Y.-K. Park, K.-J. Jeon, Appl. Surf. Sci. 529 (2020).
[267] H. Yang, T. Zhang, H. Zhu, M. Zhang, W. Wu, M. Du, Int. J. Hydrog. Energy 42 (2017) 1912–1918.
[268] N. Huang, R. Peng, Y. Ding, S. Yan, G. Li, P. Sun, X. Sun, X. Liu, H. Yu, J. Catal. 373 (2019) 250–259.
[269] P. Gnanasekar, K.S. Ranjith, P. Manivel, Y.-K. Han, J. Kulandaivel, ACS Appl. Energy Mater. 3 (2020) 6717–6725.
[270] G. Li, Z. Chen, Y. Li, D. Zhang, W. Yang, Y. Liu, L. Cao, ACS Nano 14 (2020) 1707–1714.
[271] G. Li, D. Zhang, Q. Qiao, Y. Yu, D. Peterson, A. Zafar, R. Kumar, S. Curtarolo, F. Hunte, S. Shannon, Y. Zhu, W. Yang, L. Cao, J. Am. Chem. Soc. 138 (2016) 16632–16638.
[272] Y. Yu, C. Li, Y. Liu, L. Su, Y. Zhang, L. Cao, Sci. Rep. 3 (2013).
[273] A. Gurarslan, Y. Yu, L. Su, Y. Yu, F. Suarez, S. Yao, Y. Zhu, M. Ozturk, Y. Zhang, L. Cao, ACS Nano 8 (2014) 11522–11528.
[274] P. Yasaei, C.J. Foss, K. Karis, A. Behranginia, A.I. El-Ghandour, A. Fathizadeh, J. Olivares, A.K. Majee, C.D. Foster, F. Khalili-Araghi, Z. Aksamija, A. Salehi-Khojin, Adv. Mater. Interfaces 4 (2017) 1700334.
[275] G. Li, D. Zhang, Y. Yu, S. Huang, W. Yang, L. Cao, J. Am. Chem. Soc. 139 (2017) 16194–16200.
[276] Z. Zhang, X. Zou, V.H. Crespi, B.I. Yakobson, ACS Nano 7 (2013) 10475–10481.
[277] L. Cai, J. He, Q. Liu, T. Yao, L. Chen, W. Yan, F. Hu, Y. Jiang, Y. Zhao, T. Hu, Z. Sun, S. Wei, J. Am. Chem. Soc. 137 (2015) 2622–2627.
[278] J. Hong, C. Jin, J. Yuan, Z. Zhang, Adv. Mater. 29 (2017) 1606434.
[279] Q. Zhang, Z. Ren, N. Wu, W. Wang, Y. Gao, Q. Zhang, J. Shi, L. Zhuang, X. Sun, L. Fu, Npj 2D Mater. Appl. 2 (2018) 1–8.
[280] W. Zhou, M. Chen, M. Guo, A. Hong, T. Yu, X. Luo, C. Yuan, W. Lei, S. Wang, Nano Lett. 20 (2020) 2923–2930.
[281] J. Xu, G. Shao, X. Tang, F. Lv, H. Xiang, C. Jing, S. Liu, S. Dai, Y. Li, J. Luo, Z. Zhou, Nat. Commun. 13 (2022) 2193.
[282] S. Wang, G. Deng, J. Gu, W. Hua, X. Jia, K. Xi, Appl. Catal. A 508 (2015) 80–85.
[283] A. Parija, W. Zaheer, J. Cho, T.E.G. Alivio, S.C. Fakra, M. Al-Hashimi, D. Prendergast, S. Banerjee, Chem. Phys. Rev. 2 (2021).
[284] S.M. Gali, A. Pershin, A. Lherbier, J.-C. Charlier, D. Beljonne, J. Phys. Chem. C 124 (2020) 15076–15084.

[285] J. Yang, F. Bussolotti, H. Kawai, K.E.J. Goh, Phys. Status Solidi RRL – Rapid Res Lett. 14 (2020) 2000248.
[286] S. Pak, J. Lim, J. Hong, S. Cha, Catalysts 11 (2021) 70.
[287] S. Li, S. Zhou, X. Wang, P. Tang, M. Pasta, J.H. Warner, Mater. Today, Energy 13 (2019) 134–144.
[288] P. Zhang, H. Xiang, L. Tao, H. Dong, Y. Zhou, T.S. Hu, X. Chen, S. Liu, S. Wang, S. Garaj, Nano Energy 57 (2019) 535–541.
[289] F.C. Simeone, C. Albonetti, M. Cavallini, J. Phys. Chem. C 113 (2009) 18987–18994.
[290] M. Cavallini, P. Mei, F. Biscarini, R. García, Appl. Phys. Lett. 83 (2003) 5286–5288.
[291] H. Li, J. Wu, Z. Yin, H. Zhang, Acc. Chem. Res. 47 (2014) 1067–1075.
[292] Z. Lin, A. McCreary, N. Briggs, S. Subramanian, K. Zhang, Y. Sun, X. Li, N.J. Borys, H. Yuan, S.K. Fullerton-Shirey, A. Chernikov, H. Zhao, S. McDonnell, A. M. Lindenberg, K. Xiao, B.J. LeRoy, M. Drndić, J.C.M. Hwang, J. Park, M. Chhowalla, R.E. Schaak, A. Javey, M.C. Hersam, J. Robinson, M. Terrones, 2D Mater. 3 (2016).
[293] A.K. Geim, P. Kim, Sci. Am. 298 (2008) 90–97.
[294] L. Wu, N.Y. Dzade, M. Yu, B. Mezari, A.J.F. van Hoof, H. Friedrich, N.H. de Leeuw, E.J.M. Hensen, J.P. Hofmann, ACS Energy Lett. 4 (2019) 1733–1740.
[295] D. Zhao, S. Xu, H. Wang, Y. Shen, Q. Xu, Chem. Commun. 59 (2023) 8135–8138.
[296] X. Zhu, Z. Su, C. Wu, H. Cong, X. Ai, H. Yang, J. Qian, Nano Lett. 22 (2022) 2956–2963.
[297] Y. Li, X. Yin, X. Huang, X. Liu, W. Wu, Int. J. Hydrog. Energy 45 (2020) 16489–16499.
[298] E. Varrla, C. Backes, K.R. Paton, A. Harvey, Z. Gholamvand, J. McCauley, J.N. Coleman, Chem. Mater. 27 (2015) 1129–1139.
[299] Y. Liu, Z. Tai, J. Zhang, W.K. Pang, Q. Zhang, H. Feng, K. Konstantinov, Z. Guo, H. K. Liu, Nat. Commun. 9 (2018) 3645.
[300] S. Zhang, X. Yu, H. Yu, Y. Chen, P. Gao, C. Li, C. Zhu, ACS Appl. Mater. Interfaces 6 (2014) (1885) 21880–21882.
[301] Y. Li, K. Yin, L. Wang, X. Lu, Y. Zhang, Y. Liu, D. Yan, Y. Song, S. Luo, Appl. Catal. B Environ. 239 (2018) 537–544.
[302] Y. Li, J. Feng, H. Li, X. Wei, R. Wang, A. Zhou, Int. J. Hydrog. Energy 41 (2016) 4096–4105.
[303] H. Wei, J. Si, L. Zeng, S. Lyu, Z. Zhang, Y. Suo, Y. Hou, Chin. Chem. Lett. 34 (2023).
[304] X. Wang, Y. Zhang, H. Si, Q. Zhang, J. Wu, L. Gao, X. Wei, Y. Sun, Q. Liao, Z. Zhang, K. Ammarah, L. Gu, Z. Kang, Y. Zhang, J. Am. Chem. Soc. 142 (2020) 4298–4308.
[305] S. Ali Shah, L. Xu, R. Sayyar, T. Bian, Z. Liu, A. Yuan, X. Shen, I. Khan, A. Ali Tahir, H. Ullah, Chem. Eng. J. 428 (2022).
[306] X. Meng, C. Ma, L. Jiang, R. Si, X. Meng, Y. Tu, L. Yu, X. Bao, D. Deng, Angew. Chem. 132 (2020) 10588–10593.
[307] W. Yang, S. Zhang, Q. Chen, C. Zhang, Y. Wei, H. Jiang, Y. Lin, M. Zhao, Q. He, X. Wang, Y. Du, L. Song, S. Yang, A. Nie, X. Zou, Y. Gong, Adv. Mater. 32 (2020) 2001167.
[308] H. Jin, Y. Yu, Q. Shen, P. Li, J. Yu, W. Chen, X. Wang, Z. Kang, L. Zhu, R. Zhao, L. Zheng, W. Song, C. Cao, J. Mater. Chem. A 9 (2021) 13996–14003.
[309] A. Bayat, M. Zirak, E. Saievar-Iranizad, ACS Sustain. Chem. Eng. 6 (2018) 8374–8382.
[310] Y. Liu, J. Liu, Z. Li, X. Fan, Y. Li, F. Zhang, G. Zhang, W. Peng, S. Wang, Int. J. Hydrog. Energy 43 (2018) 13946–13952.
[311] L. Ali, F. Subhan, M. Ayaz, S.S. ul Hassan, C.C. Byeon, J.S. Kim, S. Bungau, Nanomaterials 12 (2022) 3465.
[312] Z.-W. Gao, M. Liu, W. Zheng, X. Zhang, L.Y.S. Lee, Small 15 (2019) 1903791.
[313] O.E. Meiron, L. Houben, M. Bar-Sadan, RSC Adv. 5 (2015) 88108–88114.
[314] H. Lin, C. Wang, J. Wu, Z. Xu, Y. Huang, C. Zhang, New J. Chem. 39 (2015) 8492–8497.
[315] K. Vasu, O.E. Meiron, A.N. Enyashin, R. Bar-Ziv, M. Bar-Sadan, J. Phys. Chem. C 123 (2019) 1987–1994.
[316] M. Zhou, Z. Zhang, K. Huang, Z. Shi, R. Xie, W. Yang, Nanoscale 8 (2016) 15262–15272.
[317] Z. Liu, K. Nie, X. Qu, X. Li, B. Li, Y. Yuan, S. Chong, P. Liu, Y. Li, Z. Yin, W. Huang, J. Am. Chem. Soc. 144 (2022) 4863–4873.
[318] P.S. Maiti, K. Anal, R. Ganai, A.N. Bar-Ziv, L. Enyashin, M.B. Houben, Sadan, Chem. Mater. 30 (2018) 4489–4492.